universität wien

DISSERTATION / DOCTORAL THESIS

Titel der Dissertation /Title of the Doctoral Thesis

„Magnetic structure design and source reconstruction by solving the inverse magnetostatic problem“

verfasst von / submitted by

Dipl.-Ing. Gregor Wautischer, BSc.

angestrebter akademischer Grad / in partial fulfilment of the requirements for the degree of

Doktor der Naturwissenschaften (Dr.rer.nat)

Wien, 2023 / Vienna 2023

Studienkennzahl lt. Studienblatt / degree programme code as it appears on the student record sheet:	UA 796 605 411
Dissertationsgebiet lt. Studienblatt / field of study as it appears on the student record sheet:	Physik
Betreut von / Supervisor:	Univ.-Prof. Dipl.-Ing. Dr.techn. Dieter Süss, Privatdoz.

Abstract

Magnetic structures play a key part in a multitude of applications. In order to fulfill their specified function, the involved hard or soft magnetic materials have to be designed. The design process can include the design of the external properties of the structures, i.e. their shape, or the design of their internal properties, i.e. their magnetization state. Most commonly, the design goal concerns their magnetic stray field, the magnetic field that is generated by the magnetic structure.

Another important aspect concerns the investigation of magnetic structures. During quality control, obtaining information about the magnetization state of a magnetic structure might be of interest. This information can be obtained non-destructively from measurements of the magnetic stray field generated by the structure. This process is referred to as source reconstruction.

Both these tasks, optimal design, and source reconstruction can be formulated as inverse problems. When solving an inverse problem, one is interested in deducing the cause that leads to a known effect. Within this thesis, the effect is the magnetic stray field and the cause is the properties of the respective magnetic structure. Since the considered magnetic structures are macroscopic in size and steady currents are assumed, the physics of the examined systems are covered by magnetostatics. The magnetic stray field of a magnetic structure can be calculated from partial differential equations, Maxwell's equations. The corresponding inverse problem, the magnetostatic inverse problem can therefore be solved within the framework of optimization problems with partial differential equation constraints, i.e., partial differential equation-constrained optimization. Within this approach, the gradient necessary to solve the inverse problem iteratively can be obtained efficiently using the adjoint method.

Within this thesis, the appearing partial differential equations are solved using hybrid finite element method - boundary element method approaches. In order to efficiently solve the inverse magnetostatic problem using these methods, the formalism of partial differential equation-constrained optimization is used and expressions for the gradient, necessary to perform the optimizations, are derived. Based on these methods, a software package capable of performing optimal design and source reconstruction of hard as well as soft magnetic structures has been developed. To showcase the capabilities of the developed algorithm several examples, namely the topology optimization of hard as well as soft magnetic structures and the source reconstruction of a magnetic structure are presented.

Kurzzusammenfassung

Magnetische Strukturen spielen in einer Vielzahl von Anwendungen eine Schlüsselrolle. Damit sie ihre spezifische Funktion erfüllen können, müssen die betreffenden hart- oder weichmagnetischen Werkstoffe entworfen werden. Der Entwurfsprozess kann die Gestaltung der äußeren Eigenschaften der Strukturen, d.h. ihrer Form, oder die Gestaltung ihrer inneren Eigenschaften, d.h. ihres Magnetisierungszustands, umfassen. In den allermeisten Fällen bezieht sich das Ziel des Gestaltungsprozesses dabei auf das magnetische Streufeld, das Magnetfeld welches von den magnetischen Strukturen erzeugt wird.

Ein weiterer wichtiger Aspekt betrifft die Untersuchung magnetischer Strukturen. Beispielsweise kann es bei der Qualitätskontrolle von Interesse sein, Informationen über den Magnetisierungszustand einer magnetischen Struktur zu erhalten. Diese Information kann zerstörungsfrei aus Messungen des von der Struktur erzeugten magnetischen Streufeldes gewonnen werden. Dieser Prozess wird als Quellenrekonstruktion bezeichnet.

Beide Aufgaben, optimaler Entwurf und Quellrekonstruktion, können als inverse Probleme formuliert werden. Bei der Lösung eines inversen Problems ist man daran interessiert, die Ursache zu ermitteln, die zu einer bekannten Wirkung führt. In der vorliegenden Arbeit bezieht sich die Wirkung auf das magnetische Streufeld und die Ursache sind die Eigenschaften der jeweiligen magnetischen Struktur. Da die betrachteten magnetischen Strukturen makroskopische Ausmaße haben und stationäre Ströme angenommen werden, wird die Physik der untersuchten Systeme durch die Theorie der Magnetostatik beschrieben. Das magnetische Streufeld einer magnetischen Struktur lässt sich mittels partieller Differentialgleichungen, den sogenannten Maxwell-Gleichungen, berechnen. Das entsprechende inverse Problem, das magnetostatische inverse Problem, kann daher auf Grundlage der Optimierung mit partiellen Differentialgleichungen gelöst werden. Im Rahmen dieses Ansatzes kann der Gradient, der zur iterativen Lösung des inversen Problems erforderlich ist, mit Hilfe der adjungierten Methode effizient ermittelt werden.

In dieser Doktorarbeit werden die auftretenden partiellen Differentialgleichungen mit Hilfe hybrider Finite-Elemente-Methode-Randelement-Methode-Ansätze gelöst. Um das inverse magnetostatische Problem mit diesen Methoden effizient zu lösen, wird der Formalismus der Optimierung mit partiellen Differentialgleichungen herangezogen und es werden Ausdrücke für den Gradienten abgeleitet, der zur Durchführung der Optimierungen erforderlich ist. Auf der Grundlage dieser Methoden wurde ein Softwarepaket für die optimale Auslegung und Quellenrekonstruktion von hart- und weichmagnetischen Strukturen implementiert. Um die Möglichkeiten des entwickelten Algorithmus zu demonstrieren, werden mehrere Beispiele, nämlich die Topologieoptimierung hart- und weichmagnetisher Strukturen und die Quellrückrechnung einer Magnetstruktur, präsentiert.

Publications

The scientific results that are presented within this thesis have been partially published within the following publications:

[1] Gregor Wautischer et al. "Topology optimization of a heat-assisted magnetic recording write head to reduce transition curvature using a binary optimization algorithm utilizing the adjoint method". In: *Scientific Reports* 12.1 (Aug. 2022), p. 13986. DOI: 10.1038/s41598-022-18112-z.

[2] Gregor Wautischer et al. "A topology optimization algorithm for magnetic structures based on a hybrid FEM–BEM method utilizing the adjoint approach". In: *Scientific Reports* 12.1 (Jan. 2022), p. 1119. DOI: 10.1038/s41598-021-04246-z.

[3] Gregor Wautischer et al. "Solving the inverse magnetostatic problem using fictitious magnetic charges". In: *AIP Advances* 8.5 (May 2018), p. 056005. DOI: 10.1063/1.5007348.

Contents

1. Introduction

1.1. Background

Devices whose functionality is based on the magnetic interaction have a wide range of applications. Be it magnetic recording devices [1], magnetic sensors used e.g. in the automotive industry [2, 3, 4, 5], magnetic cooling devices [6], or electric motors [7], to name just a few, magnetism plays an important part in modern technology. In order to create these devices, the involved magnetic structures, consisting of soft as well as hard magnetic materials are designed to optimally perform their specific function [8]. Most commonly they are designed to produce a magnetic field, the demagnetization or stray field, with a well-defined, specific spatial distribution according to some design objective. This includes magnetic fields generated by permanent magnetic structures as well as magnetic fields generated by electric currents whose spatial distribution is influenced by soft magnetic structures in the vicinity, or even by combinations of the two.

The demagnetization field of a magnetic structure is generated from its magnetization distribution. For a given material (defined by a B/H curve) the spatial characteristics of the magnetic field depend, for the case of permanent magnetic material, on the direction of the anisotropy axis and on the magnetization process. For soft magnetic materials, due to demagnetization effects, additionally, the shape of the magnetic structure constitutes a contribution. All three mentioned properties can be designed to obtain the desired magnetic field distribution. The problem of finding the best design to satisfy a given objective is called optimal design.

In order to realize a magnet design, the magnetic structure can be produced by a wide range of methods. For permanent magnets, the possibility to produce polymer-bonded magnets has significantly improved the ability to design their generated magnetic field [9]. Using injection molding, not only can complex shapes be produced economically, but furthermore, their magnetization state can be influenced during the molding process. This is done by applying a multi-polar magnetic field during cooling [10]. The applied field orients the magnetic filler inside the polymer melt, thereby shaping the final magnetization state. Note that additionally, this method makes a subsequent magnetization of the magnet structure unnecessary. For isotropic hard magnetic materials, a related method can be used to shape the magnetization state of the final magnetic structure. There, while a common molding process without an applied magnetic field is used to create the structure, a well-defined magnetic field is applied during the subsequent magnetization process. The spatial distribution of this magnetic field completely defines the final magnetization state [11]. Note that furthermore, with 3D printing, recently an additional method to produce polymer-bonded magnets with complex shapes has been developed [12, 13, 14, 15]. This method is especially useful for rapid prototyping without the necessity of first producing a complex mold.

After the design process, during the prototyping state, it has to be ensured, that the obtained magnetization state of a magnetic structure coincides with the desired magnetization state.

This problem is referred to as a source identification or source reconstruction problem. Source reconstruction problems additionally appear in quality control, where it has to be ensured that a stable function of the magnetic structure is guaranteed during its lifetime [16]. Both these tasks can be achieved by reconstruction of the magnetization state from measurements of the magnetic field generated by the magnetic structure.

Optimal design as well as source reconstruction, can both be efficiently solved using the theory and formalism of inverse problems.

1.1.1. The inverse magnetostatic problem

Whereas solving the forward problem in the case of magnetostatics means calculating the magnetic field of a given magnetic structure, solving the inverse problem means obtaining information about the magnetic structure given information of its created or desired stray field.

Following [17], a general forward problem can be defined as

$$Gm = d, \tag{1.1}$$

where G is the forward operator, m are the model parameters and d are, possibly measured data. Solving the inverse problem then means finding m given d. Inverse problems in general are subject to several difficulties. These have to do with:

- solution existence
- solution uniqueness
- solution stability.

This means that, if no solution exists for an inverse problem, or the existing solution is not unique, i.e. it has several solutions, or the solution is unstable in the sense that it does not depend continuously on the input data, the problem is said to be ill-posed.

When considering magnetic structures the forward problem is governed by Maxwell's equations as will be introduced in chapter 3. Since Maxwell's equations are partial differential equations (PDEs) within this thesis techniques from partial differential equation (PDE)-constrained optimization [18] are used to solve the inverse magnetostatic problem.

While for the case of optimal design, the existence of a solution for a given setup depends on the desired objective, when solving the source reconstruction problem, as mentioned in [17] "there may be no model that exactly fits a given data set if our mathematical model of the system's physics is approximate and/or if the data contains noise". However, when using PDE-constrained optimization, as will be seen, to perform source reconstruction, an iterative minimization of the difference between the calculated field, starting from an initial state, and the input field is minimized. Therefore, here always some kind of solution exists and the question is only how well the obtained solution represents the true source. Also, here the problem of solution uniqueness arises since several configurations might represent the true source equally well with respect to some metric. A regularization procedure can in this case be applied to choose a configuration with desired properties. This will be discussed in more detail in chapter 5 where it is appropriate. Additionally, when dealing with source reconstruction problems, due to unavoidable noise in the measurement data, solution stability becomes important. For unstable problems, small changes in the measurement data due to noise can lead to enormous changes within the reconstructed

source. This dependence of the reconstructed source on small changes in the measurement data can also be decreased by employing regularization techniques, increasing solution stability. This is, as discussed in more detail in chapter 5 since regularization can suppress features in the source present only due to the noise. Note that also during optimal design some kind of regularization might be necessary in order to enforce constraints onto a given design parameter (see chapter 4).

1.2. Aim and structure of the doctoral thesis

Within this thesis, the optimal design and source reconstruction of magnetic structures is discussed. Based on Maxwell's equations, an efficient way to solve the inverse magnetostatic problem is developed within the formalism of PDE-constrained optimization. The inverse magnetostatic problem is therein solved iteratively and the necessary gradients are obtained using the adjoint approach.

Based on the developed method, a software package to perform optimal design and source reconstruction of hard as well as soft magnetic structures has been implemented. The software package is written in python and is based on the micromagnetic tool magnum.fe [19] that in turn utilizes the finite element library FEniCS [20]. Regarding optimal design, it allows for the optimization of the topology of soft as well as hard magnetic structures defined by a possibly non-linear B/H curve, as well as for the optimization of the magnetization distribution inside a hard magnetic structure. Concerning source reconstruction, it allows for the reconstruction of the magnetization state or the topology of a magnetic structure from measurements of its magnetic stray field.

The thesis is structured as follows. Within the next chapter (chapter 2) PDE-constrained optimization is introduced and the formalism necessary to solve the inverse magnetostatic problem is presented. Thereafter, in chapter 3 the numerical methods used to solve the governing partial differential equations are presented and discussed. Following in chapter 4 topology optimization is introduced and as examples, the topology of hard as well as soft magnetic thin film flux guide concentrators and a magnetic recording write head is optimized. In chapter 5 then the source reconstruction of magnetic structures is discussed and the source reconstruction of a magnetic unit cube is presented as an example. The thesis finishes with a summary and an outlook given in chapter 6.

2. Partial differential equation-constrained optimization and the adjoint method

Within this chapter, the foundations of optimization constrained by partial differential equations, i.e. partial differential equation-constrained optimization, are presented. First, the general optimization problem is introduced. Its iterative optimization is then discussed and the necessary gradient is derived. Finally, the adjoint method, an efficient way to obtain the gradient, is presented. The following explanations and derivations mainly follow [18] and [21], from where also the mathematical definitions and theorems were taken. Parts of this section have been published in [22].

2.1. Partial differential equation-constrained optimization

Partial differential equations (PDEs) appear in a wide range of fields, describing phenomena like diffusion or heat transfer, to just name a very few, and as considered in this thesis, magnetic fields. By tuning the different parameters appearing inside of PDEs one can model systems and optimize them towards desired function goals. This is called Partial differential equation (PDE)-constrained optimization.

Consider a general, linear elliptic PDE in its residual form $F(x) = 0$ with given boundary conditions. Since the state variable x is obtained by solving the PDE we call F the state equation or forward problem. In order to perform an optimization, a control or design variable p is introduced $F(x) \to F(x, p)$. Furthermore, the optimization goal has to be formulated as an objective functional $J(x, p)$.

The PDE-constrained optimization problem can then be written as follows:

$$\min_{x \in X,\, p \in P} J(x, p) \quad \text{subject to} \quad F(x, p) = 0, \tag{2.1}$$

where $J : X \times P \to \mathbb{R}$ and $F : X \times P \to Z$. Note, within this thesis hybrid finite element method - boundary element method (FEM-BEM) approaches are used to solve the appearing PDEs. There, the weak formulation, involving an inner product with appropriate test functions is used and the appearing function spaces, as also X, P and Z are therefore Hilbert spaces.

When solving the forward problem, the state variable x is obtained for a given value of the design variable p. Assuming that the forward problem has a unique corresponding solution x for each p, we can define an abstract solution operator $x(p) : P \to X$. Inserting this solution operator into J leads to the reduced objective functional

$$\hat{J}(p) \coloneqq J(x(p), p). \tag{2.2}$$

Here it is important to realize that $\hat{J}$ depends on p implicitly via the forward problem and may also depend on p explicitly. The implicit dependence constitutes the PDE constraint.

2.2. Optimization, derivative and gradient of $\hat{J}$

In order to develop a way to solve a PDE-constrained optimization problem, the properties of the reduced objective functional $\hat{J}(p)$ have to be further investigated. To this aim, the following definition introduces the concept of duality. Note, that the following definitions will be introduced for Banach spaces. However, since all Hilbert spaces are also Banach spaces, this generalization does not restrict the validity for the FEM case.

Definition 1 (Linear functionals, dual space, dual pairing and dual basis) *Let V be a Banach space. A bounded linear operator $I : V \to \mathbb{R}$, i.e., $I \in \mathcal{L}(V, \mathbb{R})$ is called a bounded **linear functional** on V.*

*The space $V^* \coloneqq \mathcal{L}(V, \mathbb{R})$ of linear functionals on V is called the **dual space** of V and is a Banach space. Note, that V is adequately referred to as primal space. In the same way as for the primal space, a basis - the **dual basis** - can be defined on V^* (see section A.1 in the appendix).*

*The **dual pairing** $\langle \cdot, \cdot \rangle_{V^*,V}$ of V^* and V is denoted by*

$$\langle I, v \rangle_{V^*,V} \coloneqq I(v). \tag{2.3}$$

The reduced objective functional $\hat{J}(p)$ is exactly an element of the dual space P^* of P. To solve the PDE-constrained optimization problem, $\hat{J}(p)$ has to be minimized. To do so, any kind of minimization algorithm can be used. In the following, an iterative minimization approach starting from an initial configuration of the control variable p_{init} is discussed. To perform an iterative minimization, an update p_{update} to the current control variable value p_i is needed. Since p_{update} should be a value, that further reduces the objective functional, a candidate would be the negative derivative of $\hat{J}(p)$. In order to obtain it, first the Fréchet differentiability, a generalization of differentiability from functions on Euclidean space [21], has to be introduced.

Definition 2 (Fréchet derivatives) *A functional $I : U \subset V \to \mathbb{R}$, where V is a Banach spaces and U is an open set $U \neq \emptyset$ is called directionally differentiable at $v \in U$ if*

$$\mathrm{d}I(v; h) \coloneqq \lim_{\epsilon \to 0^+} \frac{I(v + \epsilon h) - I(v)}{\epsilon}, \tag{2.4}$$

exists for all $h \in U$. Here we introduced the notation $\mathrm{d}I(v; h)$ that indicates that $\mathrm{d}I$ depends on the element in front of the semicolon $v \in U$ and is applied to the element after the semicolon $h \in U$. If furthermore, the directional derivative $\mathrm{d}I(v; \cdot) : V \ni h \mapsto \mathrm{d}I(v; h) \in \mathbb{R}$ is bounded and linear, i.e. $\mathrm{d}I(v; \cdot) \in V^* \quad \forall u \in U$, I is Gâteaux-differentiable. If additionally

$$\lim_{\|h\|_V \to 0} \frac{\|I(v + h) - I(v) - \mathrm{d}I(v; h)\|}{\|h\|_V} = 0 \quad \forall v \in U \tag{2.5}$$

exists, I is Fréchet-differentiable.

Therefore, $\mathrm{d}\hat{J}(p; \cdot)$, the directional derivative of $\hat{J}(p)$ is also an element of the dual space P^*. Considering now, that a basic iterative minimization algorithm updates the current value of the control as $p_{i+1} = p_i + \gamma\, p_{\text{update}}$, where γ is a parameter for the step length. Since the control p is an element of the primal space P using the derivative $\mathrm{d}\hat{J}(p; \cdot) \in P^*$ as update is the wrong choice. What is needed, is an element of the primal space P, the gradient $\nabla \hat{J}_p$. To obtain the gradient, the Riesz representation theorem has to be introduced.

Theorem 1 (Riesz representation theorem) *The dual space H^* of a Hilbert space H is isometric to H itself. More precisely, for every $w \in H$ there exists a linear functional I defined by*

$$\langle I, v \rangle_{H^*,H} \coloneqq (w, v)_H \quad \forall v \in H, \tag{2.6}$$

where $(w, v)_H$ is the inner product defined on H and I is in H^* with norm $||I||_{H^*} = ||w||_H$. Vice versa, for any $I \in H^*$ there exists a unique $w \in H$ such that

$$\langle I, v \rangle_{H^*,H} = (w, v)_H \quad \forall v \in H \tag{2.7}$$

and $||I||_{H^*} = ||w||_H$.

This means, that any element I of the dual space H^* can be uniquely represented by an element w of the primal space H.

Definition 3 (Riesz map) *The **Riesz map** $\mathcal{R}_H : H^* \to H$ is the operation that converts a functional $I \in H^*$ to its unique representation $w \in H$, where $w = \mathcal{R}_H(I)$ is called the Riesz representer of I in H with respect to the inner product defined on H.*

The gradient $\nabla \hat{J}_p$ can now be identified as the Riesz representer $\mathcal{R}_P\left(\mathrm{d}\hat{J}(p)\right) \in P$ of the derivative $\mathrm{d}\hat{J}(p; \cdot) \in P^*$.

$$\mathrm{d}\hat{J}(p; s) = \left\langle \mathrm{d}\hat{J}(p), s \right\rangle_{P*,P} = \left(\mathcal{R}_P\left(\mathrm{d}\hat{J}(p)\right), s\right)_P = \left(\nabla \hat{J}_p, s\right)_P \tag{2.8}$$

Note that in the following $\mathcal{R}_H$ is called the Riesz representer and the specific reference to the Hilbert space H is dropped, whenever it can be derived from context to which Hilbert space the Riesz representer belongs. How the Riesz representer can be obtained in detail within the used finite element (FE) scheme, is shown within the appendix (section A.2). There, for the case of using the L^2 inner product as done within this thesis, it is shown that the gradient is obtained from the derivative by multiplication with the inverse mass matrix. To illustrate the difference between the derivative and the gradient a simple example can be considered. In Figure 2.1a the function $f = x$, where x corresponds to the x-coordinate, on a finite element mesh with two different element sizes, using basis functions constant within each element is shown. Using the objective functional $\hat{J} = \int_\Omega 2\, f \,\mathrm{d}V$ the corresponding derivative $\mathrm{d}\hat{J}_x$ and gradient $\nabla \hat{J}_x$ are show in Figure 2.1b and Figure 2.1c respectively. It can be seen, that while the values of the derivative are different within differently-sized elements this is not the case for the gradient, where all values are equal. This shows, that the multiplication with the inverse mass matrix removed the weighting of the dofs with the respective element size. Using the gradient, an optimization based on an iterative minimization algorithm can now be performed. Note that the minimization itself is done within the defined Hilbert spaces using the corresponding inner product. Since more complex minimization algorithms internally e.g. calculate approximations for the Hessian matrix like e.g. algorithms based on the method of Broyden-Fletcher-Goldfarb-Shannon (BFGS), it should be ensured that during these calculations the correct inner product is used. Otherwise, mesh dependency can occur during optimization as covered in detail in [21]. The algorithms used within this thesis are discussed regarding the usage of the inner product and furthermore the usage of the derivative and the gradient is investigated experimentally.

In the next section, a way to efficiently calculate the gradient for a given objective functional is introduced.

(a) (b) (c)

Figure 2.1.: Simple example showing the difference of the derivative and the gradient. In (a) the function $f = x$ where x refers to the x-coordinate is shown. The derivative $\mathrm{d}\hat{J}_x$ and the gradient $\nabla\hat{J}_x$ of the objective functional $\hat{J} = \int_\Omega 2\, f \,\mathrm{d}V$ are shown in (b) and (c) respectively.

2.3. The adjoint method

In the context of PDE-constrained optimization, the adjoint method is a tool to efficiently calculate the derivative and thereby the gradient of the reduced objective functional with respect to the design variable $\nabla\hat{J}_p$. Using a FE scheme to solve F, the design variable p introduces a number n_p of degrees of freedom (dofs) as input variables into the PDE, which is typically large. On the other hand, the objective functional value as the output value is a scalar. Using, e.g. the finite difference approach, the derivative in a direction δp is approximated by computing the difference quotient, e.g. by the central difference formula:

$$d\hat{J}\left(p;\delta p\right) = \frac{\hat{J}\left(p + h\delta p\right) - \hat{J}\left(p - h\delta p\right)}{2h} + \mathcal{O}\left(|h|^2\right) \quad \text{as} \quad h \to 0. \tag{2.9}$$

In order to obtain the full derivative, this formula would have to be solved once for each degree of freedom $\delta p = \psi_i$ where ψ_i is the basis function corresponding to each dof. This equals solving the forward PDE $2n_p$ times and the number of necessary forward solves to calculate the derivative grows linearly with n_p. The advantage of the adjoint method over the finite difference approximation or similar methods like the tangent linear (or sensitivity) approach is, that the number of PDE solves required to obtain the derivative is independent of the number of input variables n_p. In fact, to obtain the derivative, the adjoint approach only requires the solution of the forward problem once and an additional solve of the so-called adjoint equation, an equation of similar complexity as the forward problem, that will be introduced below. Furthermore, as will be seen, for self-adjoint operators, the adjoint equation even is of the same form as the forward problem and therefore, the derivative can be calculated by solving two similar equations once.

The adjoint approach is now applied to obtain the gradient $\nabla\hat{J}_p$ of the reduced objective function $\hat{J}\left(p\right)$ with respect to the design variable p. A "first optimize then discretize" scheme [18] is used, within which the gradient is derived using continuous operators.

Following [18], in order to derive the gradient $\nabla\hat{J}_p$, first the derivative

$$\mathrm{d}\hat{J}\left(p;\cdot\right) = \partial J_x\left(x\left(p\right), p; \mathrm{d}x_p\left(p;\cdot\right)\right) + \partial J_p\left(p;\cdot\right) \quad \in P^*, \tag{2.10}$$

where ∂J_x and ∂J_p denote the partial derivatives of J with respect to the state and control variable x and p respectively, is considered. For ease of readability from here on the function arguments are dropped giving

$$\mathrm{d}\hat{J}_p = \partial J_x \mathrm{d}x_p + \partial J_p, \tag{2.11}$$

where it has been used, that in the same way as in Euclidean space, the partial and total derivatives in Hilbert spaces are related by the chain rule [21]. Note however, that $\mathrm{d}\hat{J}_p$ here still

is an abstract element of P^* that only has a concrete representation when applied to an element in P.

The numerically challenging term here is $\mathrm{d}x_p$ since the state variable x depends on the control variable p via the forward problem F. Naive evaluation of $\mathrm{d}x_p$ in the discretized form by means of the finite difference formula would again require $2n_p$ solves of the forward problem. However, $\mathrm{d}x_p$ can be avoided since the derivative of the forward problem reads

$$\mathrm{d}F_p = \partial F_x \mathrm{d}x_p + \partial F_p = 0. \tag{2.12}$$

Therefore, the critical term can be written as

$$\mathrm{d}x_p = -\partial F_x^{-1} \partial F_p. \tag{2.13}$$

which after inserting into equation (2.11) leads to an expression

$$\mathrm{d}\hat{J}_p = -\partial J_x \partial F_x^{-1} \partial F_p + \partial J_p, \tag{2.14}$$

where $\mathrm{d}x_p$ has been eliminated.

Using the Riesz representation theorem (Theorem 1), as shown in equation (2.8), this can be written as

$$\mathrm{d}\hat{J}\left(p; s\right) = \left(\nabla \hat{J}_p, s\right)_P = -\left(\mathcal{R}\left(\partial J_x\right), \partial F_x^{-1} \partial F_p s\right)_X + \left(\mathcal{R}\left(\partial J_p\right), s\right)_P, \tag{2.15}$$

where $\mathcal{R}$ denotes the respective Riesz representer as introduced in Definition 3.

To continue, the definition of the dual operator is needed.

Definition 4 (Dual operator) *Let V, W be Banach spaces. Then for an operator $A \in \mathcal{L}\left(V, W\right)$ the **dual operator** $A^* \in \mathcal{L}\left(W^*, V^*\right)$ is defined by*

$$\left\langle A^*\left(v\right), u\right\rangle_{V^*,V} = \left\langle v, A\left(u\right)\right\rangle_{W^*,W} \quad \forall u \in V, v \in W^* \tag{2.16}$$

where if V and W are Hilbert spaces , again the dual pairing is identical to the inner product and therefore

$$\left(A^*\left(v\right), u\right)_V = \left(v, A\left(u\right)\right)_W \quad \forall u \in V, v \in W. \tag{2.17}$$

It therefore follows

$$\left(\nabla \hat{J}_p, s\right)_P = -\left(\partial F_p^* \partial F_x^{-*} \mathcal{R}\left(\partial J_x\right), s\right)_P + \left(\mathcal{R}\left(\partial J_p\right), s\right)_P, \tag{2.18}$$

where $\partial F_x^{-*} = \left(\partial F_x^{-1}\right)^*$ denotes the adjoint of the inverse of ∂F_x, and the gradient $\nabla \hat{J}_p$ can be extracted as

$$\nabla \hat{J}_p = -\partial F_p^* \partial F_x^{-*} \mathcal{R}\left(\partial J_x\right) + \mathcal{R}\left(\partial J_p\right). \tag{2.19}$$

Looking at $\partial F_x^{-*} \mathcal{R}\left(\partial J_x\right)$, $\mathcal{R}\left(\partial J_x\right)$ can be identified as an element of the primal space X and ∂F_x^{-*} as a mapping $X \to Z$. We can therefore represent $\partial F_x^{-*} \mathcal{R}\left(\partial J_x\right)$ as a new variable $\lambda \in Z$ that is called the adjoint variable

$$\lambda = \partial F_x^{-*} \mathcal{R}\left(\partial J_x\right) \tag{2.20}$$

and rearranging gives the adjoint equation

$$\partial F_x^* \lambda = \mathcal{R}\left(\partial J_x\right). \tag{2.21}$$

The adjoint equation can be used to efficiently calculate the adjoint variable λ. In fact it will be shown, that in case of a self-adjoint forward operator F the adjoint equation is of the same form as F and the gradient

$$\nabla \hat{J}_p = -\partial F_p^* \lambda + \mathcal{R}\left(\partial J_p\right) \quad \in P \tag{2.22}$$

can be obtained very efficiently by solving two similar equations once.

The adjoint operators ∂F_p^* and ∂F_x^* can be obtained using the definition of dual operators in Hilbert spaces (equation (2.17)). They are derived in detail for each presented example.

In the next chapter, the forward problems considered within this thesis and the algorithms used to solve them are presented.

3. Solving the magnetostatic forward problem

Since within this thesis, the design and source reconstruction of macroscopic magnetic structures is covered, the basis of all PDE-constrained optimization problems that are treated are the magnetostatic equations. In this chapter, the magnetostatic equations are derived and the applied techniques to solve them numerically are discussed.

3.1. The full magnetostatic Maxwell problem

We first derive the full, self-consistent magnetostatic Maxwell problem. Maxwell's equations for magnetostatics are obtained from Maxwell's equations by assuming that the electric charges are fixed or moving as a steady current $\boldsymbol{j}$ leading to an electric field $\boldsymbol{E}$ constant in time $\frac{\partial \boldsymbol{E}}{\partial t} = 0$ and by assuming slowly changing magnetic fields implying that the time derivatives of the magnetic field variables can be neglected $\frac{\partial \boldsymbol{B}}{\partial t} = 0$, where $\boldsymbol{B}$ is the magnetic flux. Maxwell's equations then decouple resulting in the equations for electrostatics and magnetostatics. For magnetostatics, Gauss's law for magnetism

$$\boldsymbol{\nabla} \cdot \boldsymbol{B} = 0 \tag{3.1}$$

and Ampère's law

$$\boldsymbol{\nabla} \times \boldsymbol{H} = \boldsymbol{j} \tag{3.2}$$

are the relevant equations.

3.1.1. Derivation of the demagnetization field

An expression for the magnetic demagnetization or stray field can be obtained by considering that the magnetic flux density $\boldsymbol{B}$ is connected to the magnetic field $\boldsymbol{H}$ and the magnetization $\boldsymbol{M}$ by

$$\boldsymbol{B} = \mu_0 \left(\boldsymbol{H} + \boldsymbol{M} \right), \tag{3.3}$$

where μ_0 is the vacuum permeability.

Using the reduced magnetic scalar potential formulation (or Φ-formulation) [23, 24], the total magnetic field $\boldsymbol{H}$ can be split into two parts

$$\boldsymbol{H} = \boldsymbol{H}_{\text{ext}} + \boldsymbol{H}_{\text{d}}. \tag{3.4}$$

Here $\boldsymbol{H}_{\text{ext}}$ is an external magnetic field independent of the present magnetic parts, but produced by an external current $\boldsymbol{j}$ following Ampère's law (equation (3.2)), giving $\boldsymbol{\nabla} \times \boldsymbol{H}_{\text{ext}} = \boldsymbol{j}$. Note, that $\boldsymbol{j}$ is referred to as external since it is outside of the domain where the demagnetization field is to be calculated. Furthermore note, that since $\boldsymbol{H}_{\text{ext}}$ is independent of present magnetic

structures, inserting equation (3.3) with $\boldsymbol{M} = 0$ into equation (3.1) leads to $\boldsymbol{\nabla} \cdot \boldsymbol{H}_{\text{ext}} = 0$. $\boldsymbol{H}_{\text{d}}$, the demagnetization (or stray) field, on the other hand, is generated from the magnetic parts. Since $\boldsymbol{\nabla} \times \boldsymbol{H}_{\text{ext}} = \boldsymbol{j}$, it follows from Ampère's law that it is rotational-free $\boldsymbol{\nabla} \times \boldsymbol{H}_{\text{d}} = 0$, and it can therefore be expressed as the gradient of a scalar potential u,

$$\boldsymbol{H}_{\text{d}} = -\boldsymbol{\nabla} u. \tag{3.5}$$

It, therefore, follows

$$\boldsymbol{B} = \mu_0 \left(\boldsymbol{H}_{\text{ext}} - \boldsymbol{\nabla} u + \boldsymbol{M} \right). \tag{3.6}$$

Furthermore the relationship between the magnetization $\boldsymbol{M}$ and the field $\boldsymbol{H}$ for a general magnetic material is given by

$$\boldsymbol{M} = \chi \left(\boldsymbol{H} \right) \boldsymbol{H} + \boldsymbol{M}_{\text{r}}, \tag{3.7}$$

where $\boldsymbol{M}_{\text{r}}$ is the remanence magnetization of a permanent magnetic material in direction of its easy axis and $\chi \left(\boldsymbol{H} \right)$ is the, possibly non-linear, magnetic susceptibility. Splitting $\boldsymbol{H}$ again as above one gets, after inserting into equation (3.6)

$$\boldsymbol{B} = \mu_0 \left[\left(1 + \chi \left(\boldsymbol{H} \right) \right) \left(\boldsymbol{H}_{\text{ext}} - \boldsymbol{\nabla} u \right) + \boldsymbol{M}_{\text{r}} \right]. \tag{3.8}$$

Using Gauss's law (equation (3.1)) and eliminating μ_0 one can now get

$$F = \boldsymbol{\nabla} \cdot \left[\left(1 + \chi \left(\boldsymbol{H} \right) \right) \left(\boldsymbol{\nabla} u - \boldsymbol{H}_{\text{ext}} \right) - \boldsymbol{M}_{\text{r}} \right] = 0, \tag{3.9}$$

a generalized *Laplace-Poisson equation*. Demanding that the magnetic material is localized the following open boundary condition

$$u \left(\boldsymbol{r} \right) \to \mathcal{O} \left(\frac{1}{|\boldsymbol{r}|} \right) \quad \text{for} \quad |\boldsymbol{r}| \to \infty \tag{3.10}$$

holds and equation (3.9) together with this boundary condition is called an open boundary problem.

3.1.2. Solving the full magnetostatic Maxwell problem

The full magnetostatic Maxwell problem as defined by equations (3.9) and (3.10) can be solved using a hybrid FEM-BEM algorithm based on a FEM-BEM coupling method developed by Johnson and Nédélec. A detailed description can be found in [26]. Here just a short summary is presented.

As a first step, $\mathbb{R}^3$ is divided into a region Ω_{m} containing all magnetic material and a region $\mathbb{R}^3 \backslash \Omega_{\text{m}}$ leading to

$$\boldsymbol{\nabla} \cdot \left[\left(1 + \chi^+ \right) \left(\boldsymbol{H}_{\text{ext}} - \boldsymbol{\nabla} u^+ \right) + \boldsymbol{M}_{\text{r}}^+ \right] = 0 \quad \text{in} \quad \Omega_{\text{m}} \tag{3.11}$$

and

$$\Delta u^- = 0 \quad \text{in} \quad \mathbb{R}^3 \backslash \Omega_{\text{m}}, \tag{3.12}$$

with jump conditions

$$[u]_{\partial \Omega_{\text{m}}} = u^+ - u^- = 0, \tag{3.13}$$

$$\left[\left(1 + \chi \right) \frac{\partial u}{\partial \boldsymbol{n}} \right]_{\partial \Omega_{\text{m}}} = \boldsymbol{n} \cdot \left(\chi^+ \boldsymbol{H}_{\text{ext}} + \boldsymbol{M}_{\text{r}}^+ \right) \tag{3.14}$$

and boundary condition

$$u(\boldsymbol{r}) \to \mathcal{O}\left(\frac{1}{|\boldsymbol{r}|}\right) \quad \text{for} \quad |\boldsymbol{r}| \to \infty. \tag{3.15}$$

Here, the variables living inside Ω_m have been denoted with $^+$ and the ones living in $\mathbb{R}^3 \backslash \Omega_\mathrm{m}$ with $^-$. Additionally $\frac{\partial u}{\partial \boldsymbol{n}} = \boldsymbol{\nabla} u \cdot \boldsymbol{n}$. Note that $\chi^- = 0$ and $\boldsymbol{M}_\mathrm{r}^- = 0$ since there is no magnetic material present outside of Ω_m. The jump conditions can be derived from the jump conditions of $\boldsymbol{B}$ and $\boldsymbol{H}$ at material interfaces.

Multiplying equation (3.11) by a test function v and integrating over the domain Ω_m, one gets the weak form

$$\int_{\Omega_\mathrm{m}} \boldsymbol{\nabla} \cdot \left[\left(1+\chi^+\right) \left(\boldsymbol{H}_\mathrm{ext} - \boldsymbol{\nabla} u^+ \right) + \boldsymbol{M}_\mathrm{r}^+ \right] v \, \mathrm{d}V = 0, \tag{3.16}$$

and after partial integration and rearrangement to have only terms including u on the left hand side,

$$\begin{gathered} \int_{\Omega_\mathrm{m}} \left(1+\chi^+\right) \boldsymbol{\nabla} u^+ \cdot \boldsymbol{\nabla} v \, \mathrm{d}V - \int_{\partial\Omega_\mathrm{m}} \left(1+\chi^+\right) \boldsymbol{\nabla} u^+ \cdot \boldsymbol{n} \, v \, \mathrm{d}S = \\ \int_{\Omega_\mathrm{m}} \left[\left(1+\chi^+\right) \boldsymbol{H}_\mathrm{ext} + \boldsymbol{M}_\mathrm{r}^+ \right] \cdot \boldsymbol{\nabla} v \, \mathrm{d}V - \int_{\partial\Omega_\mathrm{m}} \left[\left(1+\chi^+\right) \boldsymbol{H}_\mathrm{ext} + \boldsymbol{M}_\mathrm{r}^+ \right] \cdot \boldsymbol{n} \, v \, \mathrm{d}S. \end{gathered} \tag{3.17}$$

Introducing now a new variable $\phi = \frac{\partial u}{\partial \boldsymbol{n}}$ and using the jump condition of equation (3.14), this can be rewritten as

$$\begin{gathered} \int_{\Omega_\mathrm{m}} \left(1+\chi^+\right) \boldsymbol{\nabla} u^+ \cdot \boldsymbol{\nabla} v \, \mathrm{d}V - \int_{\partial\Omega_\mathrm{m}} \phi^- \, v \, \mathrm{d}S = \\ \int_{\Omega_\mathrm{m}} \left[\left(1+\chi^+\right) \boldsymbol{H}_\mathrm{ext} + \boldsymbol{M}_\mathrm{r}^+ \right] \cdot \boldsymbol{\nabla} v \, \mathrm{d}V - \int_{\partial\Omega_\mathrm{m}} \boldsymbol{H}_\mathrm{ext} \cdot \boldsymbol{n} \, v \, \mathrm{d}S. \end{gathered} \tag{3.18}$$

Equation (3.12) can be solved using the Green's function method by $G = \frac{1}{4\pi} \frac{1}{|\boldsymbol{x}-\boldsymbol{y}|}$, giving the following representation formula

$$\frac{1}{2} u^- = \int_{\partial\Omega_\mathrm{m}} \left(u^- \boldsymbol{\nabla} G - \boldsymbol{\nabla} u^- G \right) \boldsymbol{n} \, \mathrm{d}S. \tag{3.19}$$

Here, the two terms on the right hand side are called double and single layer potential respectively. Since u is continuous at the boundary (3.13) one gets

$$\frac{1}{2} u^+ - \int_{\partial\Omega_\mathrm{m}} \left(u^+ \boldsymbol{\nabla} G \boldsymbol{n} - \phi^- G \right) \mathrm{d}S = 0. \tag{3.20}$$

At this point, the equations are discretized using the Galerkin formalism by introducing finite element basis functions $\psi_i(\boldsymbol{r})$ and $\omega_i(\boldsymbol{r})$ for the variables as well as the test functions $u^+(\boldsymbol{r}) = \sum_j u_j \psi_j(\boldsymbol{r})$, $\phi^-(\boldsymbol{x}) = \sum_n \phi_n \omega_n(\boldsymbol{r})$. Note, that while $\psi_i(\boldsymbol{r})$ has to at least be piecewise linear ($\mathcal{P}_1$), $\omega_i(\boldsymbol{r})$ can be also chosen to be constant within each element. Equations (3.18) and (3.20) can now be written as a combined system of equations

$$\begin{pmatrix} M_{ij}^{11} & M_{in}^{12} \\ M_{mj}^{21} & M_{mn}^{22} \end{pmatrix} \begin{pmatrix} u_j \\ \phi_n \end{pmatrix} - \begin{pmatrix} \int_{\Omega_\mathrm{m}} \left[\left(1+\chi^+\right) \boldsymbol{H}_\mathrm{ext} + \boldsymbol{M}_\mathrm{r}^+ \right] \cdot \boldsymbol{\nabla} \psi_i \, \mathrm{d}V - \int_{\partial\Omega_\mathrm{m}} \boldsymbol{H}_\mathrm{ext} \cdot \boldsymbol{n} \, \psi_i \, \mathrm{d}S \\ \boldsymbol{0} \end{pmatrix}, \tag{3.21}$$

where the individual submatrices are given by

$$\begin{aligned} M_{ij}^{11} &= \int_{\Omega_\mathrm{m}} \left(1+\chi^{+}\right) \boldsymbol{\nabla}\psi_i \cdot \boldsymbol{\nabla}\psi_j \,\mathrm{d}V \\ M_{in}^{12} &= -\int_{\partial\Omega_\mathrm{m}} \psi_i \,\omega_n \,\mathrm{d}S \\ M_{mj}^{21} &= \frac{1}{2}\psi_j\left(\boldsymbol{r}_m\right) - \int_{\partial\Omega_\mathrm{m}} \psi_j \boldsymbol{\nabla} G_m \cdot \boldsymbol{n} \,\mathrm{d}S \\ M_{mn}^{22} &= \int_{\partial\Omega_\mathrm{m}} \omega_n G_m \,\mathrm{d}S. \end{aligned} \tag{3.22}$$

Note, that the big advantage of this method is, that only the region Ω_m, as well as its boundary, has to be spatially discretized, whereas discretization of the infinite outer region can be avoided. This reduces the number of degrees of freedom significantly compared to a pure FEM approach where also the surrounding space has to be discretized. While assembling M^{11} and M^{12} is rather straightforward, the compilation of the sub-matrices M^{21} and M^{22}, the double and single layer potential matrices respectively, responsible for the boundary part is rather involved and is done analytically as shown in [27].

For a given constant susceptibility χ equation (3.21) constitutes a linear system of equations that can be solved using a linear solver. However, if the susceptibility is a non-linear function depending on $\boldsymbol{H}$, an inexact Newton method has to be used to solve the full Maxwell problem. Using the obtained scalar potential u, the magnetic stray field $\boldsymbol{H}_\mathrm{d}$ can be calculated using equation (3.5), and the magnetization state of the involved magnetic structures can then be obtained from equation (3.7). However, note that $\boldsymbol{M}$ depends on the total magnetic field $\boldsymbol{H}$. In order to avoid cancellation errors when calculating the total magnetic field $\boldsymbol{H} = \boldsymbol{H}_\mathrm{ext} + \boldsymbol{H}_\mathrm{d}$ and in turn obtain a smooth expression for the magnetization, $\boldsymbol{H}_\mathrm{ext}$ has to fulfill $\boldsymbol{\nabla} \cdot \boldsymbol{H}_\mathrm{ext} = 0$, as mentioned above. This is ensured by considering that $\boldsymbol{\nabla} \times \boldsymbol{H}_\mathrm{ext} = 0$ within Ω_m. Therefore $\boldsymbol{H}_\mathrm{ext}$ can be expressed as the gradient of a scalar potential $\boldsymbol{H}_\mathrm{ext} = -\boldsymbol{\nabla} u_e$ and a divergence-free external field can be obtained by solving $\Delta u_e = 0$, where $\boldsymbol{H}_\mathrm{ext}$ only appears explicitly as Neumann boundary condition. An example of a magnetization state obtained using an external field with non-vanishing divergence can be seen in Figure 4.28a. Note, that furthermore, $\boldsymbol{H}_\mathrm{ext}$ and $\boldsymbol{H}_\mathrm{d}$ have to be defined using the same basis functions and since the potential u is defined using piecewise linear basis functions ($\mathcal{P}_1$), here, for $\boldsymbol{H}_\mathrm{ext}$ and $\boldsymbol{H}_\mathrm{d}$ basis function constant within each element are used.

Note, that while the continuous forward problem (equation (3.9)) is self-adjoint, as will be shown below (section 4.2), it is clearly visible that within the chosen discretization the discrete operator is not self-adjoint. This shows the necessity of using a "first optimize then discretize" scheme to derive the adjoint equation, as done above.

3.2. Magnetization as source

A possible simplification for the calculation of the demagnetization field is considering a fixed magnetization state as source. This approximation is useful when considering permanent magnetic materials with a low susceptibility where the demagnetization field does not significantly influence the magnetization state. Furthermore, using a magnetization configuration as source is useful when trying to reconstruct a magnetization configuration of a magnetic structure from the measured magnetic field as will be shown below.

3.2.1. Derivation of the demagnetization field

For a fixed magnetization state as source, no interaction of the magnetization with the demagnetization field as well as with an external field is considered. Therefore, $\boldsymbol{H}_{\mathrm{ext}} = 0$ and Ampère's law simplifies to

$$\boldsymbol{\nabla} \times \boldsymbol{H}_{\mathrm{d}} = 0 \tag{3.23}$$

This implies that the magnetic stray field $\boldsymbol{H}_{\mathrm{d}}$ is curl free and can therefore, again be written as the gradient of a scalar potential u

$$\boldsymbol{H}_{\mathrm{d}} = -\boldsymbol{\nabla} u. \tag{3.24}$$

Now using that

$$\boldsymbol{B} = \mu_0 \left(\boldsymbol{H}_{\mathrm{d}} + \boldsymbol{M} \right), \tag{3.25}$$

one gets with equation (3.1)

$$F = \boldsymbol{\nabla} \cdot \left(\boldsymbol{\nabla} u - \boldsymbol{M} \right) = 0. \tag{3.26}$$

This equation is continuous in all of $\mathbb{R}^3$, even if the magnetization $\boldsymbol{M}$ is discontinuous (e.g. at the boundary of a magnetic structure). Again, assuming the magnetic material to be localized, the following open boundary condition holds for u

$$u\left(\boldsymbol{r}\right) \to \mathcal{O}\left(\frac{1}{|\boldsymbol{r}|}\right) \quad \text{for} \quad |\boldsymbol{r}| \to \infty \tag{3.27}$$

and equation (3.26) together with this boundary condition becomes also an open boundary problem.

3.2.2. Solving the magnetostatic Maxwell problem with the magnetization as source

Within this thesis, the open boundary problem defined above is solved using a hybrid FEM-BEM approach based on the method of Fredkin and Koehler [28]. To this end, first, $\mathbb{R}^3$ is again split into a domain Ω_{m} containing all magnetic material and a domain $\mathbb{R}^3/\Omega_{\mathrm{m}}$. Denoting all variables inside Ω_{m} again with $^+$ and all in $\mathbb{R}^3/\Omega_{\mathrm{m}}$ with $^-$, equation (3.26) splits into

$$\boldsymbol{\nabla} \cdot \left(\boldsymbol{\nabla} u^+ - \boldsymbol{M} \right) \quad \text{in} \quad \Omega_{\mathrm{m}} \tag{3.28}$$

and

$$\Delta u^- = 0 \quad \text{in} \quad \mathbb{R}^3/\Omega_{\mathrm{m}}, \tag{3.29}$$

with jump conditions at the surface of the magnetic region

$$[u]_{\partial\Omega_\mathrm{m}} = 0 \tag{3.30}$$

and

$$\left[\frac{\partial u}{\partial \boldsymbol{n}}\right]_{\partial\Omega_\mathrm{m}} = -\boldsymbol{n}\cdot\boldsymbol{M}, \tag{3.31}$$

as well as the boundary condition

$$u(\boldsymbol{r}) \to \mathcal{O}\left(\frac{1}{|\boldsymbol{r}|}\right) \quad \text{for} \quad |\boldsymbol{r}| \to \infty. \tag{3.32}$$

The potential u is now split $u = u_1 + u_2$, where u_1 is the solution of the inhomogeneous Neumann problem

$$\boldsymbol{\nabla}\cdot\left(\boldsymbol{\nabla}u_1^+ - \boldsymbol{M}\right) \quad \text{in} \quad \Omega_\mathrm{m} \tag{3.33}$$

with boundary condition

$$\frac{\partial u_1^+}{\partial \boldsymbol{n}} = \boldsymbol{n}\cdot\boldsymbol{M} \quad \text{on} \quad \partial\Omega_\mathrm{m} \tag{3.34}$$

and is zero elsewhere $u_1^- = 0$. Note that this implies that u_1 jumps at the boundary $[u_1] = u_1^+$.

On the other hand, u_2^+ now must be a solution to

$$\Delta u_2^+ = 0 \quad \text{in} \quad \mathbb{R}^3 \tag{3.35}$$

where in order to satisfy the jump conditions from equation (3.30) and (3.31) it follows

$$[u_2]_{\partial\Omega_\mathrm{m}} = -u_1^+ \tag{3.36}$$

and

$$\left[\frac{\partial u_2}{\partial \boldsymbol{n}}\right]_{\partial\Omega_\mathrm{m}} = 0. \tag{3.37}$$

Furthermore

$$u_2(\boldsymbol{r}) \to \mathcal{O}\left(\frac{1}{|\boldsymbol{r}|}\right) \quad \text{for} \quad |\boldsymbol{r}| \to \infty \tag{3.38}$$

still has to hold.

A solution to Laplace's equation (equation (3.35)) that also satisfies the boundary conditions (equations (3.36) - (3.38)) is given by the double-layer potential

$$u_2 = \int_{\partial\Omega_\mathrm{m}} u_1 \boldsymbol{\nabla} G \,\mathrm{d}\boldsymbol{S}. \tag{3.39}$$

Therefore, in order to solve equation (3.28) first equation (3.33) can be solved by first multiplication with a test function v giving

$$\int_{\Omega_\mathrm{m}} \boldsymbol{\nabla}\cdot\left(\boldsymbol{\nabla}u_1^+ - \boldsymbol{M}\right) v \,\mathrm{d}V = 0 \tag{3.40}$$

and using partial integration on both sides leads to

$$\int_{\partial\Omega_\mathrm{m}} \boldsymbol{\nabla}u_1 \, v \,\mathrm{d}\boldsymbol{S} - \int_{\Omega_\mathrm{m}} \boldsymbol{\nabla}u_1 \cdot \boldsymbol{\nabla}v \,\mathrm{d}V = \int_{\partial\Omega_\mathrm{m}} \boldsymbol{M}\, v \,\mathrm{d}\boldsymbol{S} - \int_{\Omega_\mathrm{m}} \boldsymbol{M}\cdot\boldsymbol{\nabla}v \,\mathrm{d}V. \tag{3.41}$$

Using the boundary condition (3.34), the surface terms on both sides cancel, defining the boundary condition as natural. Using again the Galerkin formalism introducing finite element basis function for the variables as well as the test functions leads to a system of equations that can be solved to obtain u_1

$$\int_{\Omega_\mathrm{m}} \boldsymbol{\nabla}\psi_i \cdot \boldsymbol{\nabla}\psi_j \,\mathrm{d}V\, u_{1,j} = \int_{\Omega_\mathrm{m}} \boldsymbol{M} \cdot \boldsymbol{\nabla}\psi_i \,\mathrm{d}V. \tag{3.42}$$

Now, the double-layer potential (equation (3.39)) can be used to calculate u_2. While it is in principle possible to use the double-layer potential to obtain u_2 within Ω_m, in order to avoid having to assemble the complete double-layer potential matrix for each dof in Ω_m, equation (3.39) is used to evaluate u_2^+ only at the boundary. To do so the double-layer potential matrix is computed in the same way as above and u_2^+ on $\partial\Omega_\mathrm{m}$ is obtained by a simple matrix-vector multiplication. u_2^+ is then obtained by solving equation (3.35) using the same finite element calculation used to calculate u_1^+ (equations (3.40) - (3.42)) with the known boundary values as Dirichlet boundary condition.

The computation of the potential u, therefore, divides into three steps. First, u_1 is obtained by a finite element calculation where a linear system is solved. Then the boundary values of u_2 are obtained by a matrix-vector multiplication and finally, u_2 is obtained again by solving a linear system. This system is computationally less complex compared to solving the full Maxwell problem since on the one hand the two matrices involved in the finite element calculations are sparse and also the boundary method is reduced to a simple matrix-vector multiplication. Note, that even though here all matrices used are self-adjoint the complete forward problem in its discrete form is not, since the order of steps is not reversible. In the same way as for the full Maxwell problem, therefore the adjoint of the continuous problem (equation (3.26)) will be derived and applied.

4. Topology optimization

Within this chapter, the adjoint method is used to optimize the topology of hard as well as soft magnetic structures. First, the principles of topology optimization are explained and discussed. Then, the density approach for topology optimization is introduced. Thereafter, it is incorporated into the full Maxwell problem and the corresponding adjoint equation and the gradient are derived. As examples then the topology of a hard magnetic, as well as a soft magnetic thin film flux guide concentrator is optimized, and furthermore, the topology optimization of a magnetic write head used for heat-assisted magnetic recording is presented. The examples are used to investigate the influences of parameters present in the density approach for topology optimization and to compare the performance of different optimization algorithms. Furthermore, the usage of the derivative and the gradient is compared for selected examples. As an approximation for hard magnetic structures then, a scheme using the magnetization as source for the calculation of the demagnetization field is used. The topology optimization of a hard magnetic thin film flux guide concentrator is repeated using this method and the results from the two different approaches are compared. Parts of this chapter have previously been published in [29], [22] and [30].

Topology optimization tries to find, within a predefined spatial domain Ω_{opt}, the optimal material distribution with respect to a design goal [31]. This is done by varying a given material's distribution inside the domain. Two possible approaches are the density method used within this thesis and the homogenization method [32]. Another common approach within the general field of shape optimization [33] is geometry parameterization. There, an initial layout is chosen and parameterized with a given number of parameters. The parameter space is then investigated with respect to the design goal until an optimal geometry is found. Depending on the number of parameters this can be very time-consuming and the quality of the found solutions depends on the choice of parameters. In contrast, topology optimization does not require an initial layout. Furthermore, the solutions obtained using topology optimization are not restricted by any parameters except the parameters defining the optimization domain Ω_{opt}. However, topology optimization drastically increases the dofs. Examples of successful applications of topology optimization are the optimization of magnetic recording write heads [34], rotors of brushless DC motors [35], and electromagnetic actuators [36, 37].

4.1. The density approach for topology optimization

In order to perform topology optimization, here the density approach for topology optimization [38] (also referred to as solid isotropic micro-structure with penalization - SIMP [31]) is used. A scalar indicator function

$$\rho(\boldsymbol{r}) \in [0,1], \quad \text{where} \quad \rho(\boldsymbol{r}) = \begin{cases} 0\text{: no material} \\ 1\text{: material} \end{cases} \tag{4.1}$$

is introduced as design variable p. The respective functions representing the material are transformed by multiplication with the scalar indicator function (see section 4.2) in order to perform the optimization.

Additionally, the scalar indicator function is exponentiated with a parameter p. This is originally done in order to penalize intermediate values of $0 \leq \rho \leq 1$ that are allowed during optimization. However, the impact of this exponentiation is much bigger, as will be seen below. A detailed study of the impact of this parameter is given for each presented example. Furthermore, the impact of different initial distributions of ρ is investigated. Note that, this approach allows values of ρ unequal 0/1. However, in most cases, the magnetic density ρ should only take the values 0 or 1 since intermediate values $\rho \in (0,1)$ are very difficult to realize in fabrication. Therefore, some kind of regularization is necessary to prevent intermediate values of ρ. A possibility is Tikhonov regularization as also used in chapter 5. However, this approach is very time-consuming since the minimization problem has to be solved several times in order to adapt the regularization parameter. Therefore, here a brute force approach to regularization is used where after the optimization terminates all dofs with values of ρ with $0 \leq \rho < 0.5$ are set to 0 and all with $0.5 \leq \rho < 1$ are set to 1. This is justified since all solutions have final values of ρ very close to the bound as will be shown.

4.2. Topology optimization of magnetic structures - the adjoint of the full Maxwell problem

The topology of a magnetic structure containing soft, as well as hard magnetic materials, can be done by using the full Maxwell problem as defined by equations (3.9) and (3.10), that define the remanence magnetization $\boldsymbol{M}_\mathrm{r}$ and the susceptibility χ as material parameters. Using the density approach for topology optimization,, as introduced above, the material parameters are transformed giving $\boldsymbol{M}_\mathrm{r} \to \boldsymbol{M}_\mathrm{r}(\rho) = \rho^p \boldsymbol{M}_\mathrm{r}$ and $\chi \to \chi(\rho) = \rho^p \chi$.

The forward problem then reads

$$F(u(\rho), \rho) = \boldsymbol{\nabla} \cdot \left[(1 + \rho^p \chi) (\boldsymbol{\nabla} u - \boldsymbol{H}_\mathrm{ext}) - \rho^p \boldsymbol{M}_\mathrm{r} \right] = 0, \tag{4.2}$$

with unchanged open boundary condition. Note that here u is a scalar function from a Hilbert Space U satisfying the boundary condition that now takes the role of the state variable x defined in section 2.1. Furthermore, ρ is also a scalar function of an appropriate Hilbert space R replacing p as the control variable and F is now a mapping $U \times R \to Z$ into another appropriate Hilbert space Z. Also, the L^2-inner product is defined on all mentioned Hilbert spaces.

The reduced optimization problem can be written as

$$\min_{\rho \in R} \hat{J}\left(u\left(\rho\right), \rho\right) \tag{4.3}$$

for a given reduced objective functional $\hat{J}$ (compare section 2.1).

4.2.1. Adjoint equation

In order to efficiently minimize the reduced objective functional $\hat{J}\left(u\left(\rho\right), \rho\right)$ containing the design goal, its gradient with respect to the design variable ρ, $\nabla \hat{J}_\rho$ is needed.

As laid out in section 2.3, to obtain the gradient, first the adjoint equation and hence ∂F_u has to be derived. This is done using the definition of the Fréchet derivative (Definition 2) for a $w \in U$ as

$$\partial F_u\left(u\left(\rho\right), \rho; w\right) = \partial F_u w = \lim_{\epsilon \to 0^+} \frac{F\left(u + \epsilon w, \rho\right) - F\left(u, \rho\right)}{\epsilon} = \boldsymbol{\nabla} \cdot \Big(\left(1 + \rho^p \chi\right) \boldsymbol{\nabla} w \Big). \tag{4.4}$$

However, what is actually needed is the dual operator ∂F_u^* that can be obtained from Definition 4 with $\lambda \in Z$ being the adjoint variable

$$\begin{aligned} \left(\partial F_u w, \lambda\right) &= \int_{\mathbb{R}^3} \boldsymbol{\nabla} \cdot \Big(\left(1 + \rho^p \chi\right) \boldsymbol{\nabla} w \Big) \, \lambda \, \mathrm{d}V \\ = -\int_{\mathbb{R}^3} \left(1 + \rho^p \chi\right) \boldsymbol{\nabla} w \cdot \boldsymbol{\nabla} \lambda \, \mathrm{d}V &= \int_{\mathbb{R}^3} w \, \boldsymbol{\nabla} \cdot \Big(\left(1 + \rho^p \chi\right) \boldsymbol{\nabla} \lambda \Big) \, \mathrm{d}V \\ = \int_{\mathbb{R}^3} w \, \boldsymbol{\nabla} \cdot \Big(\left(1 + \rho^p \chi\right) \boldsymbol{\nabla} \lambda \Big) \, \mathrm{d}V &= \left(w, \partial F_u^* \lambda\right), \end{aligned} \tag{4.5}$$

where partial integration has been applied twice. The first boundary integral in row three vanishes if the validity of the equation is restricted to elements of $w \in U$ that also satisfy the boundary condition demanded from u. Furthermore, in order for the second boundary integral to vanish the same boundary condition has to be enforced on $\lambda \in Z$.

The adjoint equation therefore becomes (compare with equation (2.21))

$$\boldsymbol{\nabla} \cdot \Big(\left(1 + \rho^p \chi\right) \boldsymbol{\nabla} \lambda \Big) = \mathcal{R}\left(\partial J_u\right) \tag{4.6}$$

with boundary condition

$$\lambda\left(\boldsymbol{r}\right) \to \mathcal{O}\left(\frac{1}{|\boldsymbol{r}|}\right) \quad \text{for} \quad |\boldsymbol{r}| \to \infty. \tag{4.7}$$

The weak form of equation (4.6) is obtained by multiplication with a test function $v \in Z$

$$\int_{\mathbb{R}^3} \boldsymbol{\nabla} \cdot \Big(\left(1 + \rho^p \chi\right) \boldsymbol{\nabla} \lambda \Big) v \, \mathrm{d}V = \int_{\mathbb{R}^3} \mathcal{R}\left(\partial J_u\right) v \, \mathrm{d}V = \Big(\mathcal{R}\left(\partial J_u\right), v \Big). \tag{4.8}$$

On the right hand side of equation (4.8) the partial derivative of the objective functional with respect to the scalar potential u appears. However, generally optimality conditions will not be imposed on the potential but on the magnetic stray field $\boldsymbol{H}_\mathrm{d}$. Therefore, simplifying $\boldsymbol{H}_\mathrm{d} = \boldsymbol{H}$ from here on, this term is rewritten as

$$\Big(\mathcal{R}\left(\partial J_u\right), v \Big) = \partial J_u v = \partial J_{\boldsymbol{H}} \mathrm{d}\boldsymbol{H}_u v = \Big(\mathcal{R}\left(\partial J_{\boldsymbol{H}}\right), \mathrm{d}\boldsymbol{H}_u v \Big). \tag{4.9}$$

Considering $\boldsymbol{H}(u(\rho)) = -\boldsymbol{\nabla} u(\rho)$ and using the definition of the Fréchet derivative one can continue

$$\left(\mathcal{R}(\partial J_{\boldsymbol{H}}), \mathrm{d}\boldsymbol{H}_u v\right) = -\int_{\mathbb{R}^3} \mathcal{R}(\partial J_{\boldsymbol{H}})\, \boldsymbol{\nabla} v \,\mathrm{d}V \tag{4.10}$$

and therefore rewrite equation (4.8) as

$$\int_{\mathbb{R}^3} \boldsymbol{\nabla} \cdot \Big((1+\rho^p \chi)\, \boldsymbol{\nabla}\lambda \Big) v \,\mathrm{d}V = -\int_{\mathbb{R}^3} \mathcal{R}(\partial J_{\boldsymbol{H}})\, \boldsymbol{\nabla} v \,\mathrm{d}V. \tag{4.11}$$

After partial integration of the left hand side where the boundary term vanishes due to the boundary condition on λ this becomes:

$$-\int_{\mathbb{R}^3} (1+\rho^p \chi)\, \boldsymbol{\nabla}\lambda \cdot \boldsymbol{\nabla} v \,\mathrm{d}V = -\int_{\mathbb{R}^3} \mathcal{R}(\partial J_{\boldsymbol{H}})\, \boldsymbol{\nabla} v \,\mathrm{d}V. \tag{4.12}$$

Since the objective functional J is defined locally on a region Ω_{opt} this is the weak form of

$$\boldsymbol{\nabla} \cdot \Big((1+\rho^p \chi)\, \boldsymbol{\nabla}\lambda - \mathcal{R}(\partial J_{\boldsymbol{H}}) \Big) = 0, \tag{4.13}$$

an equation similar to the forward problem in equation (4.2) where, u is replaced by λ, $\boldsymbol{H}_{\text{ext}} = 0$ and $\rho^p \boldsymbol{M}_{\text{r}}$ is replaced by $\mathcal{R}(\partial J_{\boldsymbol{H}})$. Therefore, the same algorithm to solve the forward problem can also be used to solve the adjoint equation, simplifying the optimization problem. Note, that the same jump conditions are assumed for λ as done for u in the forward problem. This is possible, since the jump conditions are contained in the respective weak forms as shown in [39].

4.2.2. Gradient

Furthermore, to obtain the gradient $\nabla \hat{J}_\rho$, the operator ∂F_ρ^* is needed. In the same way as above, first ∂F_ρ is obtained using the definition of the Fréchet derivative with $r \in R$

$$\begin{aligned} \partial F_\rho(u(\rho), \rho; r) = \partial F_\rho\, r = \lim_{\epsilon \to 0^+} \frac{F(u(\rho), \rho + \epsilon r) - F(u(\rho), \rho)}{\epsilon} = \\ \boldsymbol{\nabla} \cdot \Big(p\rho^{p-1} r \left[\chi (\boldsymbol{\nabla} u - \boldsymbol{H}_{\text{ext}}) - \boldsymbol{M}_{\text{r}} \right] \Big) \end{aligned} \tag{4.14}$$

and again the dual operator ∂F_ρ^* is calculated using Definition 4

$$\begin{aligned} (\partial F_\rho\, r, \lambda) = \int_{\mathbb{R}^3} \boldsymbol{\nabla} \cdot \Big(p\rho^{p-1} r \left[\chi (\boldsymbol{\nabla} u - \boldsymbol{H}_{\text{ext}}) - \boldsymbol{M}_{\text{r}} \right] \Big) \lambda \,\mathrm{d}V = \\ -\int_{\mathbb{R}^3} \Big(p\rho^{p-1} r \left[\chi (\boldsymbol{\nabla} u - \boldsymbol{H}_{\text{ext}}) - \boldsymbol{M}_{\text{r}} \right] \Big) \cdot \boldsymbol{\nabla}\lambda \,\mathrm{d}V = \\ -\int_{\mathbb{R}^3} r \Big(p\rho^{p-1} \left[\chi (\boldsymbol{\nabla} u - \boldsymbol{H}_{\text{ext}}) - \boldsymbol{M}_{\text{r}} \right] \Big) \cdot \boldsymbol{\nabla}\lambda \,\mathrm{d}V = \left(r, \partial F_\rho^* \lambda \right). \end{aligned} \tag{4.15}$$

Here the boundary integral again vanishes since λ satisfies the boundary condition given by equation (4.7), which is only logical since ∂F_ρ^* will be applied to λ that also satisfies this boundary condition.

Finally, one can write the gradient as

$$\begin{aligned} \nabla \hat{J}_\rho = -\partial F_\rho^* \lambda + \mathcal{R}(\partial J_\rho) = \\ p\rho^{p-1} \left[\chi (\boldsymbol{\nabla} u - \boldsymbol{H}_{\text{ext}}) - \boldsymbol{M}_{\text{r}} \right] \cdot \boldsymbol{\nabla}\lambda + \mathcal{R}(\partial J_\rho) \in R. \end{aligned} \tag{4.16}$$

4.2.3. Optimization of a hard magnetic thin film flux guide concentrator

As a first example, the topology of a hard magnetic thin film flux guide concentrator is optimized to produce a maximal vertical (y-)component of the magnetic field H_y within the region Ω_h. The thickness of the thin film (z-direction) is 12.5 µm. The domain Ω_h, consisting of 91 cells (48 nodes), is situated 10 µm above an optimization domain Ω_opt consisting of 16505 cells (5717 nodes) (see Figure 4.1). The objective functional for this case is defined by

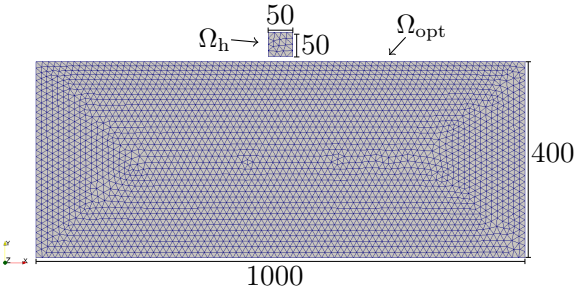

Figure 4.1.: Geometry and mesh of the thin film flux guide concentrator. Dimensions are given in µm. Picture taken from [22].

$$\hat{J}(\rho) = -\int_{\Omega_\mathrm{h}} H_y^2(\rho)\,\mathrm{d}V, \tag{4.17}$$

where H_y is the y-component of the magnetic stray field $\boldsymbol{H}$.

The optimization is performed using the B/H curve of the material linearized at the working point

$$B(H) = \mu_0\big((1+\chi)H + M_\mathrm{r}\big), \tag{4.18}$$

where the remanence magnetization is set to be $M_\mathrm{r} = 280000$ A/m and the anisotropy axis is chosen as the y-axis. First the case of an ideal permanent magnetic material with a susceptibility of $\chi = 0$ is considered. This case can be compared to an analytical model. After that, the same optimization problem is solved again using a realistic susceptibility of $\chi = 0.2$ and the results are compared.

Note that, as is true for all examples presented within this chapter, for the potential u and the adjoint variable λ piecewise linear basis functions ($\mathcal{P}_1$) are used, while the scalar indicator function ρ as well as χ, $\boldsymbol{M}_\mathrm{r}$, $\boldsymbol{H}_\mathrm{ext}$ and the derived stray field $-\boldsymbol{\nabla}u$ and $\boldsymbol{\nabla}\lambda$ are chosen to be constant within each element.

Ideal permanent magnet $\chi = 0$

In the same way as presented in [40] for a three dimensional permanent magnet and a point like target domain, an analytical solution for the optimal topology can be derived by considering the magnetization inside Ω_opt as being comprised of single dipoles $\boldsymbol{\mu}$. The magnetic flux density created by a dipole at distance $\boldsymbol{r}$ is given by

$$\boldsymbol{B}(\boldsymbol{r}) = \frac{\mu_0}{4\pi r^2}\frac{3\boldsymbol{r}(\boldsymbol{\mu}\cdot\boldsymbol{r}) - \boldsymbol{\mu}r^2}{r^3}. \tag{4.19}$$

Since the magnetic flux in y-direction is to be maximized, the relevant y-component of the magnetic flux density given by

$$B_y(\boldsymbol{r}) = \frac{\mu_0\mu_\mathrm{r}}{4\pi r^2}\left(\frac{3y^2 - r^2}{r^3}\right) \tag{4.20}$$

has to be considered, where y is the distance from the dipole in y-direction and r is the absolute distance from the dipole.

In the presented example, the size of the domain Ω_h within which the field is maximized is of considerable size. However, it has been validated that the assumption of a point like target domain is still valid, since the changes due to the finite size of Ω_h are too small to be resolved by the chosen mesh. For the quasi two dimensional thin film flux guide concentrator ($z = 0$) a positive contribution for B_y inside Ω_h is obtained for

$$x < \sqrt{2}y \tag{4.21}$$

and the surface condition $x = \sqrt{2}y$ defines the optimal topology as a cone with an opening angle of $\alpha \approx 35.26°$. In Figure 4.2 the analytical solution is shown and compared to the best numerical solution.

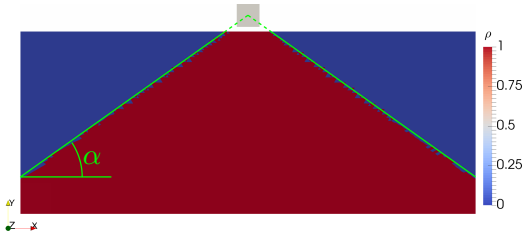

Figure 4.2.: Optimized topology for the ideal permanent magnet obtained with the objective functional defined in equation (4.17) and comparison with the analytical solution (green line).

The numerical optimization was performed for three different initial distributions of the indicator function ρ, two homogeneous distributions with a values of 1 and 0.5 respectively and a randomly initialized distribution with $\rho \in [0., 1.)$ (see Figure 4.3).

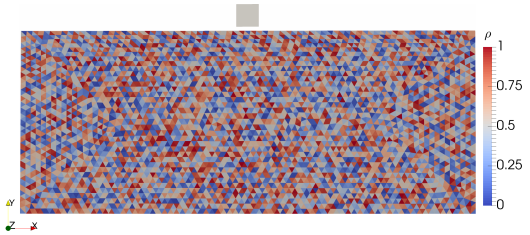

Figure 4.3.: Random initialization of the indicator function ρ.

As optimization algorithm, the Scipy implementation of the limited-memory Broyden–Fletcher-Goldfarb–Shanno minimization algorithm with bounds (L-BFGS-B) [41] is used. Note, that this algorithm, as well as other common ready-to-use optimization algorithms, are implemented to use the euclidean (ℓ^2) inner product internally to perform the optimization (i.e. e.g. approximate the Hessian) and only receive coefficient vectors as input. This has implications on mesh dependence and convergence rates as mentioned above (section 2.2) and discussed in detail in [21]. To prevent this e.g. the python package Moola [42] could be used. There, internally the correct inner product is used. However, Moola does not offer the possibility to put bounds on the optimization variable as necessary for the indicator function ρ when performing topology optimization. Note though, that the individual cells of the used mesh are of almost equal size. Since for functions constant within each element, the mass matrix is a diagonal matrix with the squared cell volumes as values, this makes the mass matrix a diagonal matrix with only values very close to each other. Now since the difference between the derivative and the gradient is given by multiplication with the mass matrix (see section A.2 in the appendix), in this case, this reduces to a simple scaling.

Using the derivative $\mathrm{d}\hat{J}(\rho)$ As mentioned before, the derivative $\mathrm{d}\hat{J}(\rho)$ can be obtained from the gradient $\nabla\hat{J}(\rho)$ (as given by equation (4.16)) by multiplication with the mass matrix. In order to illustrate the differences of using the derivative and the gradient as updates during optimization, as discussed in section 2.2, first the optimization using the derivative is presented.

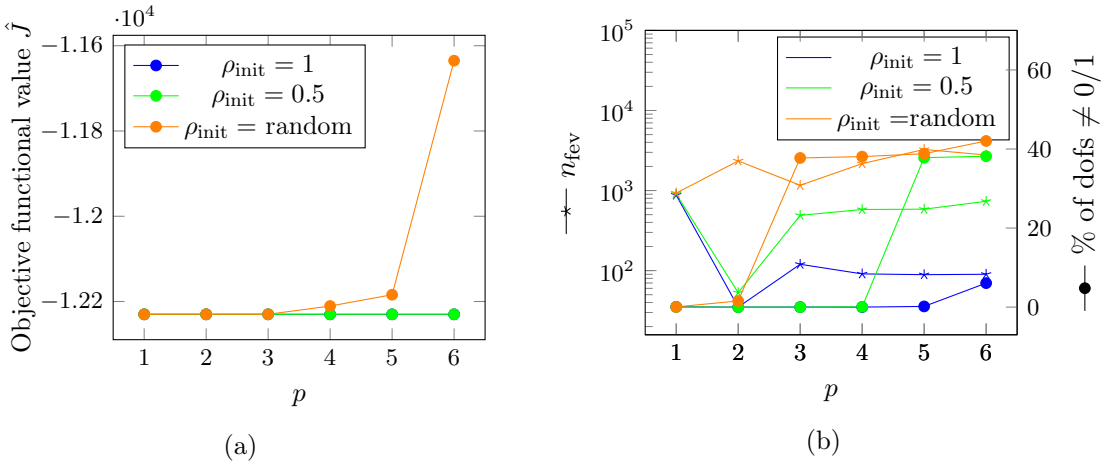

Figure 4.4.: Dependence of (a) the objective functional value $\hat{J}$ and (b) the number of necessary function evaluations n_{fev} and the number of dofs with intermediate values of ρ on the penalty parameter p when using the derivative $\mathrm{d}\hat{J}(\rho)$.

In Figure 4.4 the dependence of the objective functional value $\hat{J}$, the number of necessary function evaluations n_{fev} and the percentage of dofs with intermediate values of ρ on the penalty parameter p is shown up to $p = 6$ for the different initial distributions of ρ. The best value of the objective functional of $\hat{J} = -12230.06$ is found by the optimizations using a homogeneous initial distribution up to a value of the penalty parameter of $p = 6$. The corresponding topology can be seen in Figure 4.2 where it is compared to the analytically obtained optimal topology. Note that this objective functional value corresponds to a mean field inside Ω_{h}, $\mu_0 \bar{H}_y = \int_{\Omega_{\text{h}}} \mu_0 H_y \, \mathrm{d}V / V_{\Omega_{\text{h}}}$ of 22.81 mT. For the randomly initialized material distribution the solution gets worse for $p > 3$. Regarding the number of necessary function evaluations a minimum of $n_{\text{fev}} = 35$ is found for $\rho_{\text{init}} = 1$ with $p = 2$. Note, that even though the number of dofs with intermediate values of ρ rises also for the homogeneously initialized material distributions with increasing p, the objective functional value stays at its minimum. This suggests, that the dofs' deviation from 0 or 1 respectively is very small. Applying simple brute force regularization, i.e. setting all dofs with $\rho < 0.5$ to 0 and all dofs with $\rho \geq 0.5$ to 1 removes all intermediate values. For the presented optimizations this however, does not improve the objective functional value also for the randomly initialized optimization.

The objective functional as defined above (equation (4.17)) includes an integral over the domain Ω_{h} and therefore depends on the volume. This leads to mesh dependence even though the magnetostatic forward problem is scale independent. The mesh size dependence can be eliminated by dividing the objective functional by the Volume $V(\Omega_{\text{h}})$. Performing the optimization with the new objective functional, for $\rho_{\text{init}} = 1$ the same optimal solution is then found within 5 function evaluations without intermediate values of ρ. The reason for the lower number of necessary function evaluations is found in the fact, that by division with the volume $V(\Omega_{\text{h}})$ the objective functional and with it also the derivative were scaled up. Since bounds are enforced on ρ and therefore the size of the derivative determines how fast the individual dofs are set to 0 or 1 this explains the lower number of necessary function evaluations. In fact, since the same solution is found using a larger derivative, this also shows that the optimization problem for zero susceptibility is linear in ρ^p, as expected since the only source term in the forward problem (4.2) is given by $\rho^p \boldsymbol{M}_{\text{r}}$ where $\boldsymbol{M}_{\text{r}}$ is constant.

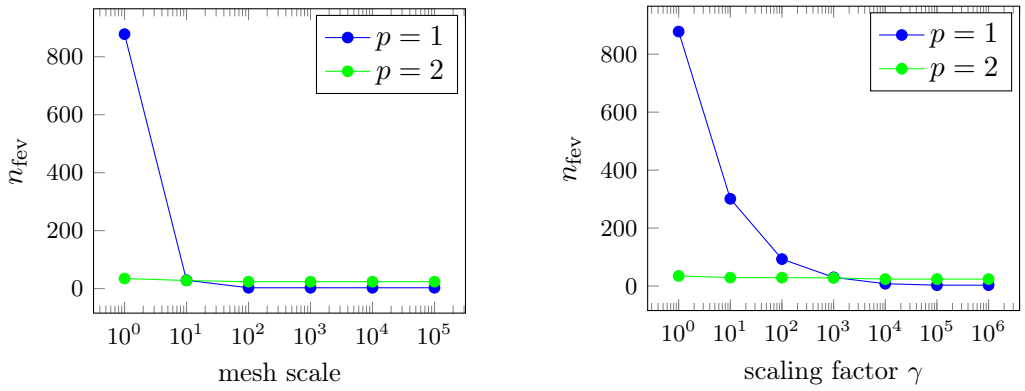

Figure 4.5.: Dependence of the number of necessary function evaluations n_{fev} on (a) the mesh scale and (b) the scale γ when using the derivative $\mathrm{d}\hat{J}(\rho)$.

The dependence on the derivative's size can also be seen in Figure 4.5a where the number of necessary function evaluations, using the original, volume dependent objective functional (equation (4.17)) is shown in dependence of the mesh scale. Note that by increasing the mesh scale, the volume $V(\Omega_{\text{h}})$ and therefore the objectice functional value and the size of the derivative increases. For $p = 1$ as well as for $p = 2$ the optimal solution without intermediate values of ρ is found for a minimum of 3 and 24 function evaluations respectively for a mesh scale >= 100, while for default mesh 878 and 35 function evaluations are necessary. That this is indeed due to the derivatives size can be seen by scaling the derivative for a fixed mesh scale. In Figure 4.5b the number of necessary function evaluations n_{fev} is plotted in dependence of the scaling factor γ. The minimal number of necessary function evaluations of 3 and 24 respectively is found for $\gamma \geq 10^4$. Note, that using an initial distribution of $\rho_{\text{init}} = 0.5$ the minimal number of $n_{\text{fev}} = 3$ is also valid for $p > 1$. Furthermore, note that scaling the derivative independently of the objective functional leads to problems during the optimization. In detail, the L-BFGS-B algorithm terminates reporting problems during the line search when the scale of the objective functional is much smaller than the scale of the derivative. The algorithm then simply returns the initial distribution of ρ. This is since one of the Wolfe conditions, the Armijo rule, that has to be meet in order for the line search to end is never satisfied. This can be circumvented by also scaling the objective functional value. Since the L-BFGS-B algorithm uses the objective function value only during the line search while performing a quasi-Newton method, this scaling of the objective functional does not alter the results.

When using meshes with differently sized element, using the derivative $\mathrm{d}\hat{J}$ can lead to additional problems for the optimization, since each dof is scaled by the size of its mesh element. A detailed discussion of this mesh dependence can be found in [21] and the implications are further presented in subsection 4.2.5 were an example using a differently refined mesh is presented. Here the problem is only illustrate in Figure 4.6 where a mesh of the thin film flux guide concentrator with a refined area, and the corresponding derivative and the gradient of the first iteration for an initial value of $\rho_{\text{init}} = 1$ is shown. It is clearly visible, that the derivative has larger values at larger elements (see Figure 4.6a), while this is not the case for the gradient (see Figure 4.6b).

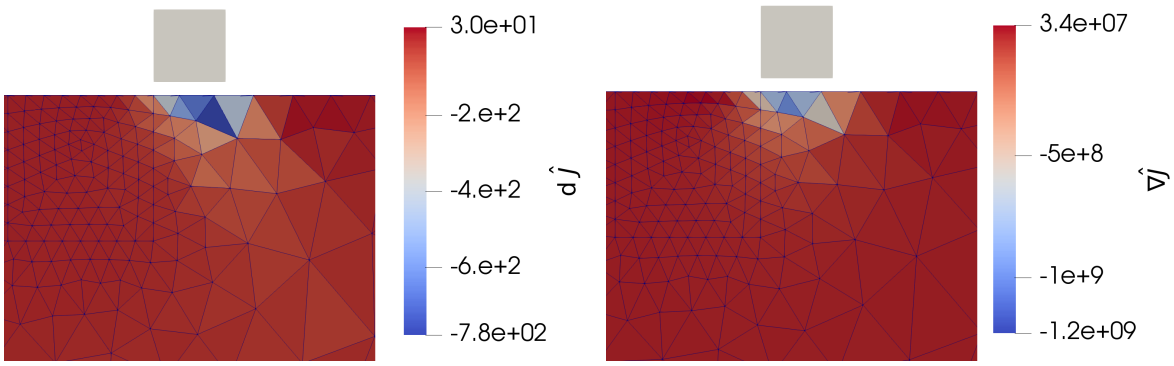

(a) (b)

Figure 4.6.: Magnification of the derivative $\mathrm{d}\hat{J}$ (a) and gradient $\nabla\hat{J}$ (b) of the first iteration for $\rho_{\text{init}} = 1$ and $p = 1$ using a partially refined mesh.

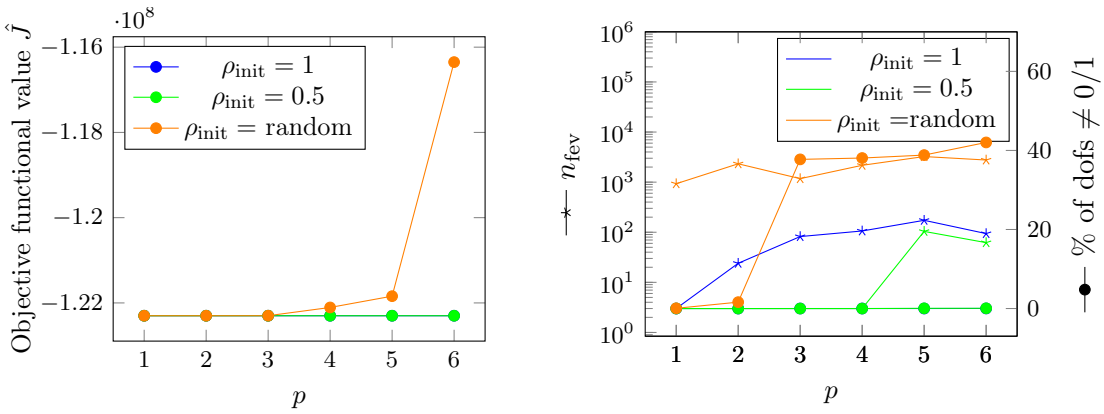

(a) (b)

Figure 4.7.: Dependence of (a) the objective functional value $\hat{J}$ and (b) the number of necessary function evaluations n_{fev} and the number of dofs with intermediate values on the penalty parameter p when using the gradient $\nabla\hat{J}\,(\rho)$.

Using the gradient $\nabla\hat{J}$ Using the gradient avoids the problems of mesh dependence discussed above. In detail, the gradient size becomes mesh independent since in the case of the L^2-inner product, the gradient is obtained from the derivative by multiplication with the inverse mass matrix. In comparison to the derivative, the dofs of the gradient are much larger than the dofs of the derivative (see also Figure 4.6a and 4.6b). However, when using a volume dependent objective functional, the fixed size of the gradient can lead to the same convergence problem of the L-BFGS-B algorithm discussed above and it can be necessary to scale the objective functional value during optimization. In order to perform the optimization using the L-BFGS-B algorithm, therefore the objective functional has to be scaled by 10^4. In Figure 4.7 the dependence of the objective functional value, the number of necessary function evaluations and the percentage of dofs with intermediate values of ρ on the penalty parameter p are shown up to $p = 6$ for the different initial distributions of ρ. For the homogeneous initial distributions the best solution is again found up to $p = 6$ while for the randomly initialized distribution the solution gets worse for $p > 3$. As expected, since the dofs of the gradient are large compared to the derivative, the number of necessary function evaluations is smaller. In detail for an initial distribution of $\rho_{\text{init}} = 0.5$ n_{fev}

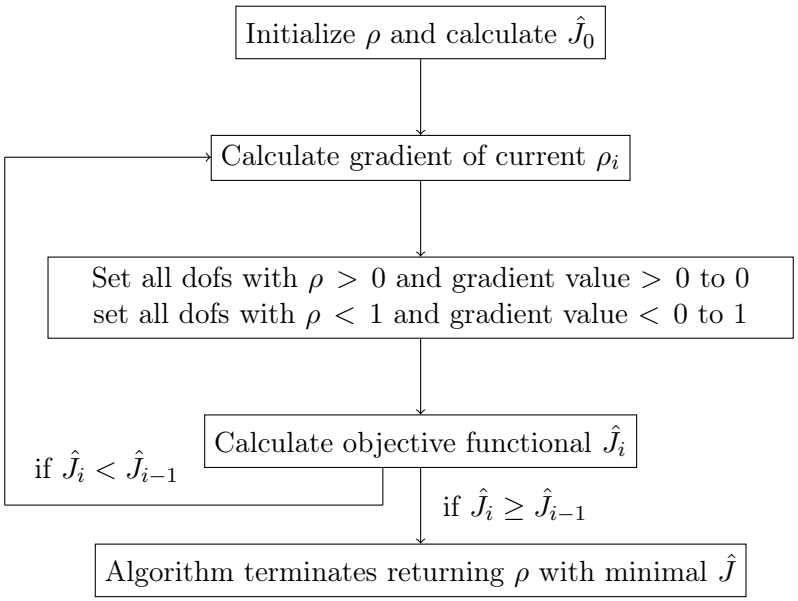

Figure 4.8.: Flowchart of the gradient size independent minimization algorithm.

is equal 3 for $p \geq 4$ while for $\rho_{\text{init}} = 1$ the minimum of 3 necessary function evaluations is only found at $p = 1$. The number of dofs with intermediate values of ρ is similar to the optimizations using the derivative and can also be removed by simple brute force regularization.

Gradient size independent optimization The dependence of the L-BFGS-B optimization algorithm on the relative scale between gradient and objective functional value suggests the usage of an optimization algorithm independent of the exact size of the gradient. Since the above examples show, that large gradients, i.e. setting all elements directly to 0 or 1 respectively, reduces the number of necessary function evaluations, an optimization algorithm setting the dofs of ρ to 0 or 1 directly only in dependence of the gradients sign is proposed. This method of optimization is also often referred to as on/off method or the algorithms are called binary [43, 44, 34, 30, 45]. An additional advantage of this method is that intermediate values of ρ are avoided and therefore no regularization is necessary. The algorithm is depicted in detail in Figure 4.8.

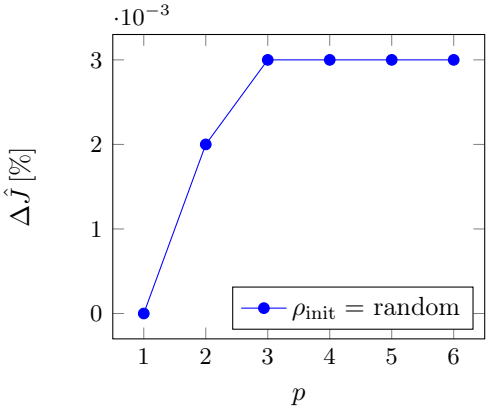

Figure 4.9.: Dependence of the deviation from the optimal solution $\Delta\hat{J}$ on the penalty parameter p for a randomly initialized ρ using the gradient size independent optimization algorithm.

For a homogeneous initial distribution of $\rho_{\text{init}} = 1$, as well as $\rho_{\text{init}} = 0.5$, all optimizations using the gradient size independent optimization algorithm up to $p = 6$ find the same optimal solution as before with 4 necessary function evaluations and without intermediate values of ρ. Note, the reason for the additional necessary function evaluation compared to the best optimization

using the L-BFGS-B algorithm is due to its usage of the gradient norm as termination condition. If a check for the gradient norm were implemented in the gradient size independent optimization algorithm, the number of necessary function evaluations would be reduced by one accordingly. Only when using a random initial configuration of ρ the optimal solution is not found for $p > 1$ as depicted in Figure 4.9. However, The number of necessary function evaluations is still 4 for all values of p and no intermediate values of ρ are present in the final topology. Note, the difference between the objective functional value of the optimal solution and the worst solution at $p = 4$ is negligible ($< 0.1‰$) and the found topologies differ by only 12 cells.

A different objective functional Another objective functional that can be used to maximize the field in the same way as above is

$$J = -\int_{\Omega_\mathrm{h}} H_y \,\mathrm{d}V. \tag{4.22}$$

This objective functional avoids the ambiguity in the field direction that is present in the previous objective functional (equation (4.17)) since now only positive values of H_y minimize the objective functional. Using the gradient size independent optimization algorithm this objective functional finds a solution that creates a higher mean field $\mu_0\bar{H}_y = \int_{\Omega_\mathrm{h}} \mu_0 H_y \,\mathrm{d}V/V_{\Omega_\mathrm{h}}$ of 22.83 mT as compared to the previous optimum with $\mu_0\bar{H}_y = 22.81$ mT. This constitutes an increase of 0.11%. The optimized topology can be seen in Figure 4.10 where it is also compared to the analytical solution. It differs from the optimal topology found with the previous objective functional (see Figure 4.2) by 196 dofs of ρ. The advantageousness of this objective functional can furthermore be seen since using it, also the randomly initialized topologies deliver the optimal solution at least for $p \leq 6$ and the number of necessary function evaluation drops to 3 for all initializations and $p \leq 6$. This objective functional is therefore used from here on.

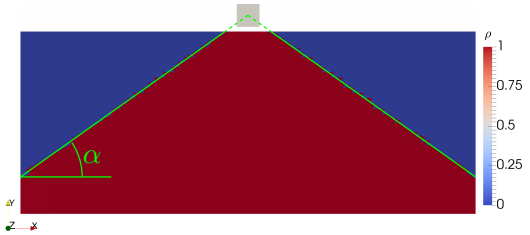

Figure 4.10.: Optimized topology for the ideal permanent magnet obtained with the objective functional defined in equation (4.22) and comparison with the analytical solution (green line).

Realistic permanent magnet $\chi = 0.2$

Using a realistic value for the susceptibility of $\chi = 0.2$ the best solution found creates a mean field of $\mu_0\bar{H}_y = 22.35$ mT. The reduction in mean field with respect to the ideal permanent magnet can be attributed to the appearing demagnetization effects. The optimal topology is shown in Figure 4.11, where it is also compared to the optimal topology obtained for $\chi = 0$. It differs only by slightly from ideal permanent magnet topology (109 different dofs).

Using the L-BFGS-B optimizer, the best solution is found independent of ρ_init for $p = 1$. Since for larger values of p the mean field produced by the found topologies decreases, the optimization is no longer independent of the parameter p. Note, however, that the difference in mean field is below 0.5% for $p \leq 4$.

As can be seen in Figure 4.12, scaling the gradient does not reduce the number of necessary function evaluations in the same way as for the ideal permanent magnet. This is due to the introduced non-linearity in ρ. While n_fev still decreases with increasing gradient size the minimal

number of necessary function evaluations is found for a constant initial distribution of $\rho_{\text{init}} = 1$ where for $\gamma > 10$ $n_{\text{fev}} < 250$. Furthermore, the optimized topologies again show dofs with intermediate values of ρ, although their number is negligible for all simulations with $p = 1$.

Using the gradient size independent optimization algorithm, the solutions are identical to the solution found using the L-BFGS-B optimization algorithm for $p = 1$ for all initializations. For larger p the solutions again get worse. However, the mean field $\bar{H}_y$ of the worst solution found for $p \leq 6$ differs by only $< 0.1‰$ from the best solution found. Regarding the number of necessary function evaluations, directly following the gradient leads to a severe reduction to $n_{\text{fev}} = 11$ for the homogeneous initializations of ρ and 14 for the random initialization for $p = 1$.

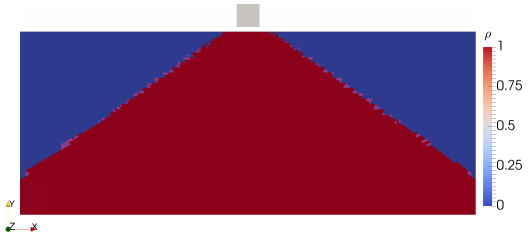

Figure 4.11.: Optimized topology for the realistic permanent magnet with $\chi = 0.2$ obtained with the objective functional defined in equation (4.22). The cells different with respect to the optimal topology obtained for $\chi = 0$ are colored in pink.

Note, that using the topology obtained for the optimization of the ideal permanent magnetic material, for a realistic hard magnetic material with $\chi = 0.2$ the produced mean field is only negligibly smaller ($< 0.1‰$) than the mean field produced by the best topology obtained by optimization with the realistic material. Therefore, and since the two topologies differ by only 109 dofs of ρ, $\chi = 0$ is a good assumption for a permanent magnetic structure.

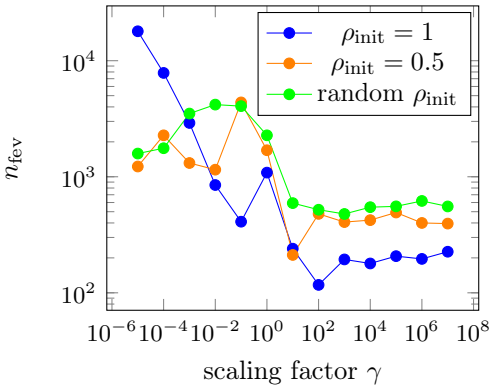

Figure 4.12.: Dependence of the number of necessary function evaluations n_{fev} on γ for the realistic hard magnetic material with $\chi = 0.2$ using the L-BFGS-B optimization algorithm with $p = 1$. Figure taken from [22].

Concluding the optimization using a hard magnetic material, it has been shown that for an ideal hard magnetic flux guide concentrator the presented algorithm delivers an optimized topology in accordance with the analytical model independent of the used minimization algorithm. Apparent gradient size (and with it mesh scale) dependencies present when using the L-BFGS-B minimization algorithm can be avoided using a gradient size independent minimization algorithm, while still finding the same optimal solution within a minimal amount of necessary function evaluations. Furthermore, this approach completely avoids solutions with intermediate values of ρ. Investigating the optimization process in detail, it has been found that the optimizations are independent of the initial distribution ρ_{init} of the indicator function ρ at least for values of the penalty parameter $p \leq 6$. Furthermore, regarding the optimization using a realistic permanent magnetic material, it can be concluded, that the approximation of using an ideal permanent magnetic material is valid, and only leads to negligible deviations.

4.2.4. Optimization of a soft magnetic thin film flux guide concentrator

As a next step, the topology of a soft magnetic thin film is optimized to act as a magnetic flux guide concentrator. A soft magnetic flux guide concentrator enhances the external field at a given position in space to e.g. improve the magnetic field detection limits of a spin valve sensor [46]. Here, the magnetic flux in vertical (y-)direction inside Ω_h is maximized. To do so, the same mesh as before (see Figure 4.1) is used and the objective functional is given by equation (4.22).

The optimization is again performed using a linear material law as defined by equation (4.18), where in the soft magnetic case the remanence magnetization vanishes. In the following, materials with three different susceptibilities of $\chi = 10^2$, 10^3 and 10^4 are considered, and again different initial material distributions are investigated. In all cases, an external field in y-direction of 10 mT is applied and the gradient $\nabla \hat{J}$ is used for the optimization.

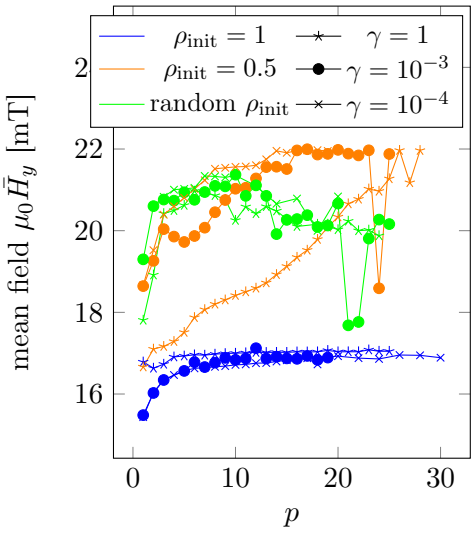

Figure 4.13.: Dependency on the penalty parameter p for different initial distributions ρ_init and gradient scaling factors γ for the optimization for $\chi = 10^3$. Figure taken from [22].

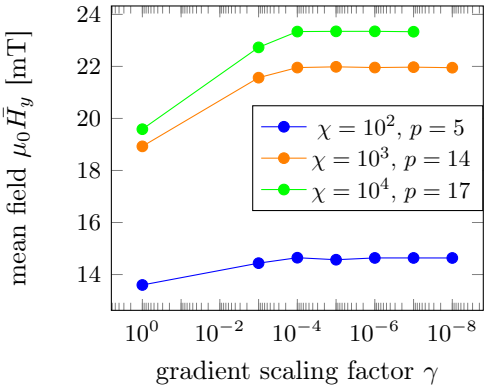

Figure 4.14.: γ-dependency of the mean field $\mu_0 \bar{H}_y$ for individual values of p. Figure taken from [22].

First, the L-BFGS-B minimization algorithm is again used to perform the topology optimization. Note, that in the same way as above scaling of the objective functional is necessary. In contrast to the topology optimization using hard magnetic material the optimizations using soft magnetic material depend much more on the penalty parameter p and the initial distribution ρ_init. This is shown in Figure 4.13 where the mean field $\bar{H}_y$ produced by the optimized and brute force regularized topologies with $\chi = 10^3$ is plotted in dependence of the penalization parameter p for different values of the gradient scaling factor γ. The best topologies are found for an initial distribution of $\rho_\mathrm{init} = 0.5$ while the best topologies optimized with $\rho_\mathrm{init} = 1$ are clearly inferior suggesting that the optimization works better when the optimizer has the possibility to also add material. The p-dependence shows an increase in mean field with increasing p up to a plateau value from where on the topologies do not further improve. This plateau value depends on the gradient scaling γ. With decreasing γ the plateau value decreases from $p = 26$ at $\gamma = 1$ until for $\gamma > 10^{-4}$ the plateau value is $p = 14$ and it does not change when further decreasing γ. Above the plateau value the mean field of the optimized topologies differs by under 1% with respect to the mean field obtained with the plateau value, except for individual outliers. This

γ-dependence is similar for single values of p for all different values of χ as shown in Figure 4.14 where with decreasing γ, $\bar{H}_y$ increases until the maximum is found again for $\gamma = 10^{-4}$.

The number of dofs with intermediate values of ρ in the optimized topology is plotted in Figure 4.15 in dependence of p for $\chi = 10^3$. With increasing p the percentage of dofs with $\rho \neq 0/1$ increases up to 60% for high values of p. A higher p therefore does not suppress intermediate values of ρ as initially intended, but the influence of p is much larger since the best topologies are found for higher values of p. Note, that the effects of the brute force regularization are under 1% for all optimizations showing, that the intermediate values of ρ are close to 0 and 1 respectively. This can also be seen in Figure 4.16 where the unregularized and regularized topologies are compared.

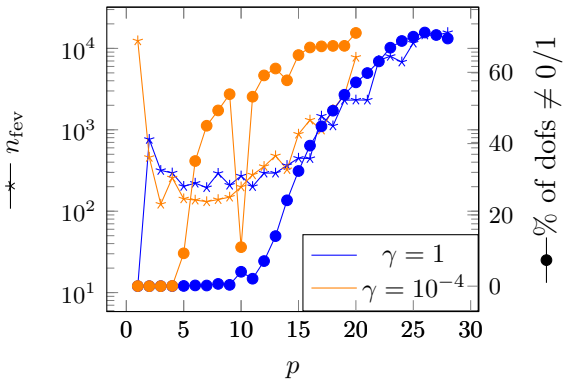

Figure 4.15.: Dependency of the number of necessary function evaluations n_{fev} and the percentage of dofs with intermediate values of ρ after optimization on the penalty parameter p for different values of γ for the optimization performed for $\chi = 10^3$. Figure taken from [22].

In Figure 4.15, also the number of necessary function evaluations n_{fev} is plotted in dependence of p for different values of the gradient scaling factor γ for $\chi = 10^3$. n_{fev} is lower for $\gamma = 10^{-4}$ where the best solution found for $p = 14$ within 325 function evaluations, than for $\gamma = 1$ where $n_{\text{fev}} = 14631$ for $p = 26$ where the best topology is found.

For $\chi = 10^2$ and $\chi = 10^4$ the dependences are similar. For both the mean field plateaus in dependence of p. Only the plateau values for $\gamma = 10^{-4}$ are different with $p = 5$ for $\chi = 10^2$ and $p = 17$ for $\chi = 10^4$. Note that for $\chi = 10^2$ the best topologies found for p larger than the plateau value get worse.

The best topologies for all χ-values can be seen in Figure 4.16 where also the results before regularization are shown. The optimized topologies have a characteristic "tanga" shape as also presented in [46] as optimal design. Note, that the best topologies for $\chi = 10^3$ and $\chi = 10^4$ differ only slightly while the topology for $\chi = 10^2$ is significantly broader. In Table 4.1 the mean field values produced by the best topologies are stated and their increase in mean field with respect to the full plate ($\rho = 1$ in Ω_{opt}) is stated.

χ	$\mu_0 \bar{H}_y$ [mT]	n_{fev}	increase [%]
10^2	14.65	281	52.25
10^3	21.95	325	84.38
10^4	23.34	493	91.23

Table 4.1.: Mean field values $\mu_0 \bar{H}_y$, number of necessary funcion evaluations n_{fev} and increase with respect to the full plate for the optimized topologies using the L-BFGS-B optimization algorithm.

In order to avoid the dependence on the gradient's size, the optimization can again be performed using the gradient size independent optimization algorithm introduced above. However, when using a soft magnetic material, the obtained topologies are inferior to the topologies obtained using the L-BFGS-B algorithm. This is, since in case of soft magnetic materials, the large value of the susceptibility χ introduces a higher dependence of the magnetization state on the

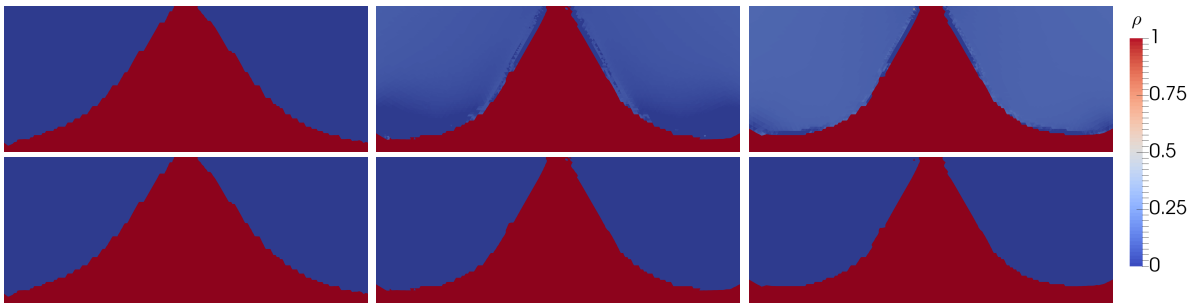

(a) (b) (c)

Figure 4.16.: Optimized topologies using the L-BFGS-B optimization algorithm with $\gamma = 10^{-4}$ for (a) $\chi = 10^2$ (for $p = 5$) (b) $\chi = 10^3$ (for $p = 14$) and (c) $\chi = 10^4$ (for $p = 17$), before (top row) and after regularization (bottom row). Figure taken from [22].

demagnetization field and therefore, the optimization problem is no longer linear in ρ^p. Note, that this non-linearity of the optimization exists even though a linear material law is used. In Figure 4.17 the topology obtained using the gradient size independent optimization algorithm for $\chi = 10^3$, $\rho_{\text{init}} = 0.5$ and $p = 1$ is shown. The differences to topologies obtained using the L-BFGS-B algorithm are clearly visible and the produced mean field is only 16.76 mT. Therefore, a different optimization algorithm is necessary.

Figure 4.17.: Optimized topology obtained using the gradient independent optimization algorithm for $\chi = 10^3$, $\rho_{\text{init}} = 0.5$ and $p = 1$.

Binary topology optimization

In order to enable the efficient optimization of also soft magnetic structures, the optimization algorithm following the gradient directly as presented in Figure 4.8 has to be modified. The modification is that not all dofs participate at once, but only a predefined number is changed during each iteration. The algorithm is called binary topology optimization (BTO) algorithm and is visualized in Figure 4.18. The fraction of dofs participating in each optimization step is determined by a parameter $\eta \in (0, 1]$. Given the number of degrees of freedom n_{dofs} in the optimization region Ω_{opt}, the actual number of participating dofs is obtained from $n_{\text{p}} = \eta \cdot n_{\text{dofs}}$. The optimization then starts with a given initial distribution ρ_{init} by first calculating the gradient. A new ρ_i is then obtained by setting the $n_{\text{p}}/2$ dofs for which the gradient is largest positive (removing material is most advantageous) and their value of ρ is unequal 0, to 0 and setting the $n_{\text{p}}/2$ dofs for which the gradient is larges negative (adding material is most advantageous) and their value of ρ is unequal 1, to 1. The objective functional is then evaluated for the new ρ_i. If the objective functional value decreases, the next iterations start by calculating the gradient for the new ρ_i and so forth. If the objective functional values stays unchanged, this means that no dofs of ρ have changed during the last iteration and the algorithm assumes a minimum is found and terminates. However, in case of an increase of the objective functional value, to prevent stalling in a local minimum, up to five additional iterations are performed. If within these additional iterations the objective functional values does not reduce further, the optimization terminates

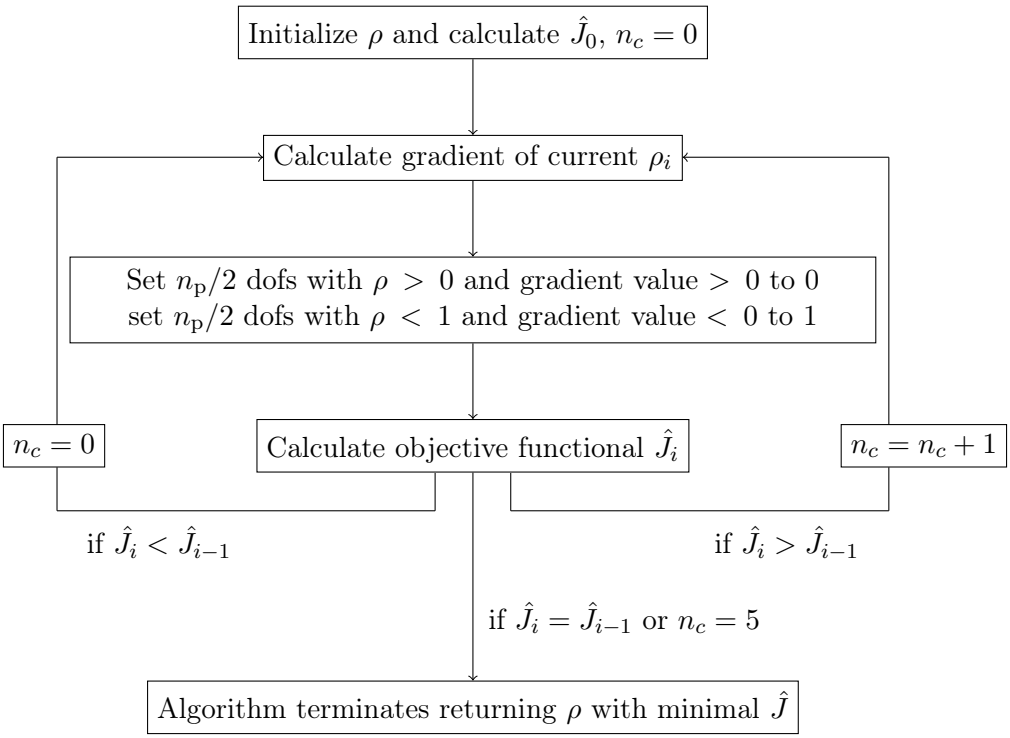

Figure 4.18.: Flowchart of the binary topology optimization (BTO) algorithm.

and the topology having the lowest objective functional value is returned. Note, that for the case of $\eta = 2$ this algorithm is identical to the gradient size independent minimization algorithm presented above.

In Figure 4.20 the mean field $\bar{H}_y$ and the number of necessary function evaluations n_fev of the optimized topologies for $\chi = 10^3$ for the three different initial distributions ρ_init obtained using the BTO algorithm is plotted in dependence of the penalty parameter p for different values of the participation η. All optimizations terminate without intermediate values of ρ as intended. The mean field again shows a strong dependence on the penalty parameter p. The highest mean field of 22.59 mT is obtained from the topologies optimized with $\rho_\mathrm{init} = 0.5$ with $p = 5$ and $\eta = 0.01$ within 133 function evaluations. Note that for $\rho_\mathrm{init} = 1$ the mean fields are much lower than for the other two initial distributions of ρ suggesting that the possibility to only subtract material during optimization is disadvantageous. The best topology is shown in Figure 4.19. The topology again shows the same "tanga" structure as the topologies obtained using the L-BFGS-B algorithm but with a much thinner peak. Furthermore, the optimization produces detached material island around the main topology. These material islands increase in number with decreasing participation η and are therefore assumed to be due to numerical inaccuracies during gradient calculation.

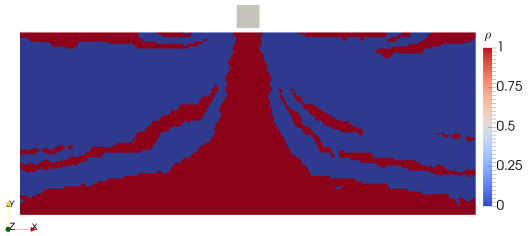

Figure 4.19.: Best optimized topology obtained using the BTO algorithm for $\chi = 10^3$, $\rho_\mathrm{init} = 0.5$, $p = 5$ and $\eta = 0.01$.

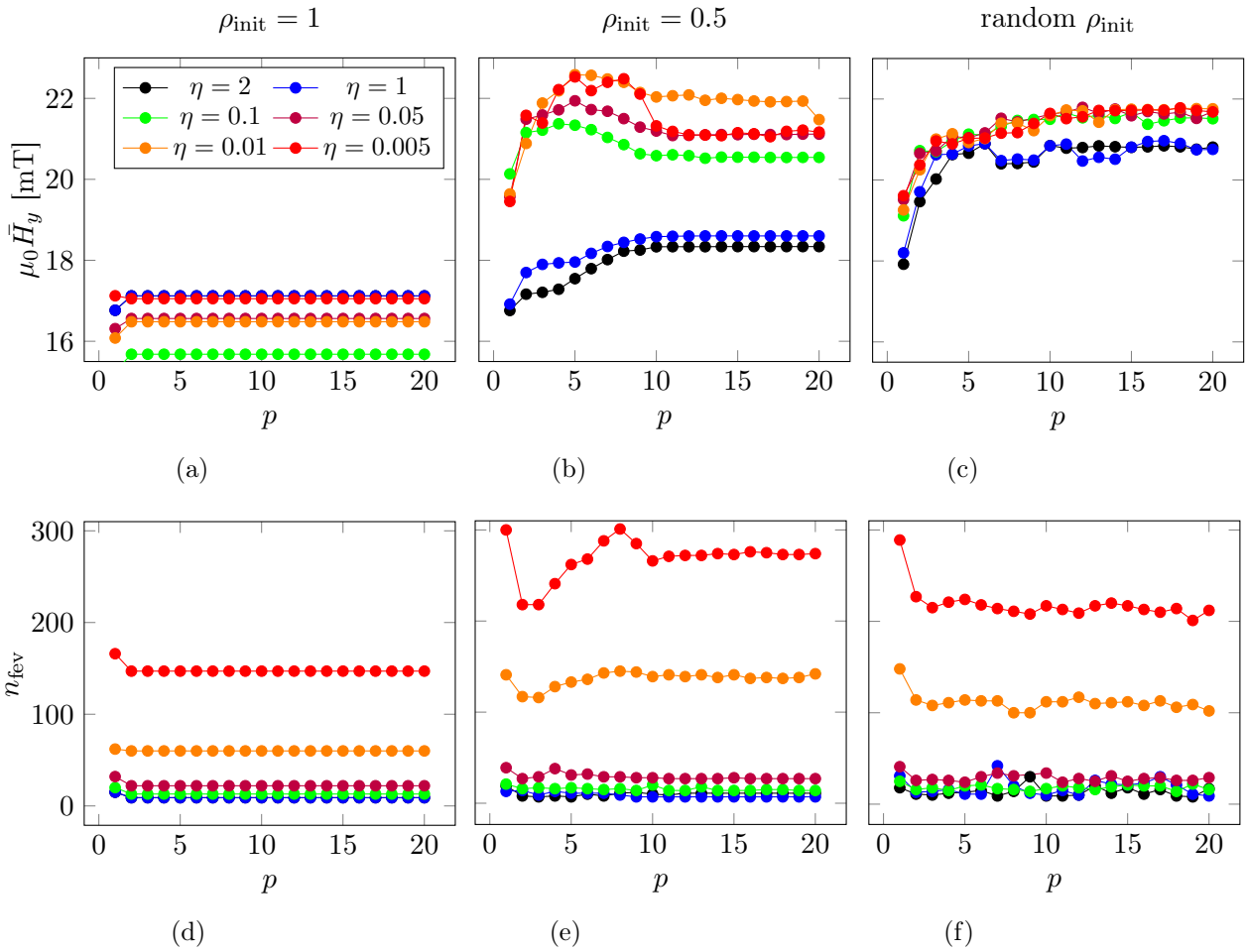

Figure 4.20.: Dependence on the penalty parameter p of the mean field $\mu_0 \bar{H}_y$ ((a) - (c)) and the number of necessary function evaluations n_{fev} ((d) - (f)) for the optimization with $\chi = 10^3$ using the BTO algorithm with an initial distribution of $\rho_{\text{init}} = 1$ ((a) and (d)), $\rho_{\text{init}} = 0.5$ ((b) and (e)) and a random initialization of ρ ((c) and (f)).

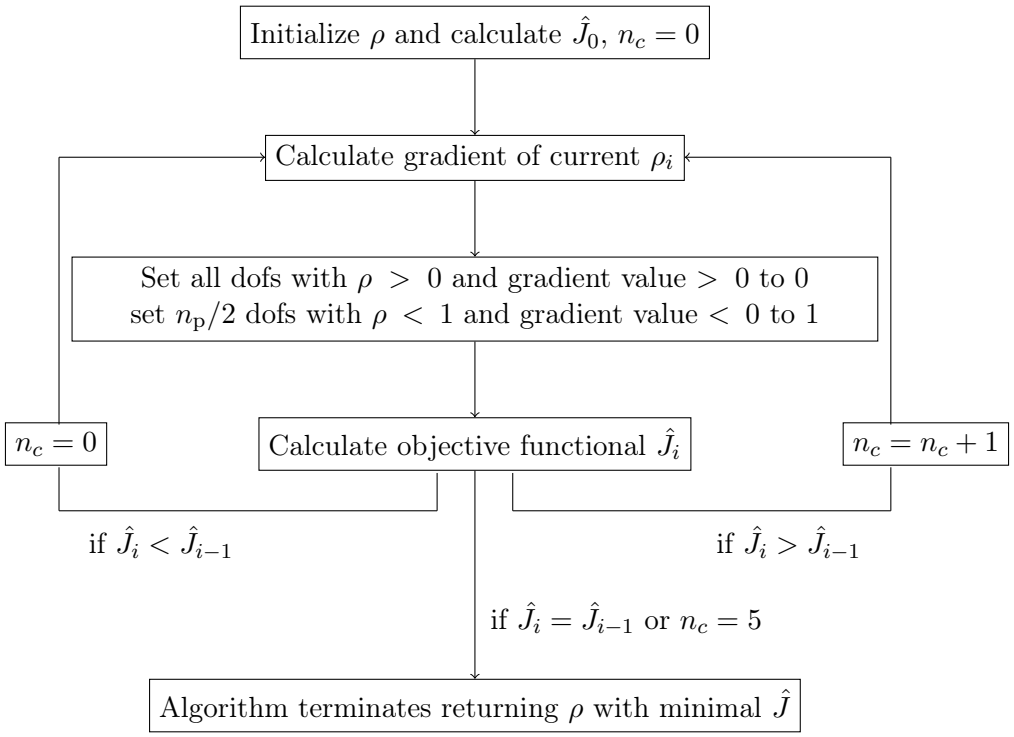

Figure 4.21.: Flowchart of the regularizing binary topology optimization (RBTO) algorithm.

In order to avoid the material islands appearing using the BTO algorithm, the algorithm can be modified by setting all dofs where taking material away is beneficial to 0 immediately. The modified algorithm is depicted in Figure 4.21 and is called regularizing binary topology optimization (RBTO) algorithm. The mean field $\bar{H}_y$ and the number of necessary function evaluations n_fev of the optimized topologies for $\chi = 10^3$ for the three different initial distributions ρ_init obtained using the RBTO algorithm is plotted in dependence of the penalty parameter p for different values of the participation η in Figure 4.23. The dependencies are similar compared to the results obtained using the BTO algorithm. Only for $\rho_\mathrm{init} = 1$ the dependency on the participation η vanished completely, since all material is now taken away in the first iteration. The highest mean field is again obtained for $p = 5$ and $\eta = 0.01$ within 51 function evaluations and is with 22.54 mT 0.22 % lower than the maximum obtained using the BTO algorithm. The best topology is shown in Figure 4.22. The detached material island that appeared using BTO vanished but the topology shows holes at the bottom.

Figure 4.22.: Best optimized topology obtained using the RBTO algorithm for $\chi = 10^3$, $\rho_\mathrm{init} = 0.5$, $p = 5$ and $\eta = 0.01$.

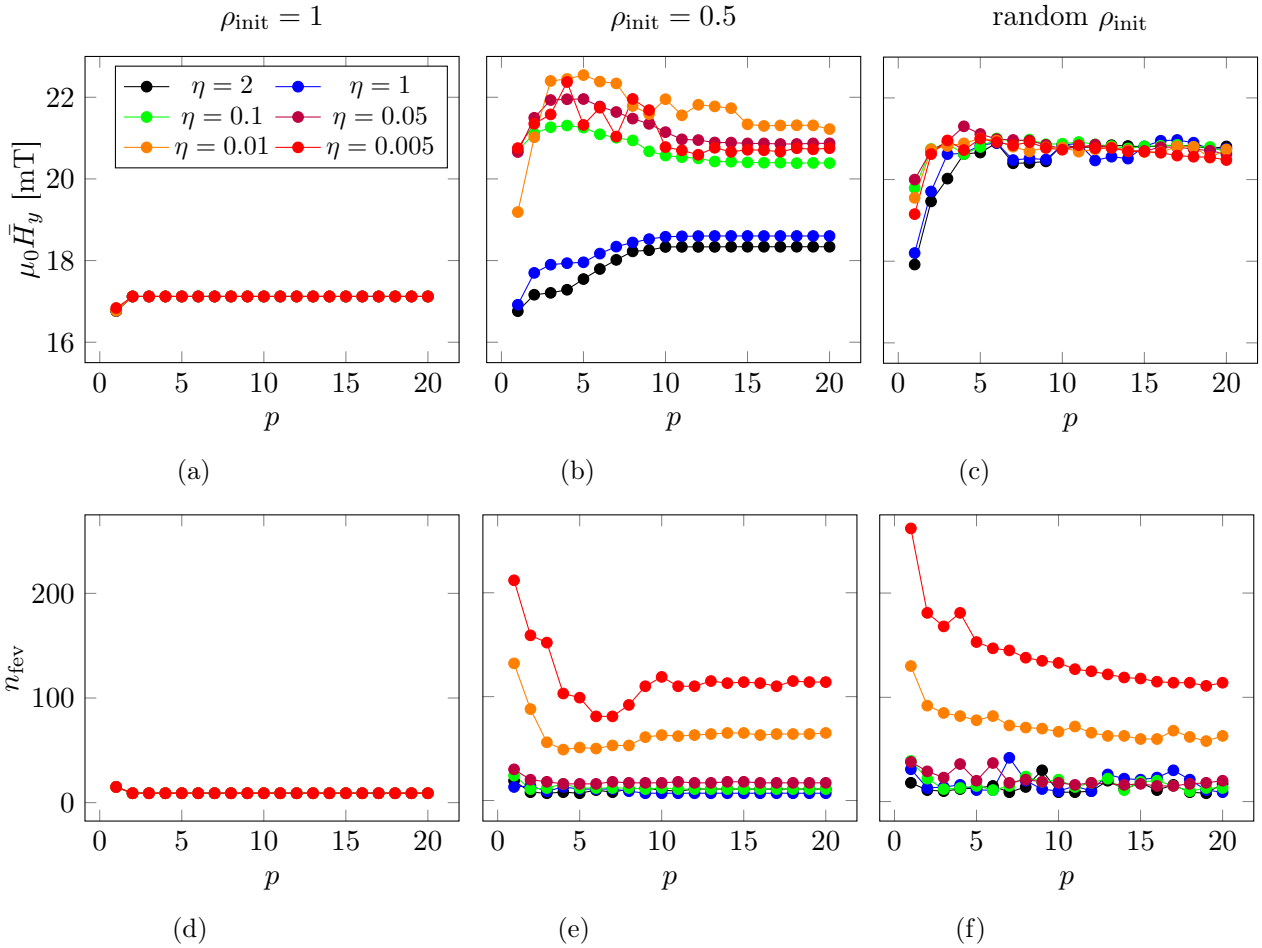

Figure 4.23.: Dependence on the penalty parameter p of the mean field $\mu_0 \bar{H}_y$ ((a) - (c)) and the number of necessary function evaluations n_{fev} ((d) - (f)) for the optimization with $\chi = 10^3$ using the RBTO algorithm with an initial distribution of $\rho_{\text{init}} = 1$ ((a) and (d)), $\rho_{\text{init}} = 0.5$ ((b) and (e)) and a random initialization of ρ ((c) and (f)).

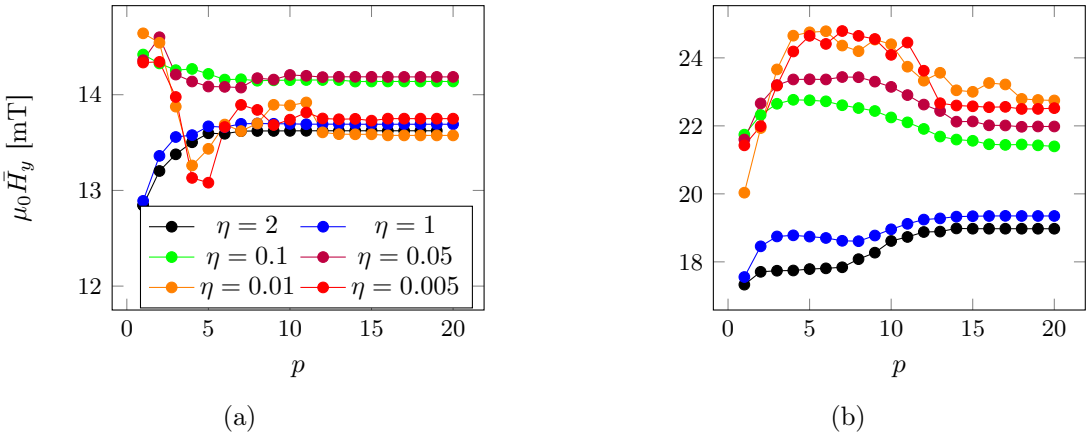

Figure 4.24.: Dependence on the penalty parameter p of the mean field $\mu_0 \bar{H}_y$ for the RBTO algorithm with $\rho_{\text{init}} = 0.5$ for (a) $\chi = 10^2$ and (b) $\chi = 10^4$.

(a) (b) (c)

Figure 4.25.: Optimized topologies for $\chi = 10^4$ with (a) $p = 7$ and $\eta = 0.005$ ($\mu_0 \bar{H}_y = 24.79$ mT), (b) $p = 7$ and $\eta = 0.01$ ($\mu_0 \bar{H}_y = 24.36$ mT) and (c) $p = 6$ and $\eta = 0.01$ ($\mu_0 \bar{H}_y = 24.78$ mT) using the RBTO algorithm.

For the optimization with $\chi = 10^2$ and $\chi = 10^4$ the highest mean fields are again obtained for an initial distribution of $\rho_{\text{init}} = 0.5$. The dependency of the mean field on the penalty parameter p for this case is plotted in Figure 4.24. For $\chi = 10^4$ the dependency is similar to $\chi = 10^3$ and the maximum mean field of 24.79 mT is found for $p = 7$ and $\eta = 0.005$ within 103 function evaluations. The best topology is shown in Figure 4.25a. Again, no detached material islands are present. However, the topology is rather irregular having a large number of holes. For optimizations with a larger η the irregularity decreases as shown in Figure 4.25b and 4.25c where the optimized topologies with $p = 7$ and $\eta = 0.01$ and $p = 6$ and $\eta = 0.01$ are shown respectively. The mean fields produced by these topologies are 24.36 and 24.78 mT respectively. In the case of $\chi = 10^2$, the dependency on the penalty parameter p is different. Here the mean field does not increase with increasing p for low participation values ($\eta < 1$) but the best solution is found for $p = 1$ and $\eta = 0.01$ with 114 function evaluations. In Figure 4.26 the best topology for $\chi = 10^2$ is shown. Furthermore, while for $\chi = 10^3$ and $\chi = 10^4$ the found solutions have a higher mean field compared to the L-BFGS-B solutions, the mean field produced by the topology found using the RBTO algorithm for $\chi = 10^2$ is 0.07% lower. The mean field values, the number of necessary function evaluations and the comparison with the topologies obtained using the L-BFGS-B optimization algorithm are given in Table 4.2.

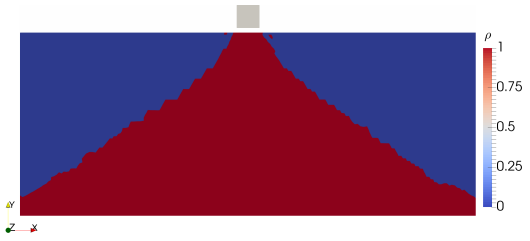

Figure 4.26.: Best optimized topology obtained using the RBTO algorithm for $\chi = 10^2$, $\rho_{\text{init}} = 0.5$, $p = 1$ and $\eta = 0.01$.

In conclusion, the non-linearity introduced by a high value of the susceptibility increases the complexity of the optimization problem. This is even though still a linear material law is used. As a result, in contrast to the optimization performed using a hard magnetic material, the dependency on the penalty parameter p changed and the optimal topologies are now found for higher values of p. Furthermore, using the L-BFGS-B minimization algorithm smaller gradient sizes have been shown to be beneficial. This also lead to the gradient size independent minimization algorithm introduced for the hard magnetic thin film flux guide concentrator to deliver inferior topologies when applied to soft

χ	$\mu_0 \bar{H}_y$ [mT]	n_{fev}	increase [%]
10^2	14.64	114	-0.07
10^3	22.54	51	2.69
10^4	24.79	103	6.21

Table 4.2.: Mean field values $\mu_0 \bar{H}_y$, number of necessary function evaluations n_{fev} and increase with respect to the optimization using the L-BFGS-B optimization algorithm for the optimized topologies using the RBTO algorithm.

magnetic structures. The algorithm therefore has been adapted to perform a stepwise minimization where at each step only a fraction of dofs, defined by the participation parameter η participates in the minimization. The so adapted versions (BTO and RBTO) have been shown to deliver better performing topologies compared to the L-BFGS-B algorithm. However, this was at the expense of introducing a new parameter, the participation. Furthermore, for low participation values regularity problems in the form of detached material islands or holes in the topology appeared. These problems of regularity could possibly be reduced using some kind of homogenization after each optimization step as e.g. shown in [34] where the procedure is called "topology smoother". However, for large mesh sizes these algorithms are computationally quite expensive since they require to investigate each dof and its surrounding locally. Furthermore, in order to avoid asymmetric topologies, symmetry considerations could be considered as e.g. done in [45]. There the topology was divided along a symmetry plane and only half the dofs were actually optimized and mirrored to the symmetric counterparts.

Note, that also optimization of the hard magnetic flux guide concentrator were performed using the binary topology optimization algorithms BTO and RBTO. However, while for $\chi = 0$ the found topologies are completely independent of the participation always delivering the same topology, the change in the obtained topology for a realistic hard magnetic material with $\chi = 0.2$ is negligible.

4.2.5. Optimization of a heat-assisted magnetic recording write head

To showcase the full capabilities of the presented topology optimization method a heat-assisted magnetic recording (HAMR) write head is optimized in order to reduce transition curvature.

HAMR is a means to increase storage density - the amount of data stored per unit area - of magnetic storage devices such as magnetic hard drives [47][48]. In order to increase storage density, the grains of the recording medium have to become smaller. This in turn means that their anisotropy has to be increased to keep them thermally stable. However, higher anisotropy grains require higher magnetic fields in order to change the magnetization direction of a given grain, necessary for information storage. The possible maximum field strength is, however, limited by the available materials. This problem is referred to as the magnetic recording trilemma [49]. HAMR overcomes this problem by spatially heating the recoding medium. This temporarily increases the temperature of the grains. With increasing temperature, the magnetic field necessary to flip a gains magnetization is reduces greatly. Therefore, a comparatively low magnetic field is able to reliably perform the process of writing information to the medium.

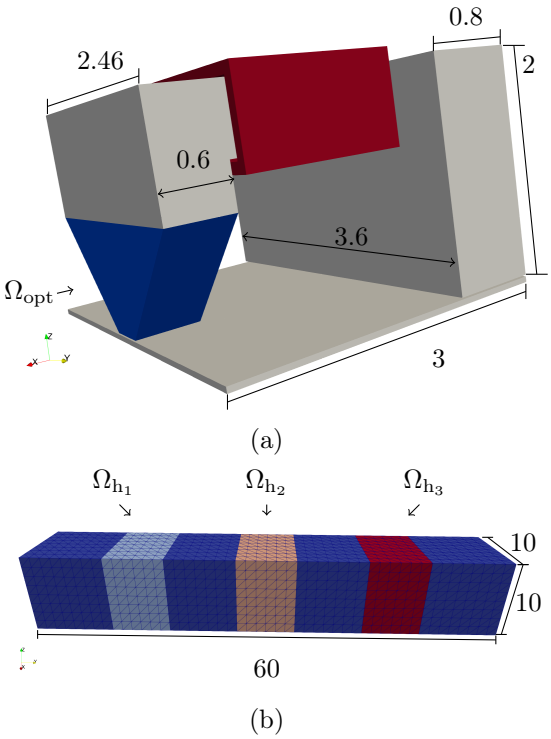

Figure 4.27.: (a) Write head model with optimization region Ω_{opt} highlighted in blue and coil highlighted in red (dimensions in µm) and (b) mesh of the fieldbox used for the topology optimization procedure (dimensions in nm). Figure taken from [30].

In HAMR a plasmonic near-field transducer is used to heat the magnetic recording medium. The heating creates a circular thermal profile inside the magnetic recording medium. In combination with the spatially homogeneous write field of a conventional write head this produces the magnetic bits to become curved as shown e.g. in [50]. This phenomenon is called transition curvature and it represents a significant problem for the read-back process in HAMR. In order to reduce transition curvature either the thermal profile in the magnetic recording medium can be flattened as presented in [51] or the magnetic write field can be shaped as proposed in [50][52]. In order to achieve the second approach, new head designs like forked and split-pole write heads [53][54][55][51] have been presented. Here, the presented topology optimization method is used to optimize the write head tip to create a cross-track (below denoted also as $y-$direction) profile of the recording field counteracting the curvature induced by the thermal profile. The evaluation of the ability of the optimized cross-track field profiles to improve the read-back process in HAMR can be found in [30] and is not presented here, since it is not within the scope of this thesis.

The write head model used for the optimization is presented in Figure 4.27a. Its basic dimension have been taken from [54]. The model includes a soft magnetic underlayer with a thickness of 50

nm below the recording head at a distance of 15 nm. The topology optimization is performed for the head tip only. In order to perform the optimization, an optimization domain Ω_{opt} (indicated in blue in Figure 4.27a) was defined. The optimization domain has a height (z-direction) of 1 µm and a width (y-direction) of 400 nm at the bottom. The fieldbox, where the magnetic field is evaluated, is placed above the underlayer and below the head tip at a z-distance of 2.5 nm from either, at the inner edge of the write head tip. The coil was modeled with a thickness of 100 nm, and outer dimensions of 1.5 µm, 2.7 µm and 0.84 µm in x-, y- and z-direction respectively and a constant distance from the write head of 15 nm.

The mesh used for the complete model consist of 130,029 nodes (678,511 elements). 3969 nodes (18,432 elements) make up the fieldbox mesh and the mesh of the optimization domain Ω_{opt} consists of 103,616 nodes (582,328 elements). In order to obtain a high resolution for the topology where it is most important, the optimization domain is divided into three areas with different mesh resolution with the finest mesh resolution close to the fieldbox. The coil was meshed using 10,010 nodes (29,895 elements).

For the material of the write head a saturation flux density of $B_{\text{s}} = 2.4$ T and an initial susceptibility of $\chi_0 = 1200$ were chosen following [56]. The material was modeled as isotropic non-linear represented by a hyperbolic tangent

$$B(H) = \mu_0 \left(M_{\text{s}} \cdot \tanh\left(\chi_0 / M_{\text{s}} \cdot H \right) + H \right), \tag{4.23}$$

where by setting $M_{\text{s}} = B_{\text{s}}/\mu_0$ the anisotropy field $H_{\text{k}} = 1.6$ kA/m has been omitted, and $H = |\boldsymbol{H}|$. Note, as will be shown below, considering the full non-linear B/H curve of the magnetic material is very time consuming since the time needed to solve the forward problem is dramatically increased with respect to using the B/H curve of the material linearized at the working point. For most optimizations, therefore the linearized material law

$$B(H) = \mu_0 (1 + \chi_0) H \tag{4.24}$$

is used. In order to still consider saturation effects, the linearly optimized topologies delivering the best performance using the linear material law are recalculated using the non-linear material law. The results obtained using the different material laws are then compared. Note that the coil dimensions of the model were chosen arbitrarily. Therefore, the current density was fixed so the write head tip is nearly saturated (see Figure 4.31) at a value of $2 \cdot 10^{11}$ A/m, and was unchanged for all presented non-linear calculations. For the linear calculations the current density is irrelevant due to the linear material law.

The magnetization inside a given grain is written when the temperature inside that grain drops below the necessary write temperature dependent on a given field strength. The point where this happens depends on the distance of the write head tip from the heat pulse center. The optimization is therefore performed for different down-track (negative x-direction) distances of the fieldbox center of $d = 0$, 10, 20, 30 and 50 nm from the inner edge of the write head tip.

The heat pulse used to heat the magnetic recording medium creates a heat profile in cross-track (y-direction) that is strongest in the center and gets lower with increasing distance. Since a stronger write field is necessary to write the magnetic material at lower temperatures the write field must be shaped to be stronger away from the cross-track center in order to counteract the heat pulse profile. For perpendicular magnetic recording the z-component of the write field is responsible for writing the bits. In order to shape the write field, three equally large domains

inside the field box are defined. One in the middle (Ω_{h_2}) and two on each side (Ω_{h_1} and Ω_{h_3}) as also shown in Figure 4.27b. These volumes are then used to define the objective functional

$$\hat{J} = \frac{1}{2}\int_{\Omega_{\mathrm{h}_1}} H_z \,\mathrm{d}V - \int_{\Omega_{\mathrm{h}_2}} H_z \,\mathrm{d}V + \frac{1}{2}\int_{\Omega_{\mathrm{h}_3}} H_z \,\mathrm{d}V. \tag{4.25}$$

When minimized, this objective functional maximizes the field difference between the center evaluation area (Ω_{h_2}) and the two evaluation areas on the sides (Ω_{h_1} and Ω_{h_3}) of the fieldbox. This leads to a cross-track field profile with the desired field shape. Note that each evaluation area has a length in cross-track (y-)direction of 8 nm and Ω_{h_1} and Ω_{h_3} are centered around $y = \pm 16$ nm.

The optimizations are performed using the BTO algorithm as presented in Figure 4.18 and the gradient $\nabla\hat{J}$ is used. As for the other presented examples, the density function ρ, as well as χ, $\boldsymbol{M}_{\mathrm{r}}$, $\boldsymbol{H}_{\mathrm{ext}}$ and the magnetic stray field $\boldsymbol{H}_{\mathrm{d}} = -\boldsymbol{\nabla} u$ and $\boldsymbol{\nabla}\lambda$ are constant within each element while the potential u and the adjoint variable λ are calculated using piecewise linear basis functions ($\mathcal{P}_1$).

In order to illustrate the problem of using an external field with non-vanishing divergence, as discussed in subsection 3.1.2, in Figure 4.28 the magnetization of the write head is compared for a calculation using the external field with and without ensuring it to be divergence free by the method described in subsection 3.1.2. The chaotic behavior of the magnetization vectors clearly shows that the magnetization is not smooth when using a non-divergence free external field. This behavior vanishes when the external field is divergence free.

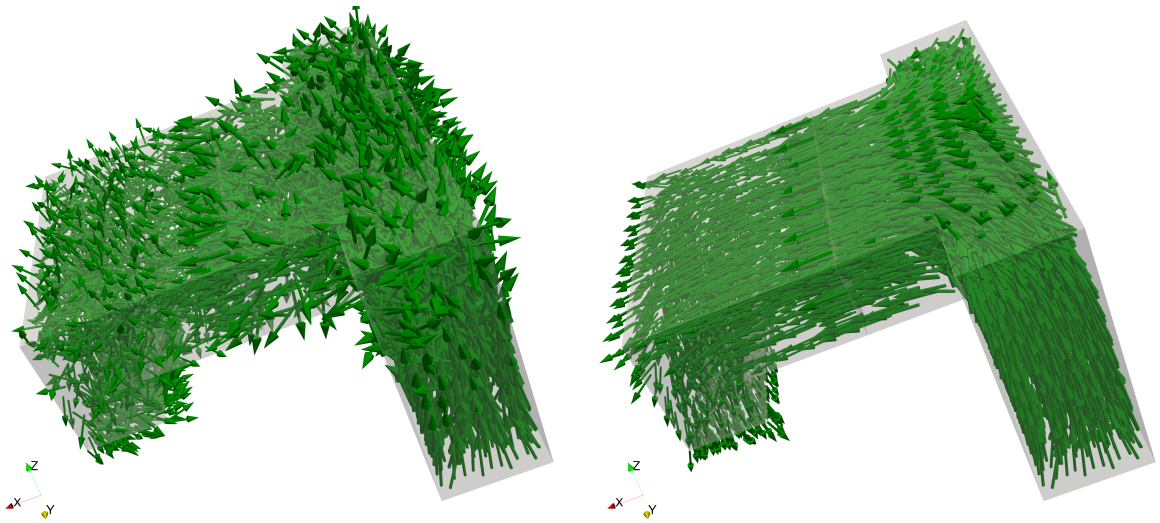

(a) (b)

Figure 4.28.: Write head without optimization domain. The green vectors represent the magnetization. (a) shows the result of a calculation where the external field $\boldsymbol{H}_{\mathrm{ext}}$ has not been ensured to be divergence free as explained in subsection 3.1.2. For the results shown in (b) the external field was divergence free.

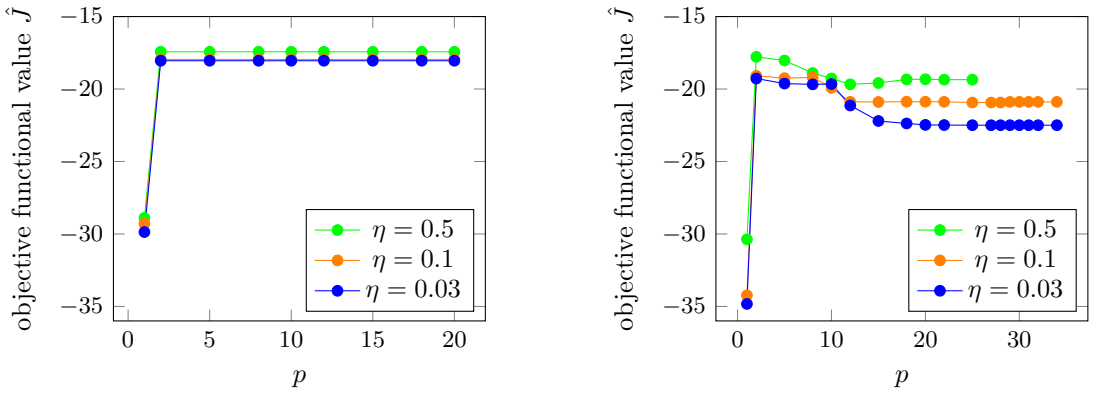

Figure 4.29.: p-dependence of the objective functional $\hat{J}$ for different values of the participation η for (a) $\rho_{\text{init}} = 1$ and (b) $\rho_{\text{init}} = 0.5$.

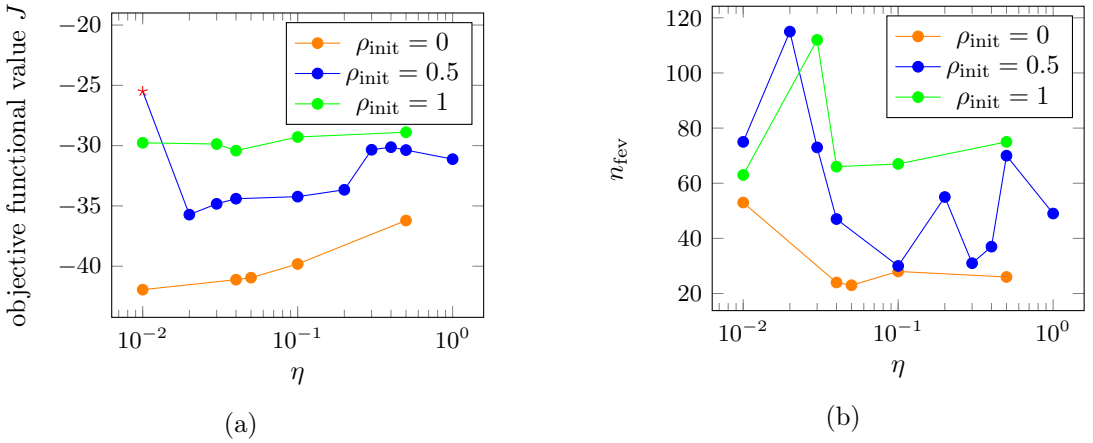

Figure 4.30.: Dependence on η for different ρ_{init} with $p = 1$ of (a) the objective functional value J and (b) the number of necessary function evaluations n_{fev}.

Linear optimization

In Figure 4.29 the results of the optimization using a linearized material law for a fieldbox distance of $d = 10$ nm for an initial distribution of $\rho_{\text{init}} = 1$ and $\rho_{\text{init}} = 0.5$ are shown for different values of the participation parameter η. It can be seen, that the best topologies are found for $p = 1$ for both initial distributions. This is in contrast to the previous example (subsection 4.2.4) where for a comparable susceptibility the best topologies were found for higher values of p. Furthermore, it is visible, that $\rho_{\text{init}} = 0.5$ produces better results compared to $\rho_{\text{init}} = 1$. Since the best topologies are obtained for $p = 1$ this value was also tested using an initial distribution of $\rho_{\text{init}} = 0$. Note, that for $\rho_{\text{init}} = 0$ higher values of p are not possible since for $p > 1$ the gradient as defined in equation (4.16) vanishes. In Figure 4.30 the results with in initial distribution of $\rho_{\text{init}} = 0$ with $p = 1$ are presented and compared with the two other initial distributions of the indicator function ρ. For an initial distribution of $\rho_{\text{init}} = 1$ it can be seen that the objective functional value barely depends on the participation. While for $\rho_{\text{init}} = 0$ the objective functional value decreases with decreasing η down to $\eta = 0.01$ this is also the case for $\rho_{\text{init}} = 0.5$ until there for $\eta = 0.01$ the optimization terminates prematurely with some dofs of ρ still having a value of 0.5. Note, that this case can not occur for $\rho_{\text{init}} = 0$. It is clearly visible, that $\rho_{\text{init}} = 0$ delivers the best topologies. Furthermore, the number of function evaluations necessary n_{fev} is lowest when using $\rho_{\text{init}} = 0$. Note, that it has been verified, that the usage of $\rho_{\text{init}} = 0$ does not deliver better results for the previous example of the soft magnetic thin film flux guide concentrator presented in subsection 4.2.4. The best topology for $d = 10$ nm is found for $\rho_{\text{init}} = 0$ and $\eta = 0.01$ and is presented in Figure 4.31. It shows a slit comparable to a split pole geometry, but additionally a material island extends from between the two prongs towards the back of the write head tip. The material island increases the field difference between the center and the sides of the fieldbox since it directs magnetic flux from the fieldbox center away.

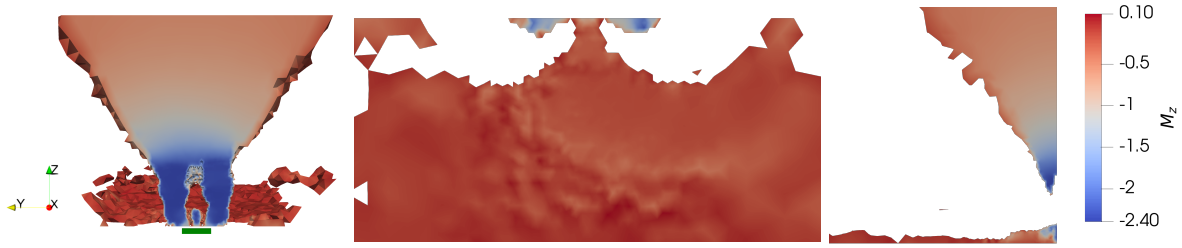

(a) (b) (c)

Figure 4.31.: Best topology found using a linearized material law for a fieldbox distance of 10 nm. In (a) the front view of the compete head tip is shown including the fieldbox in green. In (b) a bottom view slice and in (c) a side view slice through the middle can be seen.

In Figure 4.32 the usage of the gradient $\nabla\hat{J}$ and the derivative $\mathrm{d}\hat{J}$ is compared for two optimizations with $\rho_{\text{init}} = 0.5$ and $p = 1$ for $\eta = 0.1$ and $\eta = 0.03$. It is clearly visible that the gradient finds a lower objective functional value in both cases. Furthermore note that even though the optimization for $\eta = 0.03$ needs fever function evaluations using the derivative, terminating the optimization using the gradient after the same number of optimization steps would still deliver a lower objective function value.

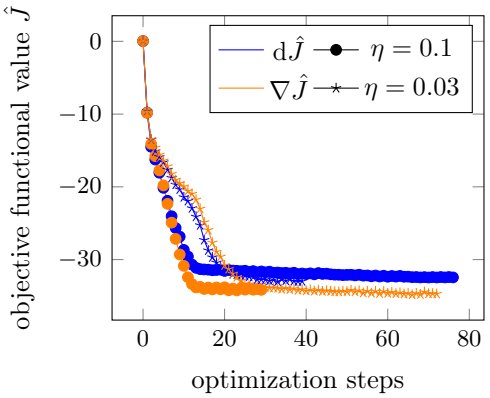

Figure 4.32.: Comparison of derivative $\mathrm{d}\hat{J}$ and gradient $\nabla\hat{J}$ for $\rho_{\text{init}} = 0.5$ and $p = 1$ for two values of η.

$\rho_{\text{init}} = 0$ delivers the best topologies for all distances d. However, with increasing distance from the head tip, the dependence on the participation parameter η changes. While for $d = 0$ and $d = 10$ the objective functional value decreases with decreasing η and the best topologies are found for $\eta = 0.01$ (see Figure 4.29a), with increasing d the value of η for which the best topology is found increases and the topologies obtained for lower participation values become increasingly irregular, showing detached islands. This is shown exemplary in Figure 4.33 where the dependence on η is plotted for $p = 1$ with $\rho_{\text{init}} = 0$ at $d = 20$ nm. It can be seen that the best topology here is found for $\eta = 0.05$ and the objective functional values increases when further decreasing the participation η. Note, that for all distances the best topologies show the same main features, namely, two material prongs divided by a slit with an material island in between similar to the topology shown in Figure 4.31 with only slight changes.

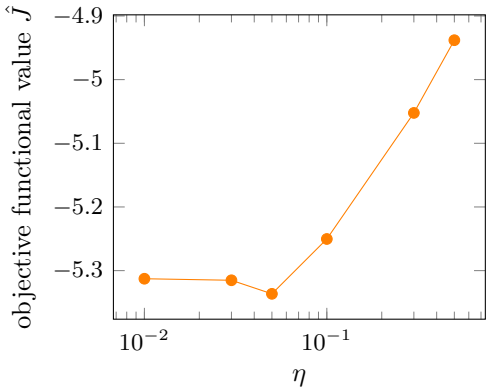

Figure 4.33.: Dependence of the objective functional $\hat{J}$ on η for the optimizations with $\rho_{\text{init}} = 0$ and $p = 1$ at $d = 20$ nm.

The best topologies for each distance d are presented in Table 4.3. In order to incorporate saturation effects, they have been recalculated using the non-linear material law defined in equation (4.23). The obtained cross-track field profiles evaluated along the fieldbox center are shown in Figure 4.34a. It can be seen that the field difference decreases rapidly with increasing distance d. Furthermore, the maximum field strength also decreases with increasing d. This is also visualized in Figure 4.34b and 4.34c. There, the mean maximal field $\bar{H}_z\left(\Omega_{\mathrm{h}_{1,3}}\right) = \bar{H}_z = \frac{\bar{H}_z\left(\Omega_{\mathrm{h}_1}\right) + \bar{H}_z\left(\Omega_{\mathrm{h}_3}\right)}{2}$ and the field difference $\Delta\bar{H}_z = \bar{H}_z\left(\Omega_{\mathrm{h}_2}\right) - \bar{H}_z\left(\Omega_{\mathrm{h}_{1,3}}\right)$ are plotted in dependence of the distance d for the non-linearly recalculated best topologies ob-

d	η	$\mu_0\Delta\bar{H}_z$ [mT]	$\mu_0\bar{H}_z$ [mT]
0	0.01	211.34	651.28
10	0.01	73.69	305.82
20	0.03	22.29	294.38
30	0.05	11.37	230.69
40	0.1	4.46	52.37
50	0.1	2.48	43.04

Table 4.3.: Participation value η, field difference $\mu_0\Delta\bar{H}_z$ and mean maximal field strength $\mu_0\bar{H}_z\left(\Omega_{\mathrm{h}_{1,3}}\right)$ for the best topologies for each distance d.

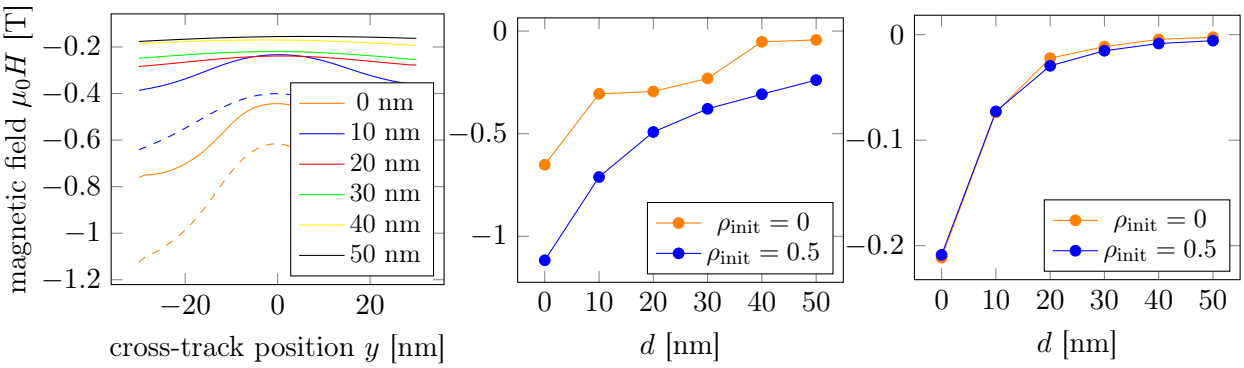

(a) (b) (c)

Figure 4.34.: (a) Cross-track field profiles (H_z) at different distances d from the write head tip for the linearly optimizations (continuous lines) and the non-linear optimizations (dashed lines) obtained from the respective optimized topologies with $\rho_{\text{init}} = 0$ and (b) dependence of the respective field difference $\mu_0 \Delta \bar{H}_z$ and (c) the mean maximal field strength $\mu_0 \bar{H}_z \left(\Omega_{\text{h}_{1,\text{h}_3}}\right)$ on the distance d for the best topologies with $\rho_{\text{init}} = 0$ and $\rho_{\text{init}} = 0.5$.

tained with $\rho_{\text{init}} = 0$ and $\rho_{\text{init}} = 0.5$ (all with $\eta = 0.1$ as presented in [30]). Note, that $\bar{H}_z \left(\Omega_{\text{h}_X}\right) = \int_{\Omega_{\text{h}_X}} H_z \, \text{d}V/V \left(\Omega_{\text{h}_X}\right)$ is the mean of the z-field component inside the respective domain Ω_{h_X} and $V \left(\Omega_{\text{h}_X}\right)$ is the corresponding volume. Comparing the results obtained using $\rho_{\text{init}} = 0$ and $\rho_{\text{init}} = 0.5$ with respect to the mean field $\bar{H}_z \left(\Omega_{\text{h}_{1,\text{h}_3}}\right)$ it can be seen that the topologies obtained with $\rho_{\text{init}} = 0.5$ produce a stronger z-field component H_z. Looking at the field difference $\Delta \bar{H}_z$ it can be seen that while for $d < 20$ nm $\rho_{\text{init}} = 0$ produced a slightly larger field difference, for $d \geq 20$ nm this is no longer the case and the field differences created by the topologies obtained with $\rho_{\text{init}} = 0.5$ become larger. This is in contradiction to the results of the optimizations using the linearized material law, where the objective functional (and with it the field difference) is always lower (larger) for the topologies obtained with $\rho_{\text{init}} = 0$. This divergence between the results obtained using the linearized material law and the recalculation using the full non-linear material characteristics shows the necessity of using the full non-linear material characteristics during optimization.

Non-linear material law

The optimizations for $d = 0$ and $d = 10$ nm have been repeated incorporating the full non-linear material characteristics during optimization. In Figure 4.36 the objective functional value $\hat{J}$ is plotted in dependence of the penalty parameter p for different values of the participation parameter η for optimization with $\rho_{\text{init}} = 0.5$ at $d = 10$ nm. It can be seen that the main dependencies of the optimization stay unchanged and the best topologies are found for $p = 1$. Furthermore, again $\rho_{\text{init}} = 0$ delivers the best results as shown in Figure 4.36 where the objective functional value $\hat{J}$ is plotted in dependence of the participation parameter η for $\rho_{\text{init}} = 0$ and $\rho_{\text{init}} = 0.5$ for $p = 1$. It can be seen that the topologies found using $\rho_{\text{init}} = 0$ are better and furthermore some optimization using $\rho_{\text{init}} = 0.5$ terminated prematurely with dofs of ρ still having the initial value. Note, that here for $\rho_{\text{init}} = 0$ the best topology is already found for $\eta = 0.2$ and the objective functional value increases when further decreasing η. The best topology is shown in Figure 4.37. The field profile is also shown in Figure 4.34a (dashed lines) for comparison with the field profiles obtained from the optimizations using a linearized material law. Regarding field difference $\mu_0 \Delta \bar{H}_z$ and mean maximal field strength $\mu_0 \bar{H}_z (\Omega_{\text{h}_1,\text{h}_3})$, with 113.81 mT and 543.97 mT respectively the non-linearly optimized topologies show an increase of 54.44% and 77.87% respectively with respect to the linearly optimized topologies.

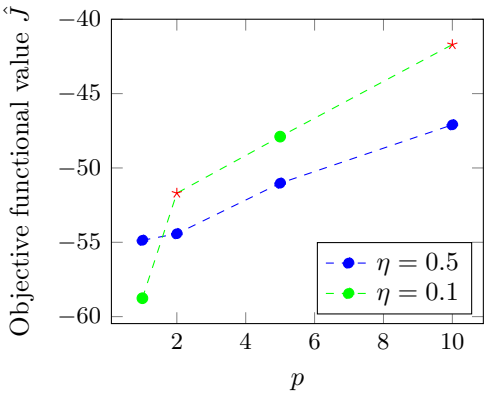

Figure 4.35.: Dependence of the objective functional value $\hat{J}$ on the parameter p for different participation values η for $\rho_{\text{init}} = 0.5$. The red stars indicate simulations for which the optimization terminates prematurely. Picture taken from [30].

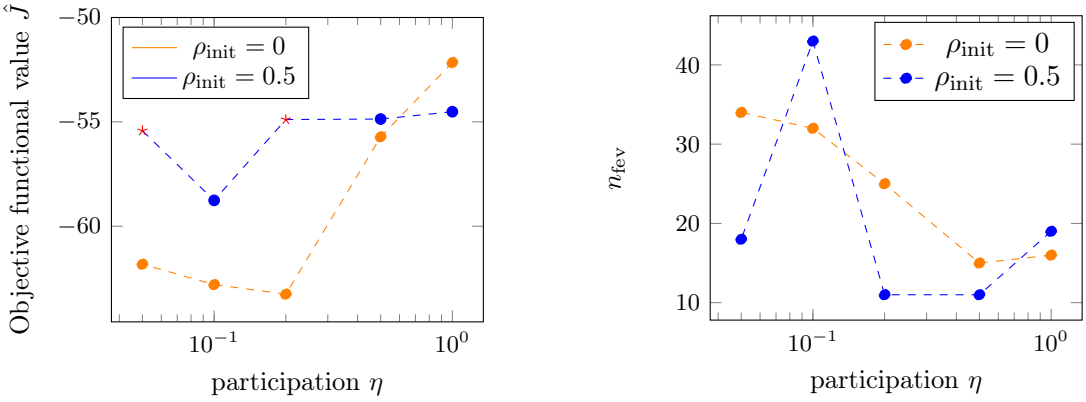

Figure 4.36.: Dependence of the objective functional $\hat{J}$ and the number of necessary function evaluations n_{fev} on the participation parameter η, both for the non-linear topology optimization at a distance of $d = 10$ nm. The red stars indicate simulations for which the optimization terminates prematurely.

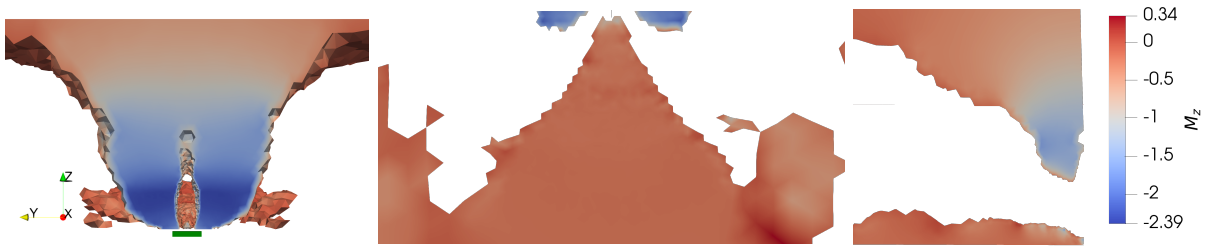

(a) (b) (c)

Figure 4.37.: Best topology found using a non-linear material law for a fieldbox distance of 10 nm. In (a) the front view of the compete head tip is shown including the fieldbox in green. In (b) a bottom view slice and in (c) a side view slice through the middle can be seen.

An important factor when using the full non-linear material characteristics during optimization is the increase in computational effort. While for $d = 10$ nm with $\rho_{\text{init}} = 0$, for the linear optimization with $\eta = 0.1$, solving the forward problem on average needs 4 linear iterations, using the non-linear material law this increases to on average 357 linear iterations necessary to solve the forward problem using the inexact Newton method. For $\rho_{\text{init}} = 0$ computational effort decreases by half to on average 160 necessary linear iterations for also $\eta = 0.1$. This is since with $\rho_{\text{init}} = 0$ the system matrix is sparser on average during optimization. However, the increase in computational effort to solve the forward problem is still by almost an order of two magnitudes. Note that solving the adjoint equation requires the same computational effort since it is a linear equation in both cases.

For $d = 0$ nm no detailed dependency on η was calculated due to the increased time demand of the optimizations and with $\rho_{\text{init}} = 0$ only an optimization with $\eta = 0.1$ was performed. The respective field profile is also shown in Figure 4.34a. With a field difference of $\mu_0 \Delta \bar{H}_z = 304.11$ mT and a mean maximal field strength of $\mu_0 \bar{H}_z \left(\Omega_{\text{h}_1,\text{h}_3}\right) = 915.55$ mT using the full non-linear material characteristics during optimization delivered an improvement by 43.90% and 40.58% respectively.

In conclusion, optimizations using a linearized material law as well as incorporating the full non-linear material characteristics have been performed using the binary optimization algorithm BTO and the dependency on the initial distribution ρ_{init} of the indicator function ρ and the participation parameter η has been investigated.

It has been found, that the optimizations using an initial distribution of $\rho_{\text{init}} = 0$ perform best for both cases, using the linearized and the non-linear material law. Regarding the participation parameter η for which the best topology is found, a dependence on the distance d was shown for the linear optimizations. In detail, while for $d = 0$ and $d = 10$ nm the objective functional value decreases with decreasing η down to at least $\eta = 0.01$, this is different for higher values of d where already for $\eta > 0.01$ the best topology is found and the objective functional value increases again when further decreasing η.

The computational demand increases by almost two orders of magnitude in terms of the number of linear iterations necessary to solve the forward problem for the optimizations incorporating the full non-linear material characteristics. Therefore, a detailed dependence on the participation parameter η of the non-linear optimizations was not calculated for each distance d. However, for

$d = 10$nm the objective functional value decreases with decreasing η until the best topology is found for $\eta = 0.2$. Regarding the obtained mean field difference a maximum of $\mu_0 \Delta \bar{H}_z = 304.11$ mT was found for the non-linear optimization at $d = 0nm$ with $\eta = 0.1$. The non-linear optimizations produced topologies that on average increases the field difference by 49.17% with respect to the linear optimizations, showing the advantage of incorporating the full non-linear material law during optimization. However, the topologies optimized using a linearly approximated material law produce the same main features as the non-linearly optimized topologies. Only the features themselves, namely the size of the two prongs, the size of the gap between the prongs and the size and position of the material island between the prongs differ.

4.3. Topology optimization of an ideal permanent magnet

An ideal permanent magnet does not change its magnetization state due to its own stray field or in other terms its susceptibility χ is equal zero. When performing topology optimization, therefore it is not necessary to solve the full magnetostatic Maxwell's equation as done above, but it is reasonable to assume a homogeneous magnetization $\boldsymbol{M}_0$ having the value of the materials remanence magnetization $\boldsymbol{M}_\mathrm{r}$ and to work with equation (3.26). Doing so reduces the computational effort greatly.

Having only the magnetization as material function, topology optimization is introduced by

$$\boldsymbol{M}(\rho) = \rho^p \boldsymbol{M}_0. \tag{4.26}$$

Inserting this into the forward problem given by equation (3.26) it follows

$$F = \boldsymbol{\nabla} \cdot (\boldsymbol{\nabla} u - \rho^p \boldsymbol{M}_0) = 0 \tag{4.27}$$

with the open boundary condition

$$u(\boldsymbol{r}) \to \mathcal{O}\left(\frac{1}{|\boldsymbol{r}|}\right) \quad \text{for} \quad |\boldsymbol{r}| \to \infty. \tag{4.28}$$

Again, F is a mapping $U \times R \to Z$ with appropriate Hilbert spaces with $u \in U$ and $\rho \in R$ and the L^2-inner product. And the reduced optimization problem can again be written as

$$\min_{\rho \in R} \hat{J}(u(\rho), \rho). \tag{4.29}$$

4.3.1. Adjoint equation

In the same way as for the full Maxwell problem starting with ∂F_u^*, the operator ∂F_u is obtained from the Fréchet derivative (Definition 2) with $w \in U$ as

$$\partial F_u(u(\rho), \rho; w) = \lim_{\epsilon \to 0^+} \frac{F(u + \epsilon w, \rho) - F(u, \rho)}{\epsilon} = \Delta w \tag{4.30}$$

the Laplace operator. The Laplace operator is self-adjoint as can easily be checked using definition (4) if the same boundary conditions as valid for the potential u are enforced on the adjoint variable λ.

The adjoint equation in the case of a fixed magnetization $\boldsymbol{M}_0$ therefore becomes:

$$\Delta \lambda = \mathcal{R}(\partial J_u) \tag{4.31}$$

with open boundary condition

$$\lambda(\boldsymbol{r}) \to \mathcal{O}\left(\frac{1}{|\boldsymbol{r}|}\right) \quad \text{for} \quad |\boldsymbol{r}| \to \infty. \tag{4.32}$$

The dependency on the scalar potential u on the right hand side of equation (5.7) can be rewritten as a dependency on the field $\boldsymbol{H}$ in the same way as above (equations (4.9) and (4.10)) giving equation (5.7) in its weak form after partial integration of the left hand side as

$$\int_{\mathbb{R}^3} \Big(-\boldsymbol{\nabla}\lambda + \mathcal{R}(\partial J_{\boldsymbol{H}}) \Big) \cdot \boldsymbol{\nabla} v \, \mathrm{d}V, \tag{4.33}$$

where again the boundary term vanished due to the boundary condition on λ. This is the weak form of

$$\boldsymbol{\nabla} \cdot \left(\boldsymbol{\nabla} \lambda - \mathcal{R} \left(\partial J_{\boldsymbol{H}} \right) \right) = 0 \tag{4.34}$$

an equation identical to the forward problem in equation (4.27), with u replaced by λ and $\rho^p \boldsymbol{M}_0$ replaced by $\mathcal{R} \left(\partial J_{\boldsymbol{H}} \right)$. Therefore, again the same algorithm used to solve the forward problem can easily be used to solve the adjoint problem.

4.3.2. Gradient

To calculate the full gradient, the operator ∂F_ρ is obtained from the Fréchet derivative (Definition 2) with $r \in R$ as

$$\partial F_\rho \left(u \left(\rho \right), \rho; r \right) = \partial F_\rho r = \lim_{\epsilon \to 0^+} \frac{F \left(u \left(\rho \right), \rho + \epsilon r \right) - F \left(u, \rho \right)}{\epsilon} = \boldsymbol{\nabla} \cdot \left(p \rho^{p-1} r \boldsymbol{M}_0 \right) \tag{4.35}$$

and the dual operator ∂F_ρ^* is calculated using Definition 4 giving

$$\begin{gathered} \left(\partial F_\rho \, r, \lambda \right) = \int_{\mathbb{R}^3} \boldsymbol{\nabla} \cdot \left(p \rho^{p-1} r \boldsymbol{M}_0 \right) \lambda \, \mathrm{d}V = \\ - \int_{\mathbb{R}^3} p \rho^{p-1} r \boldsymbol{M}_0 \cdot \boldsymbol{\nabla} \lambda \, \mathrm{d}V = - \int_{\mathbb{R}^3} r p \rho^{p-1} \boldsymbol{M}_0 \cdot \boldsymbol{\nabla} \lambda \, \mathrm{d}V = \left(r, \partial F_\rho^* \lambda \right). \end{gathered} \tag{4.36}$$

Here the boundary integral again vanishes λ satisfies the boundary condition (5.6).

For the full gradient we therefore get

$$\begin{gathered} \nabla \hat{J}_p = - \partial F_\rho^* \lambda + \mathcal{R} \left(\partial J_\rho \right) = \\ p \rho^{p-1} \boldsymbol{M}_0 \cdot \boldsymbol{\nabla} \lambda + \mathcal{R} \left(\partial J_\rho \right). \end{gathered} \tag{4.37}$$

4.3.3. Optimization of a hard magnetic thin film flux guide concentrator

In same way as above, a hard magnetic thin film flux guide concentrator is optimized using the fixed magnetization approximation. For the optimization the same mesh as presented in Figure 4.1 and the same objective functional given by equation (4.22)is used. The remanence magnetization is also set as $\boldsymbol{M}_{\mathrm{r}} = 280000$ A/m and the anisotropy axis is chosen as the y-axis.

For the optimization, the binary topology optimization algorithm (BTO) with $\eta = 2$ that is identical to gradient independent minimization algorithm is used. Note, that in the same way as when using the full Maxwell problem, changing the participation η, in the case of using a hard magnetic material only changes the number of necessary function evaluations and the same topology is obtained. The optimization was again performed for the three different initial distributions of the indicator function ρ.

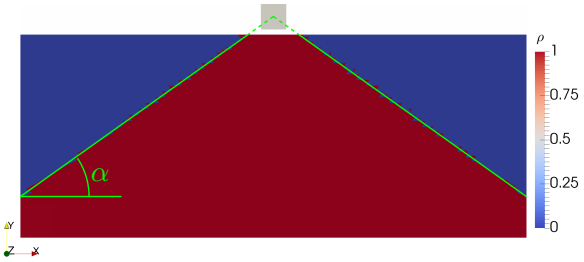

Figure 4.38.: Best optimized topology obtained using the fixed magnetization approximation and comparison with the analytical solution (green line).

The results show, that the same topology is found for all initial distributions within 3 function evaluations independent of p at least for $p \leq 6$ without intermediate values of ρ in the optimized topology. The found topology is shown in Figure 4.38 where it is also compared to the analytical solution as derived in subsubsection 4.2.3. It differs from the best topology obtained using the full Maxwell problem (Figure 4.10) by 205 cells and produces a mean field of $\bar{H}_y = 21.09$ mT inside the domain Ω_{h}. Note, that this value is inherently different from the field value obtained using the full Maxwell's equation due to the different calculation methods. Using the obtained topology and recalculating the field with the full Maxwell's equation with $\chi = 0$ the obtained mean field is $\bar{H}_y = 22.82$ mT which is 0.01 mT below the value obtained form the topology optimized using the full Maxwell problem.

4.4. Conclusion

Within this chapter, two topology optimization algorithms based on the density approach of topology optimization were presented. The first algorithm uses the full magnetostatic Maxwell problem to optimize the topology of a magnetic structure while the second algorithm is based on an approximation using a fixed magnetization configuration as source. Several examples of optimizations of hard as well as soft magnetic structures have been shown and the dependencies of the different optimizations on the penalty parameter p as well as on other parameters for the respective minimization algorithms used were investigated

The optimization of a hard magnetic structure has been shown to be rather straightforward since the optimization depends on ρ linearly. The best topologies in this case are obtained using a gradient size independent minimization algorithm where all dofs of ρ are set to 0 or 1 within one iteration following the sign of the gradient. Furthermore, the best topologies are found independently of the initial distribution ρ_{init} of the indicator function ρ and the penalty parameter p, suggesting the usage of $\rho_{\text{init}} = 1$ and $p = 1$ as default values. Additionally, it has been shown that the approximation of an ideal hard magnetic material ($\chi = 0$) is valid for a realistic permanent magnetic material with a susceptibility of $\chi = 0.2$ for the algorithm solving the full Maxwell problem. The approximation allows for a faster optimization with the number of necessary function evaluations lower by two orders of magnitudes while the obtained field difference is negligible ($< 0.1‰$) and the obtained topology differs by only 0.66% of dofs. Additionally, when optimizing the topology of hard magnetic materials, the approximation using a fixed magnetization as source can be used. Doing so, the dependencies on the penalty parameter p are identical, and using the gradient size independent minimization algorithm for $p = 1$ the best topology is obtained within 3 function evaluations. The obtained topology differs from the one obtained by solving the full Maxwell problem with $\chi = 0$ by 1.2% of dofs and the field differs by 0.4%. Note, since solving the equations appearing for the fixed magnetization approximation is computationally less demanding, this approximation is the preferred method when optimizing permanent magnetic material. Note furthermore that using more complex objective functionals with several, possibly competing terms the optimization is expected to become more involved, and the binary topology optimization algorithm introduced for the optimization of soft magnetic structures may become beneficial here as well.

For soft magnetic structures, the non-linearity introduced by the susceptibility χ leads to a higher complexity of the optimization problem already for simple objective functionals. This can be seen in the strong dependence on the penalty parameter p for the optimization of the soft magnetic thin film flux guide concentrator and by the fact, that the simple gradient size independent minimization algorithm does not deliver satisfying results anymore. The minimization algorithm has therefore been expanded to a binary topology optimization algorithm reducing the number of dofs participating in each iteration. Using this algorithm the obtained topologies are improved, but at the cost of introducing a new parameter, the participation η. Furthermore, a comparison of the two presented soft magnetic examples shows, that for different problems the penalty parameter p, as well as the initial indicator function ρ_{init} for which the best topology is obtained, are different. While for the example of a soft magnetic thin film flux guide concentrator for different values of χ the best topologies were found for higher values of p and $\rho_{\text{init}} = 0.5$, for the optimization of a HAMR write head $\rho_{\text{init}} = 0$ and $p = 1$ were optimal. Furthermore, comparing the optimizations using a linearized material law and optimization incorporating the full non-linear material characteristics, it has been shown that whenever saturation effects play a role, considering the full non-linear material characteristics during optimization improves the obtained

topologies substantially. However, this goes at the price of significantly higher computational effort.

5. Source reconstruction

This chapter deals with the problem of reconstructing the magnetic source of a given magnetic structure from measurements of its stray field. The chapter is structured as follows. First, the term source reconstruction is introduced in general terms. Thereafter, in the next section, the case of using the magnetization as control variable is discussed. The forward problem is presented and the adjoint equation and the gradient are derived. In the next section, as an example the reconstruction of a magnetic flower state inside a permanent magnetic unit cube is presented. In the following section, the case of using fictitious magnetic charges as control variables is introduced and again the respective adjoint equation and the gradient are derived. The example of the unit cube is then also calculated using this approach. Thereafter, the dependence of the source reconstruction procedure on the size and position of input measurements is investigated in detail using both methods and the results are compared. Parts of this chapter have previously been published in [57] and [58].

When performing source reconstruction, the goal is to reconstruct the magnetization state of a given magnetic structure from measurements of its magnetic stray field. This is done to gain information about the magnetization state for e.g. quality control. Furthermore, using the obtained magnetization state, the stray field can be extrapolated to regions that might not be accessible to measurement. Source reconstruction problems have e.g. been used to investigate the magnetization distribution inside magnetic rollers used in printers [59], to investigate ferromagnetic shell structures [60], magnetically biased chokes [16] or to characterize the magnetization of permanent magnets [61] .

Reconstructing the magnetic source means obtaining a magnetization state that produces a magnetic stray field identical to field measurements of the corresponding magnetic structure. The objective functional used to perform the source reconstruction is given by

$$J\left(\boldsymbol{H}\left(p\right),p\right)=R\left(\boldsymbol{H}\left(p\right)-\boldsymbol{H}_{\mathrm{m}}\right)+\alpha T\left(p\right), \tag{5.1}$$

where $R\left(\boldsymbol{H}\left(p\right)-\boldsymbol{H}_{\mathrm{m}}\right)$ is the residual term depending on the difference between the calculated stray field $\boldsymbol{H}$ and the field measurements $\boldsymbol{H}_{\mathrm{m}}$. p refers to the control variable that can e.g. be the magnetization $\boldsymbol{M}$ or, as will be seen below, fictitious magnetic volume and surface charges (ρ_{m} and σ_{m}). $T\left(p\right)$ is called regularization term. It enforces some kind of additional constraint on the control variable (Tikhonov regularization). The necessity to impose additional constraints on the control variable by means of regularization has two reasons. On the one hand, depending on the kind of control variable, the source reconstruction problem might not have a unique solution and hence is inherently ill-posed. This will be seen below when using the magnetization $\boldsymbol{M}$ as control variable. In this case, the regularization can be used to select a distribution of the control variable with specific properties from the multitude of possible solutions. On the other hand, the measured field data used as input for the source reconstruction will always be subject to noise. Since the inverse algorithm tries to produce a source that creates a field that coincides with the input field as good as possible, the source will have features that are not based on the "real" magnetic field but are introduced by the noise. This is called over-fitting. In this case, the

regularization performs a smoothing of the source and thereby the produced field. The choice of regularization term depends on the control variable used and the assumptions made regarding the source that is to be reconstructed. However, whatever regularization term is used, it is crucial to apply it with the right strength. The parameter controlling the strength of the regularization is the regularization (or Tikhonov) parameter α. If it is chosen to low, the regularization will not be strong enough to prevent over-fitting and if chosen to high, over smoothing appears and the control variable is no longer able to reconstruct the target source. A way to chose the right size of the regularization parameter α is the so called L-curve method that will be introduced in detail below (subsubsection 5.1.4).

Note, that this chapter focuses on reconstructing the magnetic source of a given magnetic structure i.e. the magnetization state or a distribution of fictitious magnetic charges. However, it is also possible to reconstruct the topology of a magnetic structure from measurements of its stray field by using the methods introduced in the previous chapter (chapter 4) in combination with an objective functional of the same form. The control would then again be the density indicator function ρ.

Furthermore note, that the techniques introduced within this chapter can also be used to design the magnetization state of a magnetic structure in order to obtain a specific magnetic stray field. To this aim, a desired magnetic field can be used as input as $\boldsymbol{H}_{\mathrm{m}}$ or a different objective functional, e.g. of the form used for topology optimization in the previous chapter, can be used. The kind of regularization used might then be different from the regularization terms used within this chapter. An example of the design of a magnetization state, the optimal design of a Halbach cylinder creating a homogeneous stray field inside of the cylinder, was published in [57].

5.1. Using the magnetization as control variable

Using the magnetization $\boldsymbol{M}$ as control or design variable the forward problem from equation (3.26) reads

$$F\left(u\left(\boldsymbol{M}\right),\boldsymbol{M}\right)=\boldsymbol{\nabla}\cdot\left(\boldsymbol{\nabla}u-\boldsymbol{M}\right)=0 \tag{5.2}$$

with open boundary condition given by equation (3.27), as derived in section 3.2. Here again u is a scalar function from a Hilbert Space U, $\boldsymbol{M}$ is a vector valued function from an appropriate Hilbert space M and F is a mapping $U\times M\rightarrow Z$ into another appropriate Hilbert space Z, with all Hilbert space having the L^2-inner product defined.

The reduced optimization problem in this case is given by

$$\min_{\boldsymbol{M}\in M}\ \hat{J}\left(u\left(\boldsymbol{M}\right),\boldsymbol{M}\right). \tag{5.3}$$

5.1.1. Adjoint equation

The adjoint equation is derived by first calculating ∂F_u in order to then obtain ∂F_u^*. From the Fréchet derivative defined in Definition 2 follows for a $w\in U$

$$\partial F_u\left(u\left(\boldsymbol{M}\right),\boldsymbol{M};w\right)=\partial F_u w=\lim_{\epsilon\rightarrow 0^+}\frac{F\left(u+\epsilon w,\boldsymbol{M}\right)-F\left(u,\boldsymbol{M}\right)}{\epsilon}=\Delta w. \tag{5.4}$$

∂F_u therefore is the Laplace operator. Since the Laplace operator is self-adjoint if the same boundary conditions as valid for the potential u are enforced on the adjoint variable λ - as can easily be checked using Definition 4 - the adjoint equation becomes:

$$\Delta\lambda=\mathcal{R}\left(\partial J_u\right) \tag{5.5}$$

with boundary condition

$$\lambda\left(\boldsymbol{r}\right)\rightarrow\mathcal{O}\left(\frac{1}{|\boldsymbol{r}|}\right)\quad\text{for}\quad|\boldsymbol{r}|\rightarrow\infty. \tag{5.6}$$

Following equations (4.9) and (4.10) the dependency on the scalar potential u on the right hand side of equation (5.5) can again be rewritten as a dependency on the field $\boldsymbol{H}$, giving equation (5.5) in its weak form after partial integration of the left hand side as

$$\int_{\mathbb{R}}\Big(-\boldsymbol{\nabla}\lambda+\mathcal{R}\left(\partial J_{\boldsymbol{H}}\right)\Big)\cdot\boldsymbol{\nabla}v\,\mathrm{d}V, \tag{5.7}$$

where again the boundary term vanished due to the boundary condition on λ. This is the weak form of

$$\boldsymbol{\nabla}\cdot\left(\boldsymbol{\nabla}\lambda-\mathcal{R}\left(\partial J_{\boldsymbol{H}}\right)\right)=0, \tag{5.8}$$

an equation identical to the forward problem in equation (5.2), with u replaced by λ and $\boldsymbol{M}$ replaced by $\mathcal{R}\left(\partial J_{\boldsymbol{H}}\right)$. Therefore, again the same algorithm used to solve the forward problem can be used to solve the adjoint problem.

5.1.2. Gradient

To calculate the full gradient, the operator $\partial F_{\boldsymbol{M}}$ is obtained for $\boldsymbol{m} \in M$ from the Fréchet derivative (Definition 2) as

$$\partial F_{\boldsymbol{M}}\left(u\left(\boldsymbol{M}\right), \boldsymbol{M}; \boldsymbol{m}\right) = \partial F_{\boldsymbol{M}}\, \boldsymbol{m} = \lim_{\epsilon \to 0^+} \frac{F\left(u\left(\boldsymbol{M}\right), \boldsymbol{M} + \epsilon \boldsymbol{m}\right) - F\left(u, \boldsymbol{M}\right)}{\epsilon} = -\boldsymbol{\nabla} \cdot \boldsymbol{m} \tag{5.9}$$

and the dual operator $\partial F^*_{\boldsymbol{M}}$ is calculated using Definition 4 giving

$$\left(\partial F_{\boldsymbol{M}}\, \boldsymbol{m}, \lambda\right) = -\int_{\mathbb{R}^3} \boldsymbol{\nabla} \cdot \boldsymbol{m}\, \lambda \,\mathrm{d}V = \int_{\mathbb{R}^3} \boldsymbol{m} \cdot \boldsymbol{\nabla} \lambda \,\mathrm{d}V = \left(\boldsymbol{m}, \partial F^*_{\boldsymbol{M}} \lambda\right). \tag{5.10}$$

Here the boundary integral again vanished since λ satisfies the boundary condition (5.6).

For the full gradient we therefore get from equation (2.22)

$$\nabla \hat{J}_{\boldsymbol{M}} = -\boldsymbol{\nabla} \lambda + \mathcal{R}\left(\partial J_{\boldsymbol{M}}\right). \tag{5.11}$$

5.1.3. Uniqueness of the obtained solution

When solving the forward problem (equation (5.2)), as presented in subsection 3.2.2, the magnetization $\boldsymbol{M}$ does not appear independently in the respective equations, but its divergence $\boldsymbol{\nabla} \cdot \boldsymbol{M}$ is used (compare equation (3.28)). This has implications for the uniqueness of the solution of the source reconstruction problem. In detail, consider that what is obtained from solving the forward problem is the magnetic stray field $\boldsymbol{H}$ as the gradient of its solution u. The uniqueness theorem for Poisson's equation states that for problems with boundary conditions like valid here (equations (3.30) - (3.32)) the gradient of the solution - and therefore in this case the stray field - is unique for a given source term. Now since the source term is the divergence of the magnetization looking at the Helmholtz decomposition of the magnetization

$$\boldsymbol{M} = \boldsymbol{\nabla} \phi + \boldsymbol{\nabla} \times \boldsymbol{\psi}, \tag{5.12}$$

one can see that any solenoidal part of the magnetization vanishes due to $\boldsymbol{\nabla} \cdot (\boldsymbol{\nabla} \times \boldsymbol{\psi}) = 0$ and is therefore not part of the source term. When performing source reconstruction, the obtained magnetization $\boldsymbol{M}$ therefore is ambiguous since every other magnetization $\boldsymbol{M}' = \boldsymbol{M} + \boldsymbol{\nabla} \times \boldsymbol{\psi}$ is also a solution giving the same stray field. The inverse problem is therefore inherently ill-posed since no unique solution exists.

5.1.4. Source reconstruction of a flower state

As an example of the reconstruction of a magnetization state, the reconstruction of a magnetic flower state of a permanent magnetic unit cube is presented. This example was also presented in [57] and is here investigated in more detail.

The model used is shown in Figure 5.1. The magnetic unit cube ($1\times1\times1$ mm^3) defines the optimization domain Ω_{opt}. It is discretized by a tetrahedral mesh with 10 cells in each direction, therefore consisting of 6000 cells (1331 nodes). It is surrounded by six fieldboxes with a thickness of 0.04 mm covering the magnets whole surface at each side at a distance of 0.1 mm. The fieldboxes constite the domain Ω_{h} where the field is calculated. Each fieldbox consists of 600 cells (242 nodes).

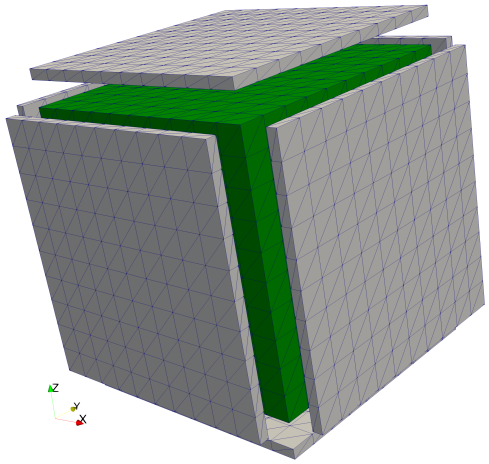

Figure 5.1.: Model used to calculate the forward stray field $\boldsymbol{H}_{\text{f}}$ used to reconstruct a magnetic flower state. The cube magnet (Ω_{opt}) is colored in green and the fieldboxes constituting the domain Ω_{h} are depicted in grey.

The magnetic flower state is described by

$$\boldsymbol{M}_{\text{f}} = M_{\text{s}} \begin{pmatrix} \sin(c_{\text{t}}\theta)\cos(\phi) \\ \sin(c_{\text{t}}\theta)\sin(\phi) \\ \cos(c_{\text{t}}\theta) \end{pmatrix} \quad \text{with} \quad \begin{matrix} \theta = z\sqrt{x^2+y^2} \\ \phi = \tan^{-1}(y/x) \end{matrix} \tag{5.13}$$

where c_{t} controls the amount by which the flower state is tilted and is chosen to be equal 2 in the presented examples. The saturation magnetization M_{s} is set to 1 A/m giving $|\boldsymbol{M}_{\text{f}}| = 1$ A/m.

In figure Figure 5.2 a slice through the middle of the model showing the magnetic flower state and the stray field $\boldsymbol{H}_{\text{f}}$, calculated as described in subsection 3.2.2, is presented. The field has a mean magnitude of 0.23 ± 0.04 A/m. Note, the magnetization is defined using piecewise linear basis functions ($\mathcal{P}_1$). The same is true for the potential u as well as the adjoint variable λ, while the derived stray field $\boldsymbol{H} = -\boldsymbol{\nabla} u$ is chosen to be constant within each element.

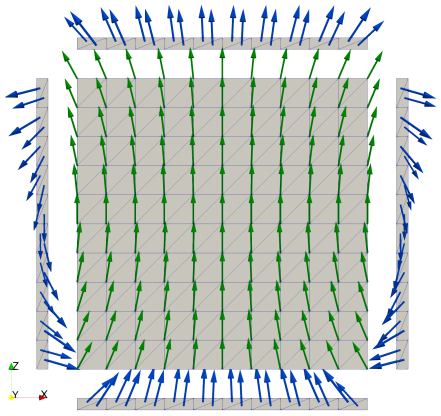

Figure 5.2.: Slice through the middle of the model showing the magnetic flower state (magnetization vectors in green) and the forward field (field vectors in blue).

The residual term as introduced in equation (5.1) used to perform the source reconstruction is given by

$$R(\boldsymbol{H}(\boldsymbol{M}) - \boldsymbol{H}_{\text{m}}) = \int_{\Omega_{\text{t}}} (\boldsymbol{H}(\boldsymbol{M}) - \boldsymbol{H}_{\text{m}})^2 \, \mathrm{d}V, \tag{5.14}$$

where $\Omega_{\text{t}} \subseteq \Omega_{\text{h}}$ is the target field domain defining the area from where the field is used as input for the source reconstruction.

In order to investigate the influence of regularization on the source reconstruction procedure, two different regularization terms are used. The regularization terms are given by

$$T_{\text{grad}}\left(\boldsymbol{M}\right) = \int_{\Omega_{\text{opt}}} \left(\boldsymbol{\nabla M}\right)^2 \, \mathrm{d}V \tag{5.15}$$

and

$$T_{\text{norm}}\left(\boldsymbol{M}\right) = \int_{\Omega_{\text{opt}}} \left(\boldsymbol{M}^2 - \boldsymbol{M}_{\text{r}}^2\right)^2 \, \mathrm{d}V. \tag{5.16}$$

The two regularization terms impact the magnetization differently. While $T_{\text{grad}}\left(\boldsymbol{M}\right)$ penalizes fluctuations within the magnetization and is considered to be a good regularization term since the magnetization is a slowly and smoothly varying entity, $T_{\text{norm}}\left(\boldsymbol{M}\right)$ penalizes magnetization vectors with a length different from the remanence magnetization $\boldsymbol{M}_{\text{r}}$. Note that in the presented case $\boldsymbol{M}_{\text{r}}$ has been replaced by 1 since this is the length of the individual magnetization vectors of the reference flower state $\boldsymbol{M}_{\text{f}}$. The influences of the two regularization terms are compared for the presented examples. Note, that in order to be able to calculate T_{grad}, the magnetization has to be defined using piecewise linear basis functions since it contains the gradient of the magnetization.

For the presented examples the Scipy implementation of the limited-memory Broyden–Fletcher-Goldfarb–Shanno minimization algorithm with bounds (L-BFGS-B) [41] is used to perform the optimizations and the derivative $\mathrm{d}\hat{J}$ is used as update during the optimization process. This was done since the possibility to use the derivative was easier to implement and done first. Furthermore, no big difference between the usage of the gradient and the derivative is expected since the mesh used is regular. However, it has to be pointed out, that since for the magnetization piecewise linear basis function are used, the dofs are on the nodes and therefore, the mass matrix is not diagonal, as is the case when using elements constant within each element, but has off-diagonal entries. Thus the multiplication is not a simple scaling of the dofs, but dofs on the boundary are weighted differently. However, after implementation of the necessary procedures, repeating selected optimizations using the python package moola [42] and the therein implemented L-BFGS minimization algorithm, no improvement of the optimization process was found.

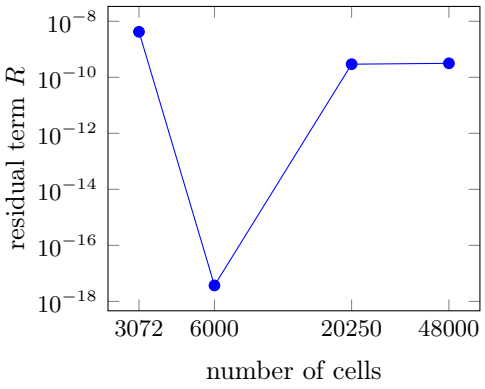

Figure 5.3.: Residual term R obtained from source reconstructions of the flower state without regularization and with the forward field $\boldsymbol{H}_{\text{f}}$ used as input directly, obtained for meshes with different numbers of cells.

The inverse crime

Note, that here the same algorithm is used to create the model problem that is then used to evaluate the capabilities of the inverse algorithm. This procedure can lead to the occurence of the so called inverse crime [62] and therefore has to be applied with caution. The main problem is, that the inverse algorithm, in this case inherently inverts the specific forward operator used to create the model problem. Therefore, its capabilities in reconstructing the model problem exceed

its capabilities of reconstructing sources using input data obtained in a different way. In order to illustrate this problem source reconstructions with the forward stray field $\boldsymbol{H}_\mathrm{f}$ as input have been performed for differently fine regular meshes for the magnetic unit cube, without any kind of regularization. In Figure 5.3 the residual terms of the source reconstructions are plotted in dependence of the number of cells of the unit cubes mesh. It can be seen that for the mesh with 6000 cells, that is identical to the mesh used to calculate the forward stray field, the reconstructed field coincides with the forward field orders of magnitudes better then when using a coarser or a finer mesh. In order to avoid these problems, for all presented examples, a different mesh, with the cell size halved in comparison to the mesh used for the generation of the model problem (48000 cells in total) is used. Furthermore, different levels of noise are added to the calculated forward field $\boldsymbol{H}_\mathrm{f}$. As noise, Gaussian noise with zero mean and different standard deviations of $10^{-2}, 10^{-3}, 10^{-4}$ and 10^{-5} is used. The influence of the different noise levels is investigated for each presented example.

Using 6 measurement boxes

As a first step all six boxes are used as target field domain $\Omega_\mathrm{t} = \Omega_\mathrm{h}$ for the source reconstruction.

L-curve method In order to find the optimal value of the regularization parameter α the L-curve method [63] is used. The objective functional is minimized for different values of the regularization parameter α starting with $\alpha = 0$ and increasing it by factors of 10 with $\alpha = 10^{-9}$ being the smallest value. In order to obtain an L-curve, the residual term R is plotted versus the regularization term T for different values of α in a log-log-plot. An example for the reconstruction of the flower state using 6 fieldboxes with a noise of 10^{-2} added to the forward field, a constant initial magnetization of $\boldsymbol{M}_\mathrm{init} = (0, 0, 0)$ and $T_\mathrm{grad}(\boldsymbol{M})$ used as regularization term is shown in Figure 5.4. For an regularization value of $\alpha = 0$ the magnetization tries to reproduce the noisy target field without any constraints, producing the smallest residual term. This is called over-

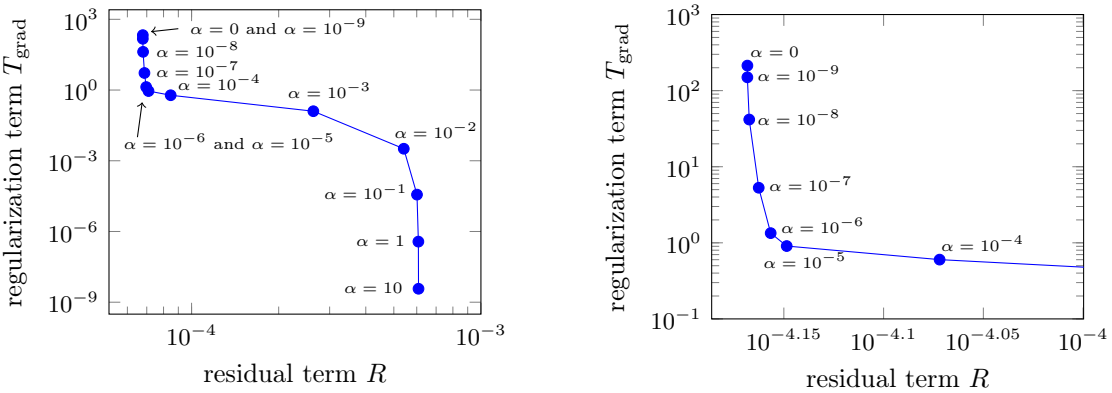

Figure 5.4.: L-curve for the source reconstruction of the flower state with 6 fieldboxes with a noise level of 10^{-2}, a constant initial magnetization of $\boldsymbol{M}_\mathrm{init} = (0, 0, 0)$ and $T_\mathrm{grad}(\boldsymbol{M})$ used as regularization term. The complete calculated L-curve is shown in (a) and in (b) the kink of the "L" is magnified.

fitting. An example can be seen in Figure 5.5 where the reconstructed magnetization state of a source reconstruction with $\boldsymbol{M}_{\text{init}} = (0, 0, 0)$ towards a target field with noise level 10^{-2} without regularization is shown. The strongly fluctuating magnetization vectors illustrate the over-fitting. Increasing the regularization parameter, the residual term increases only slightly while the regularization term decreases quickly. This happens up to a point where the regularization term becomes dominant and the residual term increases rapidly. This is where over-smoothing is happening. The ideal value of α is assumed to be right at the kink of the L-curve where the regularization is strong enough to regularize the magnetization, keeping it from over-fitting to the noise, but still weak enough to allow for the reconstruction of the flower state. Up to what value of α the L-curve is calculated depends, as will be seen on the level of noise as well as on the chosen regularization term. A condition for having used a large enough value of the regularization parameter is that the residual term increases significantly within the log-log-plot.

In order to find the optimal value for α as suggested in [63], after the objective functional has been minimized for some values of α, including values in the

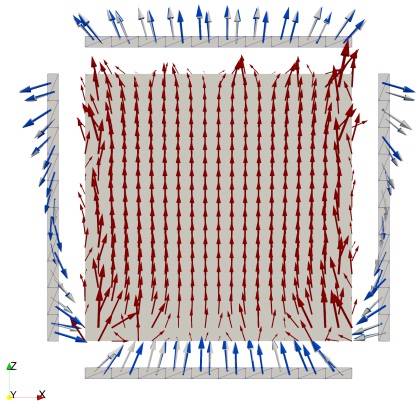

Figure 5.5.: Slice through the middle of the reconstructed flower state for a source reconstruction with noise level 10^{-2} and $\boldsymbol{M}_{\text{init}} = (0, 0, 0)$ without regularization. The field vectors of the noisy target field are represent in blue and the field vectors produced by the reconstructed magnetization in grey. The strongly fluctuating magnetization (red arrows) show that over-fitting occurs without regularization.

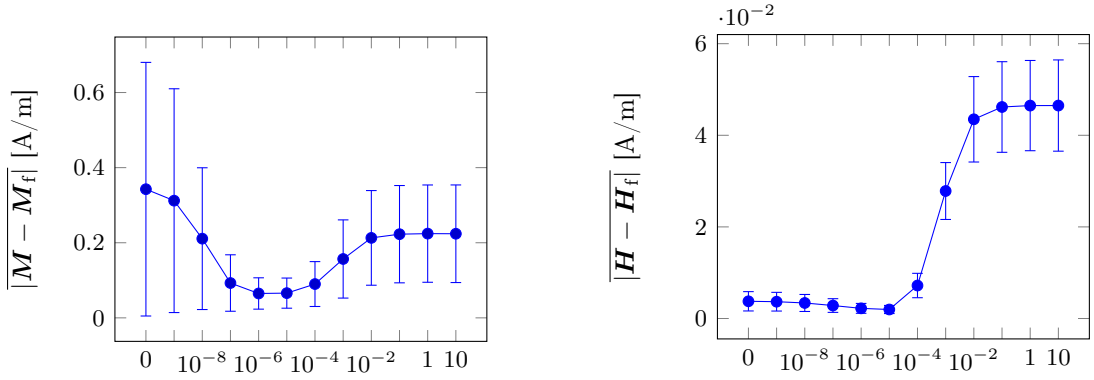

Figure 5.6.: Mean difference and standard deviation of (a) the magnetization at each dof between the obtained magnetization state and the reference flower state $\overline{|\boldsymbol{M} - \boldsymbol{M}_{\text{f}}|}$ and (b) the mean difference of the magnetic field at each dof between the obtained field and the reference forward field $\boldsymbol{H}_{\text{f}}$ for different values of α of the source reconstruction with a noise level of 10^{-2}, a constant initial magnetization of $\boldsymbol{M}_{\text{init}} = (0, 0, 0)$ and $T_{\text{grad}}(\boldsymbol{M})$ used as regularization term.

region of over-fitting, some kind of fitting procedure can be used to extract the optimal value of the regularization parameter. However, this is not done here but the L-curves obtained as explained above are evaluated manually. As can be seen from Figure 5.4 this procedure makes the exact choice of the value for α a bit ambiguous. Either, $\alpha = 10^{-6}$ and $\alpha = 10^{-5}$ seem reasonable choices. In order to investigate for which value of α really the best reconstruction of the magnetization occurs, for each α the resulting magnetization state $\boldsymbol{M}$ is compared to the flower state $\boldsymbol{M}_\mathrm{f}$. To do so, the flower state is interpolated onto the used mesh and the difference between the magnetization vectors at each dof, $|\boldsymbol{M} - \boldsymbol{M}_\mathrm{f}|$ is calculated. The same is done for the dofs of the magnetic field $\boldsymbol{H}$ obtained for each α and the noise free forward field $\boldsymbol{H}_\mathrm{f}$, giving $|\boldsymbol{H} - \boldsymbol{H}_\mathrm{f}|$. In Figure 5.6 the mean difference of the magnetization $\overline{|\boldsymbol{M} - \boldsymbol{M}_\mathrm{f}|}$ and the magnetic field $\overline{|\boldsymbol{H} - \boldsymbol{H}_\mathrm{f}|}$ is plotted in dependence of the regularization parameter α. The huge standard deviation of the magnetization for low α values shows that the magnetization fluctuates strongly for too small values of the regularization parameter. For $\alpha = 10^{-6}$ a minimum of the magnetization of $\overline{|\boldsymbol{M} - \boldsymbol{M}_\mathrm{f}|} = 64.92 \pm 41.47$ mA/m is found and in terms of reconstruction of the forward field a minimum is found at $\alpha = 10^{-5}$ with 1.97 ± 0.88 mA/m. The differences to the other possible best value of α (10^{-6} and 10^{-5} respectively) is an increase in 1.45% in $\overline{|\boldsymbol{M} - \boldsymbol{M}_\mathrm{f}|}$ and of 12.70% in $\overline{|\boldsymbol{H} - \boldsymbol{H}_\mathrm{f}|}$. Since the goal here is the source reconstruction of the magnetic flower state, in this case $\alpha = 10^{-6}$ is advantageous. Note, that this ambiguity arises frequently when evaluating the L-curve and it can be expressed as the choice between two values of the regularization parameter where one is still in the domain where the regularization parameter decreases without decreasing the residual term significantly ($\alpha = 10^{-6}$ in the above evaluation) and the other is the first value where the regularization has started to influence the solution and the decrease in the residual term is noticeable on the log-log-plot ($\alpha = 10^{-5}$ above). However, even though attempts were made, no clear trend favoring either of the two choices valid for all presented examples was found. Therefore, in order to be consistent, in the following, if this unambiguity arises, always the point still in the domain where the residual term has not yet decreased significantly is chosen.

The form or the L-curve changes for different noise levels and different regularization terms. This is exemplarily visualized in Figure 5.7 where the L-curves for different noise levels, including the case without noise, are plotted for a constant initial magnetization of $\boldsymbol{M}_\mathrm{init} = (0, 0, 0)$ and T_grad. It can be seen that with increasing noise the target field $\boldsymbol{H}_\mathrm{m}$ is reproduced with less accuracy. Furthermore, with increasing noise the domain in which over-fitting happens is longer and the kink in the L-curve is found for higher values of α. This shows, that for higher noise levels, over-fitting is a larger issue and the regularization has to be increased in order to smooth out the effects of the noise. Additionally, with increasing noise the kink in the L-curve becomes less pronounced. This also means that the ambiguity in the choice of the regularization parameter, as discussed above, increases with increasing noise. For comparison in Figure 5.8 two L-curves for which the choice of the optimal regu-

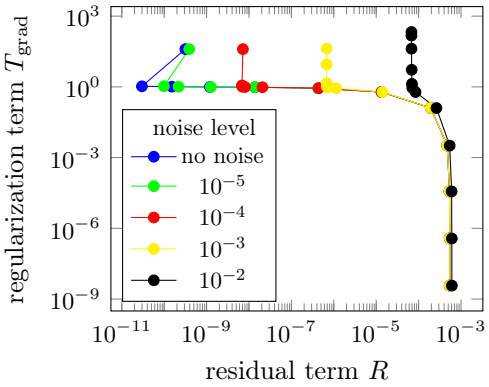

Figure 5.7.: L-curves for the source reconstruction with an initial magnetization $\boldsymbol{M}_\mathrm{init} = (0, 0, 0)$ and $T_\mathrm{grad}(\boldsymbol{M})$ as regularization term for target fields with different noise levels.

larization parameter value is unambiguous are plotted. Figure 5.8a shows the L-curve of the same optimization as above for a noise level of 10^{-5}. It is clearly visible that in this case the lowest residual term value is obtained not for $\alpha = 0$ but for $\alpha = 10^{-9}$. This suggests that without regularization the optimization terminates in a local minimum that is avoided using a small regularization parameter. $\alpha = 10^{-9}$ also constitutes the optimal value according to the L-curve evaluations and with a difference of $\overline{|\boldsymbol{H} - \boldsymbol{H}_\mathrm{f}|} = 10.70 \pm 5.70$ µA/m the forward field is reconstructed best for this parameter (see Figure 5.8c). However, while for $\alpha = 10^{-9}$ the difference in magnetization is given by $\overline{|\boldsymbol{M} - \boldsymbol{M}_\mathrm{f}|} = 70.24 \pm 37.52$ mA/m the magnetization is reconstructed more accurately for $\alpha = 10^{-7}$ with $\overline{|\boldsymbol{M} - \boldsymbol{M}_\mathrm{f}|} = 55.19 \pm 32.35$ mA/m (see Figure 5.8b). Furthermore, in Figure 5.8d the L-curve of the optimization towards the same target field with a noise level of 10^{-5} also with a constant initial magnetization of $\boldsymbol{M}_\mathrm{init} = (0, 0, 0)$ but with T_norm as regularization term is plotted. In comparison to T_grad, using T_norm the optimal regularization parameter according to the L-curve method is found for a much higher value of $\alpha = 10^{-2}$. In fact, up to $\alpha = 10^{-7}$ almost no change in the obtained magnetization is found as visible in Figure 5.8e. As can be seen in Figure 5.8f the forward field is reproduced best for the optimal value of α found using the L-curve method with $\overline{|\boldsymbol{H} - \boldsymbol{H}_\mathrm{f}|} = 12.61 \pm 8.44$ µA/m. However, again the magnetization reconstructing the flower state best is not found for the same α where $\overline{|\boldsymbol{M} - \boldsymbol{M}_\mathrm{f}|} = 70.83 \pm 38.99$mA/m, but for $\alpha = 10^{-5}$ with $\overline{|\boldsymbol{M} - \boldsymbol{M}_\mathrm{f}|} = 26.17 \pm 32.49$ mA/m. In both cases the best possible magnetization reconstructing the flower state is not found using the L-curve method for evaluation. This clearly shows the limitations of the L-curve method.

The computational effort necessary to obtain the optimal value of the regularization parameter α, depends on the one hand on the number of values of the regularization parameter for which the objective functional has to be minimized before the optimal value is found and on the other hand on the number of necessary function evaluations the individual minimizations need. The number of necessary function evaluations n_fev for each minimization of the objective functional, in dependence of the regularization parameter α, is plotted in Figure 5.9 for the examples discussed so far. Using the algorithm defined above to obtain the best value of the regularization parameter, this translates into a total number of necessary function evaluations of 2641 for the source reconstruction with $\boldsymbol{M}_\mathrm{init} = (0, 0, 0)$, T_grad and a noise level of 10^{-2}, since the L-curve has to be calculated up to at least $\alpha = 10^{-3}$ in order to be sure that the region of over-smoothing has been reached. For the optimization with $\boldsymbol{M}_\mathrm{init} = (0, 0, 0)$, T_grad and a noise level of 10^{-5}, 2925 function evaluations were necessary to calculate up to $\alpha = 10^{-7}$ and with T_norm, $n_\mathrm{fev} = 14785$ with a maximal α of 1.

Statistical evaluation In order to obtain statistically more significant results, for the presented examples, if not stated otherwise, for each noise level three different target fields were created using different random seeds. For each target field the L-curves are evaluated to extract the optimal value of the regularization parameter α. In order to compare the quality of the solutions obtained using the L-curve method with the overall possible best solutions, for each source reconstruction performed with a different value of the regularization parameter α the mean difference of the magnetization $\overline{|\boldsymbol{M} - \boldsymbol{M}_\mathrm{f}|}$ and of the magnetic field $\overline{|\boldsymbol{H} - \boldsymbol{H}_\mathrm{f}|}$ was calculated. The best possible solutions are defined as the solutions having the smallest $\overline{|\boldsymbol{M} - \boldsymbol{M}_\mathrm{f}|}$ and $\overline{|\boldsymbol{H} - \boldsymbol{H}_\mathrm{f}|}$ respectively. Note that in general the values of α at which the best solutions with respect to $\overline{|\boldsymbol{M} - \boldsymbol{M}_\mathrm{f}|}$ and $\overline{|\boldsymbol{H} - \boldsymbol{H}_\mathrm{f}|}$ are found do not coincide with each other. For each noise level, for a given initial magnetization $\boldsymbol{M}_\mathrm{init}$ and regularization term T the mean $\overline{|\boldsymbol{M} - \boldsymbol{M}_\mathrm{f}|}$ (mean$\overline{|\boldsymbol{M} - \boldsymbol{M}_\mathrm{f}|}$) and the mean

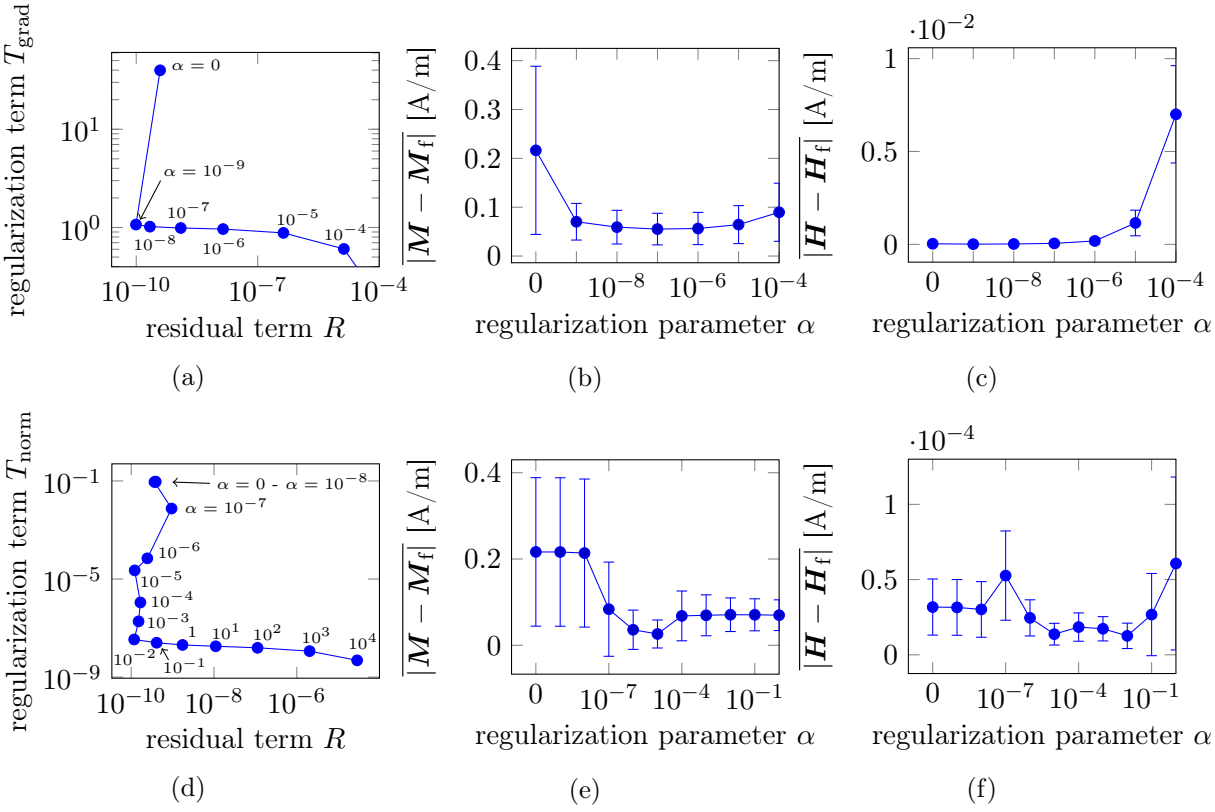

Figure 5.8.: L-curves for the source reconstructions for a noise level of 10^{-5} and $\boldsymbol{M}_{\text{init}} = (0, 0, 0)$ with (a) T_{grad} and (d) T_{norm} and corresponding $\overline{|\boldsymbol{M} - \boldsymbol{M}_{\text{f}}|}$ ((b) and (e)) and $\overline{|\boldsymbol{H} - \boldsymbol{H}_{\text{f}}|}$ ((c) and (f)).

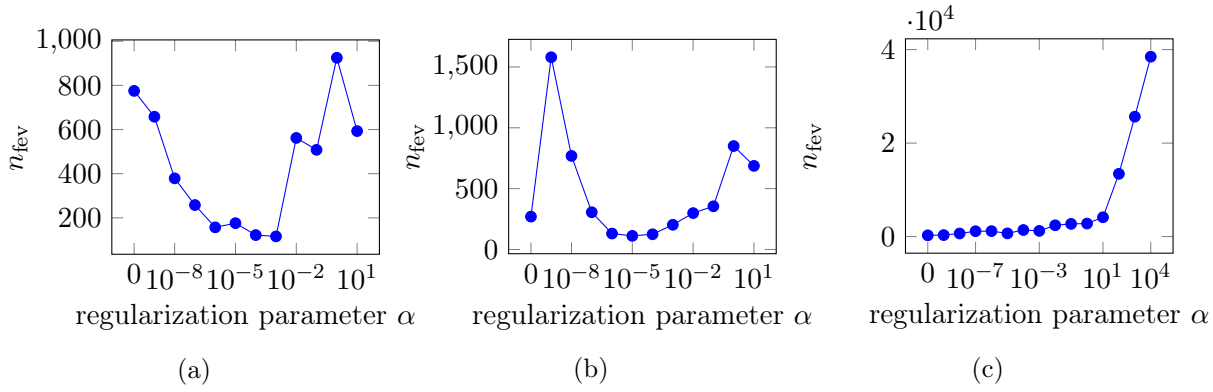

Figure 5.9.: Number of necessary function evaluations n_{fev} of the objective functional minimizations in dependence of the regularization parameter α for the source reconstructions with $\boldsymbol{M}_{\text{init}} = (0, 0, 0)$ with (a) a noise level of 10^{-2} and T_{grad}, (b) a noise level of 10^{-5} and T_{grad} and (c) a noise level of 10^{-5} and T_{norm}.

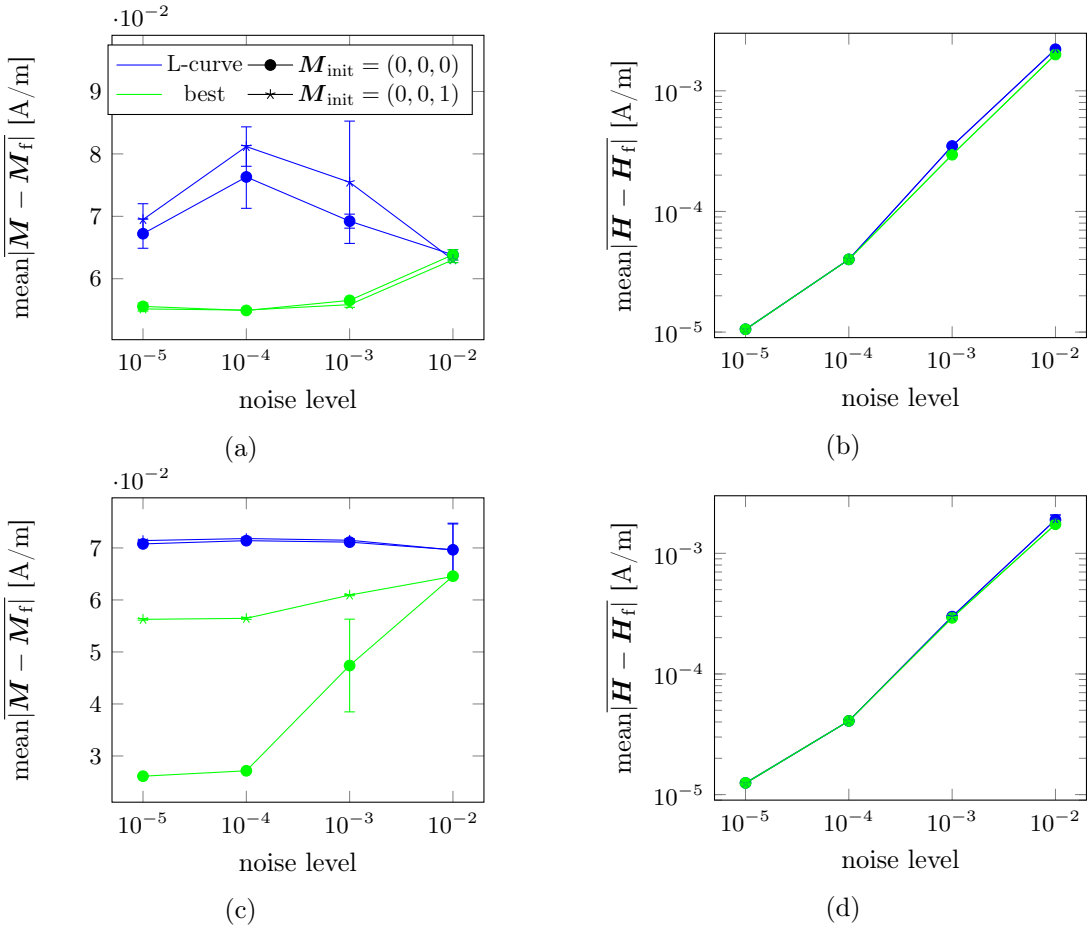

Figure 5.10.: Comparison of mean$\overline{|\boldsymbol{M}-\boldsymbol{M}_\mathrm{f}|}$ and mean$\overline{|\boldsymbol{H}-\boldsymbol{H}_\mathrm{f}|}$ obtained using the L-curve evaluation and the best found, for different initial distributions $\boldsymbol{M}_\mathrm{init}$, for source reconstructions of three target fields obtained with different random seeds for the noise, for the different regularization terms T_grad ((a) and (b)) and T_norm ((c) and (d)).

$\overline{|\boldsymbol{H}-\boldsymbol{H}_\mathrm{f}|}$ (mean$\overline{|\boldsymbol{H}-\boldsymbol{H}_\mathrm{f}|}$) over all three target fields are calculated for the solutions obtained using the L-curve method and the best possible solutions and the results are compared.

In Figure 5.10 the statistical evaluation for the source reconstruction of the magnetic flower state using 6 fieldboxes as input is shown. Regarding the quality of the reproduced magnetization state, the solutions found using the L-curve method and the best possible solutions differ significantly. Only for a noise level of 10^{-2} using T_grad the L-curve evaluation delivers the best possible solutions. For the regularization term T_norm for low noise levels a large difference between the best possible solution and the solution obtained using the L-curve method can be seen. Investigating the respective L-curves in more detail, it can be seen that in this cases the L-curves show an additional kink as also presented in Figure 5.8d and the best possible magnetization state is found at this kink for lower values of α. For a higher noise level of 10^{-3} the kink is already no longer visible and the difference between the best possible solution and the solution found using the L-curve method decreases. In Figure 5.11 the quality of the reconstructed flower state obtained using the L-curve method for different regularization terms and initial magnetizations is compared. It can be seen that the quality of the solutions obtained using T_grad fluctuates

in dependence of the noise level and also the standard deviation of mean$\overline{|\boldsymbol{M}-\boldsymbol{M}_\mathrm{f}|}$ is larger for noise levels below 10^{-2} compared to the solutions obtained using T_norm. Note that overall $\boldsymbol{M}_\mathrm{init} = (0,0,0)$ delivers better results for both regularization terms. Interestingly, increasing noise does not lead to a reduction in the quality of the reconstructed flower state, but the best reconstruction of the flower state using the L-curve method is found for a noise level of 10^{-2} with T_grad and $\boldsymbol{M}_\mathrm{init} = (0,0,1)$ with $\overline{|\boldsymbol{M}-\boldsymbol{M}_\mathrm{f}|} = 62.68 \pm 42.23$ mA/m. However, the best possible reconstruction that could be obtained if the optimal regularization parameter were accessible is found for T_norm with $\boldsymbol{M}_\mathrm{init} = (0,0,0)$ for a noise level of 10^{-5} having $\overline{|\boldsymbol{M}-\boldsymbol{M}_\mathrm{f}|} = 25.94 \pm 32.34$ mA/m. Both reconstructed magnetization states are shown in Figure 5.12 where they are also compared to the interpolated reference flower state.

Regarding the reconstruction of the forward field it can be seen, that the results obtained using the L-curve method and the best possible results coincide with each other to a higher degree than found for the reproduced magnetization state. Furthermore, the mean field difference mean$\overline{|\boldsymbol{H}-\boldsymbol{H}_\mathrm{f}|}$ increases almost logarithmically in the same ways as the noise does. This suggests that the introduced noise can not be smoothed out perfectly by the regularization. Note that, with the noise free forward field having a mean magnitude of 0.23 ± 0.04 A/m, mean$\overline{|\boldsymbol{H}-\boldsymbol{H}_\mathrm{f}|}$ in the order of 10^{-3} relates to a relative error in the forward field of around 0.5%. Furthermore note that, for both regularization terms the quality of the reproduced field is independent of the initial magnetization state and that the field reconstruction at low noise levels works slightly better using T_grad while for a noise level of 10^{-2} T_norm performs better.

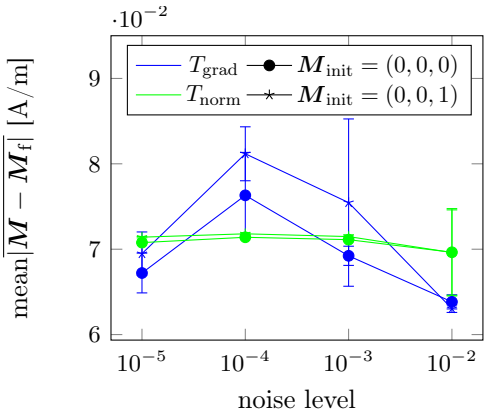

Figure 5.11.: Comparison of the quality of the reconstructed magnetic flower states (mean$\overline{|\boldsymbol{M}-\boldsymbol{M}_\mathrm{f}|}$) for the solutions obtained using the L-curve method in dependence of the noise level for different regularization terms and initial magnetizations.

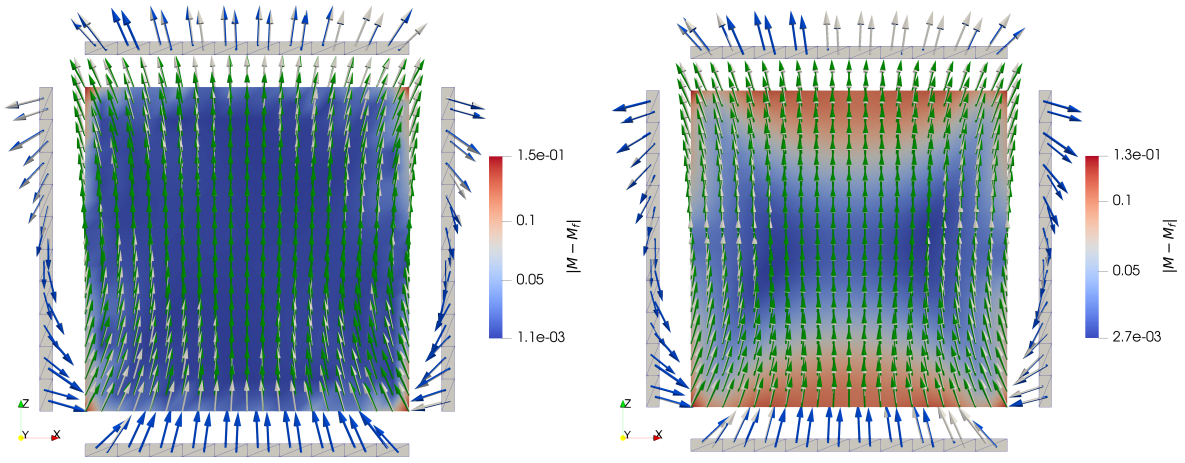

(a) (b)

Figure 5.12.: Slice through the middle of the reconstructed flower state for (a) the best possible solution and (b) the best solution obtained by evaluation using the L-curve method. The forward field vectors are depicted in blue and the magnetization vectors of the reference magnetic flower state in green. The color code represents the difference between the obtained magnetization $\boldsymbol{M}$ and the magnetization of the reference flower state $\boldsymbol{M}_{\mathrm{f}}$.

5.2. Using fictitious magnetic charges as sources

As discussed above (subsection 5.1.3) when using the magnetization as control variable, the source reconstruction problem has no unique solution and is therefore inherently ill-posed. This problems can be overcome by using fictitious magnetic charges as control variables. Fictitious magnetic charges, namely, the magnetic volume charge ρ_m and surface charges σ_m are defined by

$$\begin{aligned} \rho_\mathrm{m} &= -\boldsymbol{\nabla} \cdot \boldsymbol{M} \\ \sigma_\mathrm{m} &= \boldsymbol{n} \cdot \boldsymbol{M}. \end{aligned} \tag{5.17}$$

Simply substituting this definitions into the continuous forward problem as defined in equation (5.2) is not possible since neither the volume nor the surface charges appear explicitly. In order to solve equation (5.2) using fictitious magnetic charges, similarly to section 3.2, $\mathbb{R}^3$ is first split into a domain Ω_m containing all magnetic parts and a domain $\mathbb{R}^3/\Omega_\mathrm{m}$ (compare equations (3.28)-(3.32)). The volume charges can then be introduced obtaining

$$F\left(u\left(\rho_\mathrm{m},\sigma_\mathrm{m}\right),\rho_\mathrm{m},\sigma_\mathrm{m}\right) = \begin{cases} F^{\Omega_\mathrm{m}} = \Delta u + \rho_\mathrm{m} = 0, & \text{in} \quad \Omega_\mathrm{m} \\ F^{/\Omega_\mathrm{m}} = \Delta u = 0, & \text{in} \quad \mathbb{R}^3/\Omega_\mathrm{m} \end{cases} \tag{5.18}$$

with jump conditions

$$[u]_{\partial\Omega_\mathrm{m}} = 0, \tag{5.19}$$

$$\left[\frac{\partial u}{\partial \boldsymbol{n}}\right]_{\partial\Omega_\mathrm{m}} = -\sigma_\mathrm{m} \tag{5.20}$$

and open boundary condition

$$u\left(\boldsymbol{r}\right) \to \mathcal{O}\left(\frac{1}{|\boldsymbol{r}|}\right) \quad \text{for} \quad |\boldsymbol{r}| \to \infty. \tag{5.21}$$

Here again u, the state variable, is a scalar function from a Hilbert space U and in the same way ρ_m is a scalar function from an appropriate Hilbert space R. σ_m lives only on $\partial\Omega_\mathrm{m}$ and is also from an appropriate Hilbert space S and F is a mapping $U \times R \times S \to Z$ into another appropriate Hilbert space Z. Again the L^2-inner product is defined on all involved Hilbert spaces. Note, that in this form, there is a unique correspondence between the source term given by the magnetic volume charges ρ_m and the obtained scalar potential u and therefore the stray field. The inverse problem in this form therefore has a unique solution.

Since here, two function are used as design variable they can be represented as a vector

$$p = \begin{pmatrix} \rho_\mathrm{m} \\ \sigma_\mathrm{m} \end{pmatrix}. \tag{5.22}$$

Furthermore, since the magnetic surface charges σ_m are only present in the Neumann boundary condition they represent a boundary control variable and the optimization problem here is a simultaneous distributed-boundary optimal control problem with Neumann boundary control [64]. Note, that in contrast all other optimization problems discussed so far can be referred to as distributed optimal control problems [18].

Using fictitious magnetic charges, an additional advantage is found in the reduction of optimization variables. This is since the control variable is no longer a vector valued function with three variables at each dof, but the magnetic volume charges are a scalar function with therefore

only one variable at each dof and the surface charges are scalar as well living only at the surface of the magnetic structure. Depending of the exact shape of the investigated structure, the number of optimization variables is therefore reduced to almost a third, compared to using the magnetization as control variable.

The reduced optimization problem using fictitious magnetic charges can be written as

$$\min_{\rho_\mathrm{m},\sigma_\mathrm{m}\in R,S} \hat{J}\left(u\left(\rho_\mathrm{m},\sigma_\mathrm{m}\right),\rho_\mathrm{m},\sigma_\mathrm{m}\right). \tag{5.23}$$

5.2.1. Adjoint equation

In order to derive the adjoint equation, again ∂F_u^* is needed and in order to obtain it first ∂F_u is calculated from the Fréchet derivative defined in Definition 2. For $w \in U$ one obtains

$$\partial F_u\left(u\left(\rho_\mathrm{m},\sigma_\mathrm{m}\right),\rho_\mathrm{m},\sigma_\mathrm{m};w\right) = \partial F_u w = \lim_{\epsilon\to 0^+} \frac{F\left(u+\epsilon w,\rho_\mathrm{m},\sigma_\mathrm{m}\right) - F\left(u,\rho_\mathrm{m},\sigma_\mathrm{m}\right)}{\epsilon} = \Delta w, \tag{5.24}$$

the Laplace operator. Note that this is valid for F^{Ω_m} as well as $F^{/\Omega_\mathrm{m}}$. The dual operator ∂F_u^* is derived using Definition 4. Since u is continuous over the boundary $\partial\Omega_\mathrm{m}$ (equation (5.19)), if the same is demanded from an element $w \in U$ and also from the adjoint variable λ one can write

$$\begin{aligned}(\partial F_u w,\lambda) &= \int_{\mathbb{R}^3} \Delta w\,\lambda\,\mathrm{d}V \\ &= -\int_{\mathbb{R}^3} \boldsymbol{\nabla} w\cdot\boldsymbol{\nabla}\lambda\,\mathrm{d}V + \int_{\partial\Omega_\mathrm{m}^-} \boldsymbol{\nabla} w\cdot\boldsymbol{n}\,v\,\mathrm{d}s - \int_{\partial\Omega_\mathrm{m}^+} \boldsymbol{\nabla} w\cdot\boldsymbol{n}\,v\,\mathrm{d}s.\end{aligned} \tag{5.25}$$

Here, in order to consider the boundary conditions the surface integral was split into two boundary integrals over $\partial\Omega_\mathrm{m}$, where $\int_{\partial\Omega_\mathrm{m}^-}\mathrm{d}s$ defines an integration over the boundary $\partial\Omega_\mathrm{m}$ from the inside and $\int_{\partial\Omega_\mathrm{m}^+}\mathrm{d}s$ and integration over $\partial\Omega_\mathrm{m}$ from the outside, and an external boundary integral that vanishes if the open boundary condition on u (equation (5.21)) is also demanded for w. Note, that the two boundary integrals over $\partial\Omega_\mathrm{m}$ have different signs due to the direction of $\boldsymbol{n}$ and therefore, since boundary condition (5.20) is valid independent of the side from which the integration over the boundary is performed the two terms cancel and by again applying partial integration it follows

$$\begin{aligned}(\partial F_u w,\lambda) &= -\int_{\mathbb{R}^3} \boldsymbol{\nabla} w\cdot\boldsymbol{\nabla}\lambda\,\mathrm{d}V \\ &= \int_{\mathbb{R}^3} w\Delta\lambda\,\mathrm{d}V - \int_{\partial\Omega_\mathrm{m}^-} w\boldsymbol{\nabla} v\cdot\boldsymbol{n}\,\mathrm{d}s + \int_{\partial\Omega_\mathrm{m}^+} w\boldsymbol{\nabla} v\cdot\boldsymbol{n}\,\mathrm{d}s.\end{aligned} \tag{5.26}$$

Again, the exterior boundary terms vanish if open boundary conditions are demanded also from λ. Furthermore, the interior boundary terms here vanish if the simplest jump condition for λ, that is $\left[\frac{\partial\lambda(\boldsymbol{r})}{\partial\boldsymbol{n}}\right]_{\partial\Omega_\mathrm{m}} = 0$, is applied. One can therefore conclude

$$(\partial F_u w,\lambda) = \int_{\mathbb{R}^3} w\Delta\lambda\,\mathrm{d}V = (w,\partial F_u^*\lambda) \tag{5.27}$$

and the adjoint equation becomes

$$\boldsymbol{\nabla}\cdot\left(\boldsymbol{\nabla}\lambda - \mathcal{R}\left(\partial J_{\boldsymbol{H}}\right)\right) = 0 \tag{5.28}$$

in the same way as above (section 5.1) with open boundary condition

$$\lambda(\boldsymbol{r}) \to \mathcal{O}\left(\frac{1}{|\boldsymbol{r}|}\right) \quad \text{for} \quad |\boldsymbol{r}| \to \infty. \tag{5.29}$$

5.2.2. Gradient

Since when using fictitious magnetic charges the control variable is given by a vector (equation (5.22)), this is also true for the gradient

$$\nabla \hat{J}_p = \begin{pmatrix} \nabla \hat{J}_{\rho_\mathrm{m}} \\ \nabla \hat{J}_{\sigma_\mathrm{m}} \end{pmatrix} \tag{5.30}$$

and it is necessary to derive $\nabla \hat{J}_{\rho_\mathrm{m}}$ and $\nabla \hat{J}_{\sigma_\mathrm{m}}$ separately.

The gradient with respect to the volume charges $\nabla \hat{J}_{\rho_\mathrm{m}}$ can be obtained as before for an $r \in R$ by

$$\partial F_{\rho_\mathrm{m}} \left(u \left(\rho_\mathrm{m}, \sigma_\mathrm{m} \right), \rho_\mathrm{m}, \sigma_\mathrm{m}; r \right) = \partial F_{\rho_\mathrm{m}} r = \lim_{\epsilon \to 0^+} \frac{F \left(u \left(\rho_\mathrm{m}, \sigma_\mathrm{m} \right), \rho_\mathrm{m} + \epsilon r, \sigma_\mathrm{m} \right) - F \left(u, \rho_\mathrm{m}, \sigma_\mathrm{m} \right)}{\epsilon} = r \tag{5.31}$$

giving simply

$$\nabla \hat{J}_{\rho_\mathrm{m}} = -\lambda + \mathcal{R} \left(\partial J_{\rho_\mathrm{m}} \right). \tag{5.32}$$

In order to obtain the gradient with respect to the surface charges $\nabla \hat{J}_{\sigma_\mathrm{m}}$ the weak form of the forward problem has to be considered, since in the strong form σ_m does not appear explicitly. Furthermore, since $\nabla \hat{J}_{\sigma_\mathrm{m}}$ is only needed on Ω_m, only F^{Ω_m} is considered giving

$$-\int_{\Omega_\mathrm{m}} \boldsymbol{\nabla} u \cdot \boldsymbol{\nabla} v \, \mathrm{d}V + \int_{\partial \Omega_\mathrm{m}} \sigma_\mathrm{m} v \, \mathrm{d}s + \int_{\Omega_\mathrm{m}} \rho_\mathrm{m} v \, \mathrm{d}V = 0 \quad \text{on} \quad \Omega_\mathrm{m}, \tag{5.33}$$

where partial integration has been applied once. Note, that the transformation into the weak form also transforms the forward problem into the dual space $Z \to Z^*$. Following [18] this can be written in operator form as

$$-Au + B\sigma_\mathrm{m} + \rho_\mathrm{m} = 0. \tag{5.34}$$

Using this expression to obtain $\partial F_{\sigma_\mathrm{m}}$ via the Fréchet derivative, one obtains $\partial F_{\sigma_\mathrm{m}} = \mathrm{B}$, where B is a mapping $S \to Z^*$. However, since the gradient $\nabla \hat{J}_{\sigma_\mathrm{m}}$ is an element of the primal space of the surface charges S what is actually needed is B^*, a mapping $Z \to S$. Since the function space S contains only function that are defined on the boundary $\partial\Omega_\mathrm{m}$, B^* evaluates a function $z \in Z$ at the boundary $\partial\Omega_\mathrm{m}$, $B^* z = z|_{\partial\Omega_\mathrm{m}}$. The gradient therefore is given by

$$\nabla \hat{J}_{\sigma_\mathrm{m}} = -\lambda|_{\partial\Omega_\mathrm{m}} + \mathcal{R} \left(\partial J_{\sigma_\mathrm{m}} \right) \tag{5.35}$$

and for the complete gradient one gets

$$\nabla \hat{J} = \begin{pmatrix} \nabla \hat{J}_{\rho_\mathrm{m}} \\ \nabla \hat{J}_{\sigma_\mathrm{m}} \end{pmatrix} \begin{pmatrix} -\lambda + \mathcal{R} \left(\partial J_{\rho_\mathrm{m}} \right) \\ -\lambda|_{\partial\Omega_\mathrm{m}} + \mathcal{R} \left(\partial J_{\sigma_\mathrm{m}} \right) \end{pmatrix} \tag{5.36}$$

5.2.3. Obtaining a magnetization state from a charge state

In order to obtain a magnetization state from a fictitious magnetic charge distribution the defining equation (5.17) can be used. Since the obtained magnetization state should be irrotational, the magnetization is defined to be a gradient field

$$\boldsymbol{M} = \boldsymbol{\nabla} u_{\boldsymbol{M}} \tag{5.37}$$

where $u_{\boldsymbol{M}}$ is the respective scalar potential. The defining equation (5.17) then reads

$$\Delta u_{\boldsymbol{M}} + \rho_{\mathrm{m}} = 0, \quad \text{in} \quad \Omega_{\mathrm{m}}. \tag{5.38}$$

This however, is the same equation as obtained for $F^{\Omega_{\mathrm{m}}}$ (equation (5.18)) and therefore the magnetization can be obtained simply by calculating equation (5.37) with $u_{\boldsymbol{M}} = u$.

5.2.4. Source reconstruction of a flower state - continuation

Here, the magnetic flower state of a unit cube as presented above (subsection 5.1.4) has been reconstructed using fictitious magnetic charges as control variables. The residual term used is identical to the case where the magnetization was used as control variable (equation (5.14)) and the regularization term used is given by

$$T_{\text{charges}}\left(\rho_{\text{m}}, \sigma_{\text{m}}\right) = \int_{\Omega_{\text{opt}}} \rho_{\text{m}}^2 \, \mathrm{d}V + \int_{\Omega_{\text{opt}}} \sigma_{\text{m}}^2 \, \mathrm{d}V. \tag{5.39}$$

This regularization term includes a regularization on ρ_{m}, as well as a regularization on σ_{m}, and effectively limits the size of the magnetization vectors. Note, that even though the regularization term used consists of two terms, only one regularization parameter is used to perform Tikhonov regularization. This could be expanded by using a separate regularization parameter for each term. However, this would increase the computational effort severely and the optimal regularization parameters would have to be found on a two dimensional surface.

Note, that for all simulations the fictitious magnetic charges ρ_{m} and σ are defined using piecewise linear basis functions ($\mathcal{P}_1$).

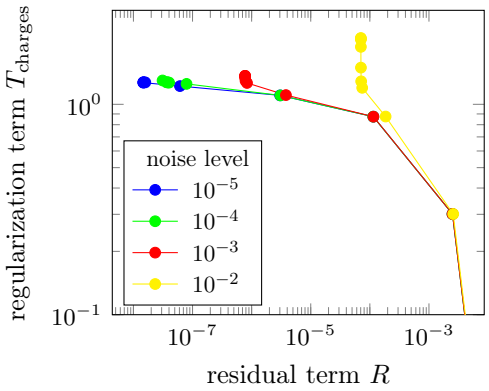

Figure 5.13.: L-curves for the source reconstruction using fictitious magnetic charges with $\rho_{\text{m,init}} = 0$ and $\sigma_{\text{m,init}} = 0$ for target fields with different noise levels.

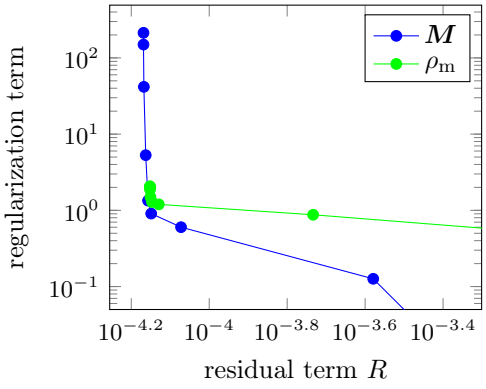

Figure 5.14.: Comparison of the L-curves obtained using the magnetization and fictitious magnetic charges as control variables for the source reconstruction with a noise level of 10^{-2} using T_{grad} and T_{charges} and an initial magnetization of $\boldsymbol{M}_{\text{init}} = (0, 0, 0)$ and $\rho_{\text{init}} = 0$, $\sigma_{\text{m,init}} = 0$ respectively.

Using 6 fieldboxes - fictitious magnetic charges

The source reconstruction using 6 fieldboxes has been repeated using fictitious magnetic charges. In order to provide a good comparison, the reconstruction was performed for each noise level for one target field identical to one target field used also for the case having the magnetization as control variable. In Figure 5.13 the obtained L-curves for an initial distribution of $\rho_{\text{m,init}} = 0$ and $\sigma_{\text{m,init}} = 0$ corresponding to $\boldsymbol{M}_{\text{init}} = (0, 0, 0)$ are shown. A comparison with the L-curves obtained using the magnetization as source with T_{grad} used as regularization term (Figure 5.7) shows that the target field is reconstructed significantly worse using fictitious magnetic charges. Only for a noise level of 10^{-2} the two methods deliver comparable results as shown in Figure 5.14 where the corresponding L-curves are compared. It can be seen, that the kink of the L-curve obtained using fictitious magnetic charges is much more pronounced as also reported in [58]. Regarding lower

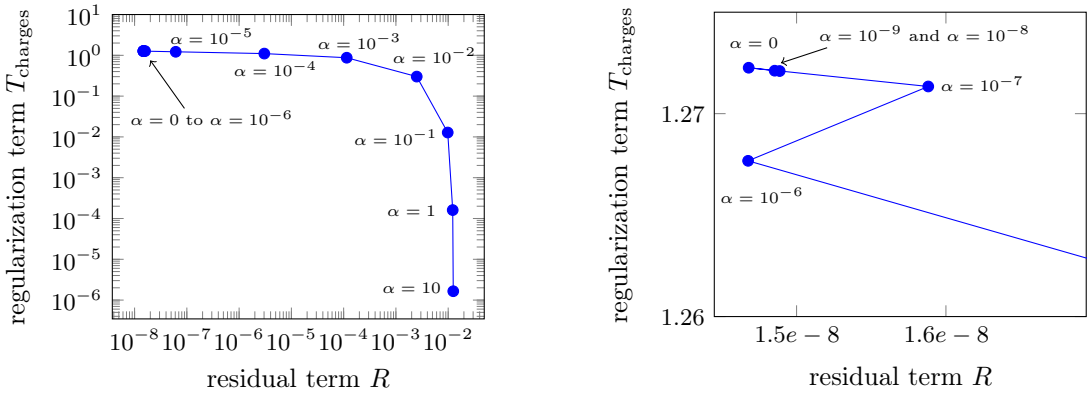

(a) (b)

Figure 5.15.: L-curve for the source reconstruction of the flower state with 6 fieldboxes with a noise level of 10^{-5}, an initial distribution of $\rho_{\text{init}} = 0$, $\sigma_{\text{m,init}} = 0$. The complete calculated L-curve is shown in (a) and in (b) the beginning of the curve is magnified.

noise levels, it is visible, that the domain where over-fitting occurs is less extended compared to the reconstructions using the magnetization. Furthermore, for lower noise levels and small values of the regularization parameter no vertical line of the L-curve can be seen, but the residual term fluctuates with increasing α. This is visualized in Figure 5.15 where the L-curve for the source reconstruction with $\rho_{\text{m,init}} = 0$ and $\sigma_{\text{m,init}} = 0$ for a noise level of 10^{-5} is shown. However, the evaluation following the L-curve method can still be performed delivering an optimal value of $\alpha = 10^{-6}$ in this case. Regarding reconstruction of the forward field, the minimal $\overline{|\boldsymbol{H} - \boldsymbol{H}_{\text{f}}|}$ of 175.40 ± 174.02 µA/m is found at the optimal α value while $\overline{|\boldsymbol{M} - \boldsymbol{M}_{\text{f}}|}$ at the optimal alpha value is 130.90 ± 66.38 mA/m which is marginally worse compared to the best reconstruction of the magnetization at $\alpha = 10^{-7}$ with $\overline{|\boldsymbol{M} - \boldsymbol{M}_{\text{f}}|} = 130.86 \pm 66.39$ mA/m.

The initial magnetization state $\boldsymbol{M} = (0, 0, 1)$ can also be created using fictitious magnetic charges by setting all dofs of σ_{m} to 1 at the top of the magnetic cube and to -1 at the bottom and keeping

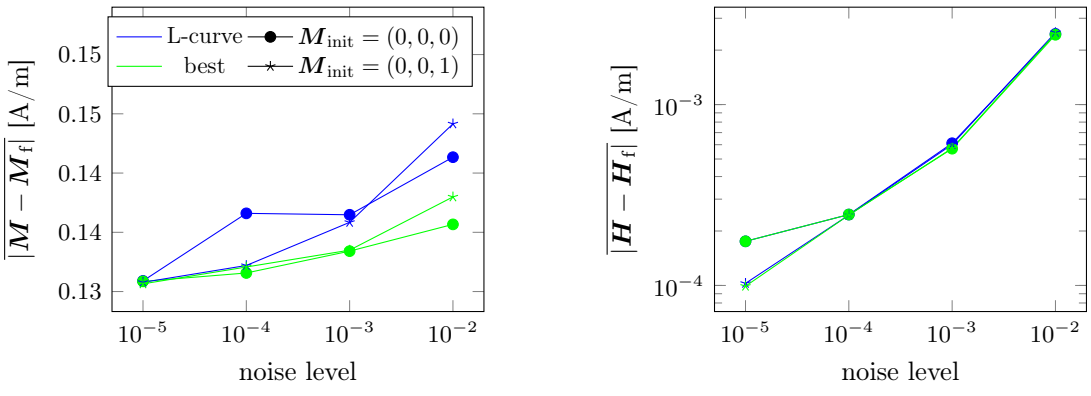

(a) (b)

Figure 5.16.: Comparison of $\overline{|\boldsymbol{M} - \boldsymbol{M}_{\text{f}}|}$ and $\overline{|\boldsymbol{H} - \boldsymbol{H}_{\text{f}}|}$ obtained using the L-curve evaluation and the best found for different initial distributions of $\rho_{\text{m,init}}$ and $\sigma_{\text{m,init}}$ representing $\boldsymbol{M}_{\text{init}} = (0, 0, 0)$ and $\boldsymbol{M}_{\text{init}} = (0, 0, 1)$ respectively.

$\rho_\mathrm{m} = 0$. This distribution is denoted as $\sigma_\mathrm{m,init} \approx \boldsymbol{M}_\mathrm{init} = (0, 0, 1)$. The source reconstructions using this initial distribution is compared to the reconstructions obtained using a zero initial distribution in Figure 5.16 where again $\overline{|\boldsymbol{M} - \boldsymbol{M}_\mathrm{f}|}$ and $\overline{|\boldsymbol{H} - \boldsymbol{H}_\mathrm{f}|}$ for the solutions obtained from the L-curve method and for the best possible solutions are plotted. Regarding the reconstruction of the magnetization state, it can be seen that while a zero initial distribution always finds an equal or better reconstruction of the flower state compared to the initial distribution representing $\boldsymbol{M}_\mathrm{init} = (0, 0, 1)$ in terms of overall best solution, when comparing the best solution found using the L-curve method no initial distribution is clearly favorable for all noise levels. For a noise level of 10^{-5} the optimal solution is found using the L-curve method and the difference between to the best possible solutions increases with increasing noise. This is in contrast to the case of using the magnetization as control variable where the difference decreased with increasing noise and using the L-curve method the optimal solution was found for a noise level of 10^{-2}. Note, that the mean increase in $\overline{|\boldsymbol{M} - \boldsymbol{M}_\mathrm{f}|}$ between the solutions found using the L-curve method and the best possible solutions here is $2.10 \pm 1.78\%$. Compared to the source reconstruction with the magnetization as control variable and T_grad using the same target field with magnetization where this mean increase is 26.25 ± 18.26, therefore the relative difference between the solutions obtained using the L-curve method and the best possible solutions is lower when using fictitious magnetic charges. However, as shown in Figure 5.17 where $\overline{|\boldsymbol{M} - \boldsymbol{M}_\mathrm{f}|}$ and $\overline{|\boldsymbol{H} - \boldsymbol{H}_\mathrm{f}|}$ obtained using fictitious magnetic charges and the magnetization as control variable using the L-curve evaluation are plotted for the different noise levels, using fictitious magnetic charges the obtained reconstruction of the reference flower state is significantly worse.

Regarding the reconstruction of the noise free magnetic field $\boldsymbol{H}_\mathrm{f}$ again an increase in $\overline{|\boldsymbol{H} - \boldsymbol{H}_\mathrm{f}|}$ with increasing noise can be observed with no initial distribution being advantageous over all noise levels. A comparison with the case of using the magnetization as control variable is shown in Figure 5.17b. It can be seen that the forward field is also reconstructed worse for all noise levels and initial distributions by the method using fictitious magnetic charges with the difference between the two methods decreasing with increasing noise. Note, that the fact that the difference in reconstruction of the noise free forward field between the two methods decreases with increasing noise but the difference in reconstruction of the reference magnetization state suggests, that

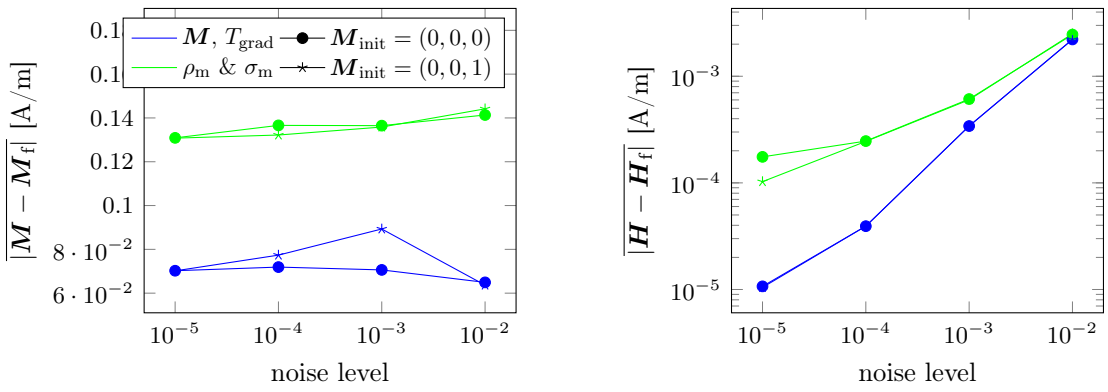

Figure 5.17.: Comparison of the quality of (a) the reconstructed magnetization states ($\overline{|\boldsymbol{M} - \boldsymbol{M}_\mathrm{f}|}$) and (b) the reconstructed noise free forward fields ($\overline{|\boldsymbol{H} - \boldsymbol{H}_\mathrm{f}|}$) obtained using the L-curve method for source reconstructions using fictitious magnetic charges and the magnetization as control variables.

the reason for the worse performance in reconstruction of the magnetization state when using fictitious magnetic charges is rooted in the numerics of the additional calculation step necessary to obtain a magnetization distribution from a fictitious charge distribution.

The comparison of the two methods shows, that the simplification of the minimization procedure by reducing the number of optimization variables through introduction of fictitious magnetic charges as control variables did not improve the results of the source reconstruction. This is also true regarding computational effort. Neither were the number of necessary function evaluations necessary to minimize the objective functional for an individual regularization parameter value reduced significantly nor was the number of α values calculated to obtain the L-curve smaller.

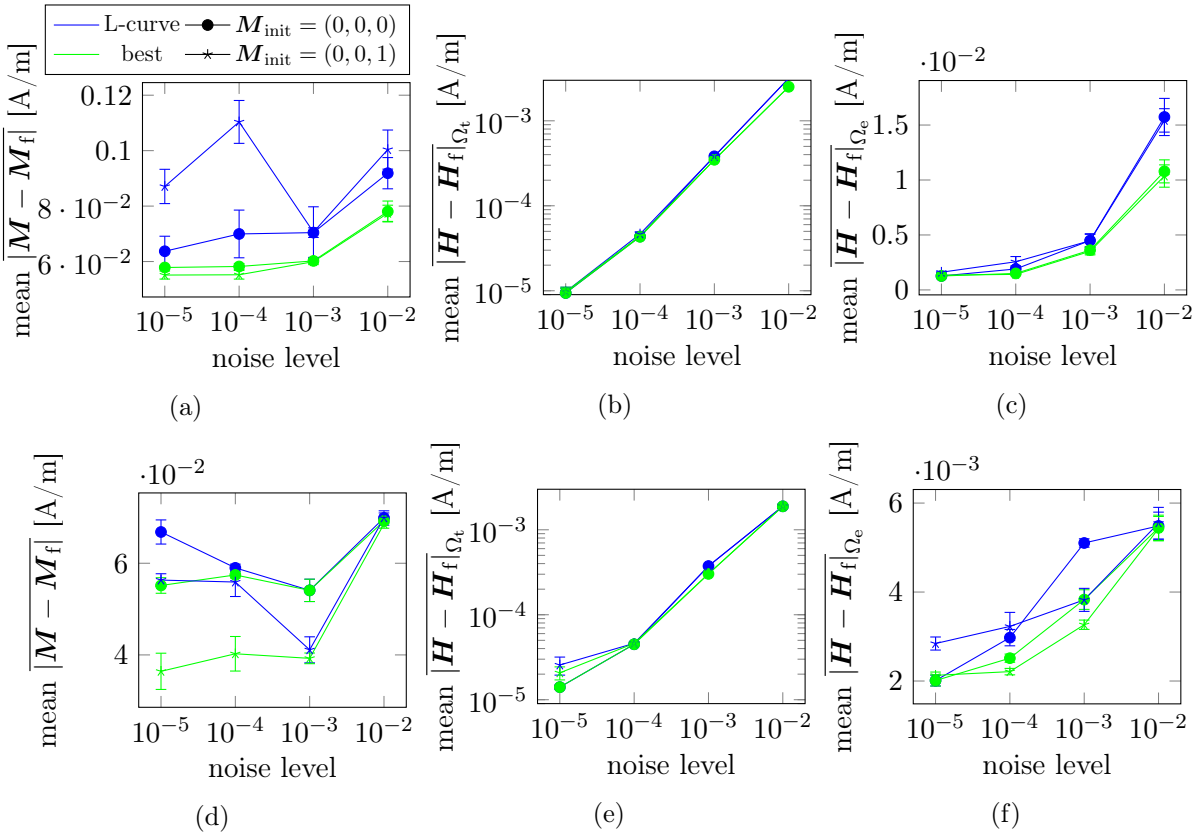

Figure 5.18.: Comparison of the mean $\overline{|\boldsymbol{M} - \boldsymbol{M}_{\text{f}}|}$ and mean $\overline{|\boldsymbol{H} - \boldsymbol{H}_{\text{f}}|}$ of source reconstructions with two field boxes as target domain Ω_{t}, of three target fields obtained with different random seeds for solutions obtained using the L-curve evaluation and the best possible solution for the different regularization terms T_{grad} ((a) and (b)) and T_{norm} ((c) and (d)).

Reducing the number of input fieldboxes

In practice obtaining information about the stray field of a magnetic structure at arbitrary points in space is often not possible since on the one hand the areas might simply not be non-destructively accessible or on the other hand performing measurements on several sides of a structure while keeping the positioning error low is rather involved. Since it is expected, that the quality of the reconstructed magnetization state highly depends on the position and the number of data points of the target field used as input for the inverse problem, as a next step the dependence on the number of input fieldboxes used is investigated. To do so, first the four fieldboxes at the sides of the magnetic unit cube (with respect to the z-axis) are removed from the target field domain Ω_t, leaving only the top and bottom fieldbox as input for the source reconstruction problem. Continuing, also the bottom fieldbox is removed leaving only the top fieldbox as input constituting Ω_t. Note that by reducing the number of fieldboxes and keeping the number of measurement points within each fieldbox constant also the number of input measurement points is reduced. The source reconstruction is performed using the magnetization as well as fictitious magnetic charges as control variables for the identical three target fields for each noise level as before. Again, the quality of the obtained magnetization state is investigated by using $\overline{|\boldsymbol{M}-\boldsymbol{M}_\mathrm{f}|}$. Inside Ω_t the reconstructed magnetic field is compared to the noise free forward field using $\overline{|\boldsymbol{H}-\boldsymbol{H}_\mathrm{f}|}_{\Omega_\mathrm{t}}$. Additionally, the possibility to reconstruct the magnetic field in areas that were not part of the input domain Ω_t, referred to as field extrapolation in the following, is investigated. To this aim, the field created by the reconstructed source is evaluated within the fieldboxes that are not part of the input for the source reconstruction $\Omega_\mathrm{e} = \Omega_\mathrm{h}/\Omega_\mathrm{t}$ and is compared to the forward field created by the reference flower state by $\overline{|\boldsymbol{H}-\boldsymbol{H}_\mathrm{f}|}_{\Omega_\mathrm{e}}$.

In Figure 5.18 the results for two fieldboxes constituting Ω_t, using the magnetization as control variable are presented. Regarding the reconstruction of the magnetic flower state, again a difference between the solutions found using the L-curve method and the best possible solutions can be seen. While using T_grad now also at a noise level of 10^{-2} the optimal solution is not found using the L-curve method, using T_norm the difference decreased significantly with respect to using 6 fieldboxes as input and already for a noise level of 10^{-3} the difference is very small. However, for lower noise levels using T_norm as regularization term, the difference between the best possible and solutions found using L-curve is again large and this is again due to the fact that the best solutions are found at the additional kink in the L-curve. Notice, that in comparison to the case of using 6 fieldboxes as input now the best solutions are found for $\boldsymbol{M}_\mathrm{init} = (0,0,1)$. In Figure 5.19 the solutions obtained using the L-curve method are compared for the different regularization terms and initial magnetizations. In comparison to the source reconstructions using 6 fieldboxes as input, here using T_norm is advantageous for all noise levels.

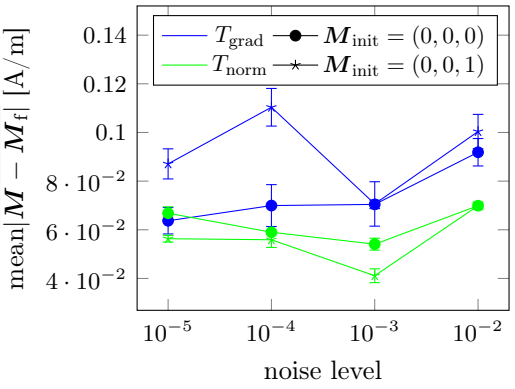

Figure 5.19.: Comparison of the quality of the reconstructed magnetic flower state mean$|\boldsymbol{M}-\boldsymbol{M}_\mathrm{f}|$ in dependence of the noise level for different regularization terms and initial magnetizations for source reconstructions with two fieldboxes as input.

Within the target domain Ω_t the noise free forward field is reconstructed equally well with respect to using 6 fieldboxes as input, and the same logarithmic increase in mean$|\overline{\boldsymbol{H} - \boldsymbol{H}_f}|_{\Omega_t}$ with increasing noise is observed.

Regarding the possibility to extrapolate the magnetic field in regions not part of the input domain Ω_t in Figure 5.18 it can be seen, that for the solutions obtained using the L-curve method as well as for the best possible solutions the difference between the extrapolated field and the forward field increases with increasing noise. Using T_{grad}, the difference in field extrapolation quality between the solutions obtained using the L-curve method and the best possible solutions increases with increasing noise. Note, that there is no one-to-one correspondence between the quality of the reconstructed of magnetization state and the quality of the extrapolated field. This can e.g. be seen for the source reconstruction using T_{norm} with a noise level of 10^{-5}. While the best possible magnetization reconstruction is obtained using $\boldsymbol{M}_{\text{init}} = (0, 0, 1)$, the best possible field extrapolation is found for $\boldsymbol{M}_{\text{init}} = (0, 0, 0)$ and the same is true for the solutions obtained using L-curve method. While regarding reconstruction of magnetization state $\boldsymbol{M}_{\text{init}} = (0, 0, 1)$ is advantageous, for the field extrapolation $\boldsymbol{M}_{\text{init}} = (0, 0, 0)$ is better. The best solutions obtained using the L-curve are compared in Figure 5.20. While for noise levels lower 10^{-2}, T_{grad} is advantageous, for a noise level of 10^{-2} the reconstructed magnetization state using T_{norm} extrapolates the field better. Note, that the dependence on $\boldsymbol{M}_{\text{init}}$ is negligible. Furthermore note, that using T_{norm} mean$|\overline{\boldsymbol{H} - \boldsymbol{H}_f}|$ is well below 10^{-2} for all noise levels. With a mean magnitude of the noise free forward field of 0.21 ± 0.03 A/m this relates to a relative error of the extrapolated forward field of around 5%.

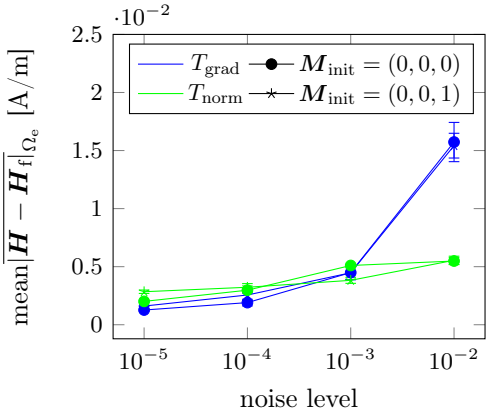

Figure 5.20.: Comparison of the quality of the field extrapolation mean$|\overline{\boldsymbol{H} - \boldsymbol{H}_f}|_{\Omega_e}$ in dependence of the noise level for different regularization terms and initial magnetizations for source reconstructions with two fieldboxes constituting Ω_t.

The source reconstruction with two fieldboxes constituting the input domain Ω_t has also been performed using fictitious magnetic charges as control variables for all three target fields. The results are shown in Figure 5.21. In comparison to using the magnetization as control variable it can be seen that neither regarding the reconstruction of the reference flower state nor regarding field extrapolation using fictitious magnetic charges is of advantage.

Reducing the amount of fieldboxes within the target domain Ω_t further to one, regarding the reconstruction of the reference flower state, the mentioned kinks in the L-curve present when using T_{norm} vanish and the solutions found using the L-curve method are much closer to the best possible solutions. Furthermore, having one fieldbox as input, the magnetization state obtained for reconstructions using T_{norm} are much closer to the reference flower state compared to magnetization state obtained using T_{grad} as shown in Figure 5.22 were the best solutions found using the L-curve method are compared. Note, that this is since T_{grad} in this cases prevents any tilting of the magnetization at the bottom of the magnetic unit cube as can be seen in Figure 5.23b

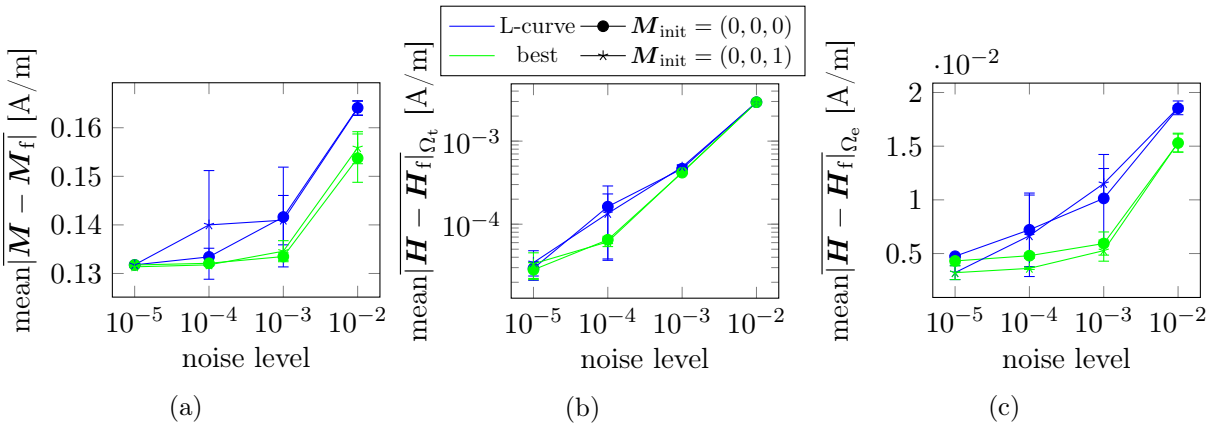

Figure 5.21.: Comparison of (a) mean$|\overline{\boldsymbol{M} - \boldsymbol{M}_{\text{f}}}|$, (b) mean$|\overline{\boldsymbol{H} - \boldsymbol{H}_{\text{f}}}|_{\Omega_{\text{t}}}$ and (c) mean$|\overline{\boldsymbol{H} - \boldsymbol{H}_{\text{f}}}|_{\Omega_{\text{e}}}$ for solutions obtained using the L-curve evaluation and the best possible solutions, for source reconstructions of three target fields obtained with different random seeds, using fictitious magnetic charges as control variables with different initial distributions representing $\boldsymbol{M}_{\text{init}} = (0,0,0)$ and $\boldsymbol{M}_{\text{init}} = (0,0,1)$, in dependence of the noise level.

were the reconstructed magnetization state obtained from the L-curve using $\boldsymbol{M}_{\text{init}} = (0,0,0)$ for a noise level of 10^{-3} is shown. In order to explain this, consider that the strength of a magnetic field decays with distance from its source. Therefore, the influence of the magnetization distribution on the residual term far away from the fieldbox at the bottom of the magnetic unit cube is very small compared to the area close to the fieldbox. However, the regularization enforces a penalization on the magnetization independent of its distance from the fieldbox. Therefore, when the regularization is of optimal strength in the sense that it regularizes the magnetization, but allows it to reconstruct the flower state in an area close to the fieldbox, for the area far away from the fieldbox it is to strong to allow for any tilting and therefore over-smooths in this area. Comparing the reconstructed magnetization states obtained from the L-curve using T_{norm} and T_{grad} for $\boldsymbol{M}_{\text{init}} = (0,0,0)$ and a noise level of 10^{-3}, as done in Figure 5.23, it can furthermore be seen, that in areas close to the fieldbox T_{grad} actually is advantageous giving the smaller $|\boldsymbol{M} - \boldsymbol{M}_{\text{f}}|$ while on the opposite site of the fieldbox T_{norm} only regularizing the length of the individual magnetization vectors stills allows for tilting of the magnetization towards the flower state. Note, that this fact is not visible in the above case using two field-

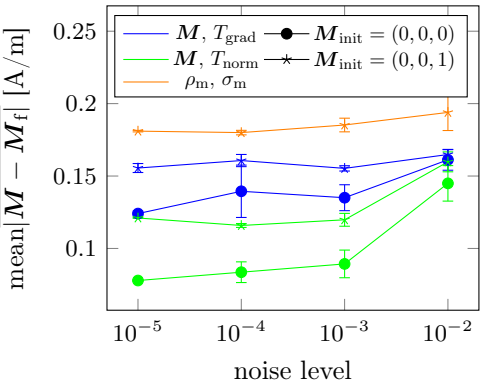

Figure 5.22.: Comparison of the quality of the reconstructed magnetic flower state mean$|\overline{\boldsymbol{M} - \boldsymbol{M}_{\text{f}}}|$ in dependence of the noise level for different regularization terms and initial magnetizations when using the magnetization $\boldsymbol{M}$ and fictitious magnetic charges ρ_{m}, σ_{m} as control variable for the source reconstruction performend with one fieldbox constituting the target field domain Ω_{t}.

boxes as target domain Ω_t since the two fieldboxes are placed close to areas where the tilting is largest. A way to possibly mitigate the problem of distance dependent regularization is to impose a distance dependence on the regularization in the same way as it is naturally present in the residual term.

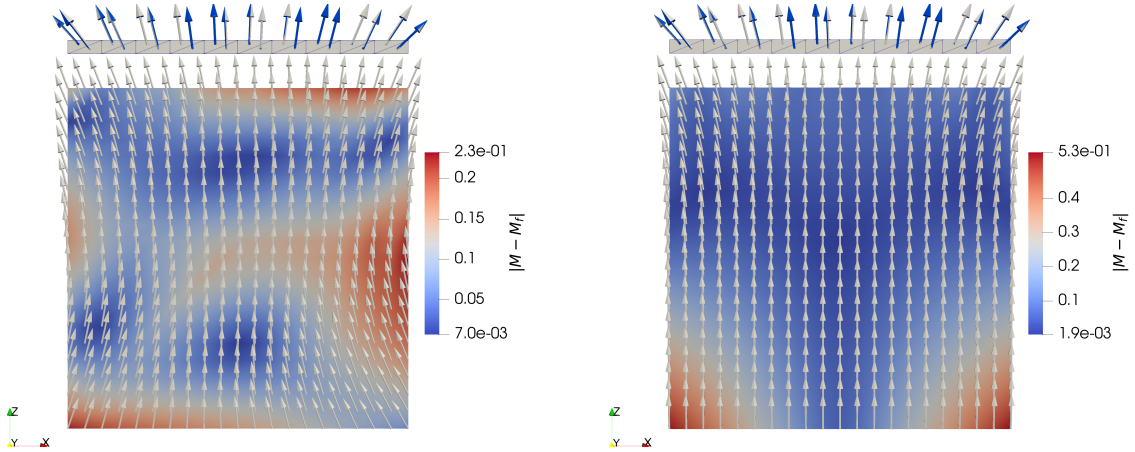

(a) (b)

Figure 5.23.: Slice through the middle of the reconstructed flower states obtained from the L-curves of source reconstructions with $\boldsymbol{M}_{\text{init}} = (0, 0, 0)$ and a noise level of 10^{-3} using (a) T_{norm} and (b) T_{grad}. The forward field vectors are depicted in blue. The color code represents the difference between the obtained magnetization $\boldsymbol{M}$ and the magnetization of the reference flower state $\boldsymbol{M}_{\text{f}}$.

In Figure 5.22 also the solutions obtained from source reconstructions using using fictitious magnetic charges as control variables are plotted. It can be seen that the obtained reconstructed magnetization states have a mean$|\boldsymbol{M} - \boldsymbol{M}_{\text{f}}|$ higher than all magnetization states reconstructed using the magnetization as control variable. Note, that the magnetization states obtained using $\rho_{\text{m,init}} = 0$ and $\sigma_{\text{m,init}} = 0$ having a larger mean$|\boldsymbol{M} - \boldsymbol{M}_{\text{f}}|$ on average over all noise levels by a factor of 2.78 ± 0.14 compared to an initial distribution of $\rho_{\text{m,init}} = 0$ and $\sigma_{\text{m,init}} \approx \boldsymbol{M}_{\text{init}} = (0, 0, 1)$ and are therefore not visible within the plot.

In Figure 5.24 the quality of the reconstructed magnetization states in terms of mean$|\boldsymbol{M} - \boldsymbol{M}_{\text{f}}|$ of solutions obtained using the L-curve method using the magnetization as control variable is plotted for each regularization term and initial magnetization in dependence of the number of fieldboxes used within Ω_t for each noise level separately. For all noise levels lower 10^{-2} the reconstructed magnetization state with the best quality is found using only two fieldboxes as input to the source reconstruction problem. Only for a noise level of 10^{-2} the quality of the reconstructed magnetization state reduces monotonically when reducing the number of fieldboxes used as input. Note, that the difference over all numbers of fieldboxes ia lowest using T_{norm} as regularization with an initial magnetization $\boldsymbol{M}_{\text{init}} = (0, 0, 0)$. Furthermore, it can be seen that for all noise levels when using one fieldbox the source reconstruction with T_{norm} and $\boldsymbol{M}_{\text{init}} = (0, 0, 0)$ delivers a magnetization state closest to the reference flower state. Note, that regarding the best possible solutions obtained for the regularization parameter value minimizing $|\boldsymbol{M} - \boldsymbol{M}_{\text{f}}|$, the decrease in quality of the reconstructed magnetization state is monotonous with decreasing number of fieldboxes except for a noise level of 10^{-3} where also regarding the best possible solutions the minimum in mean$|\boldsymbol{M} - \boldsymbol{M}_{\text{f}}|$ is found using two fieldboxes.

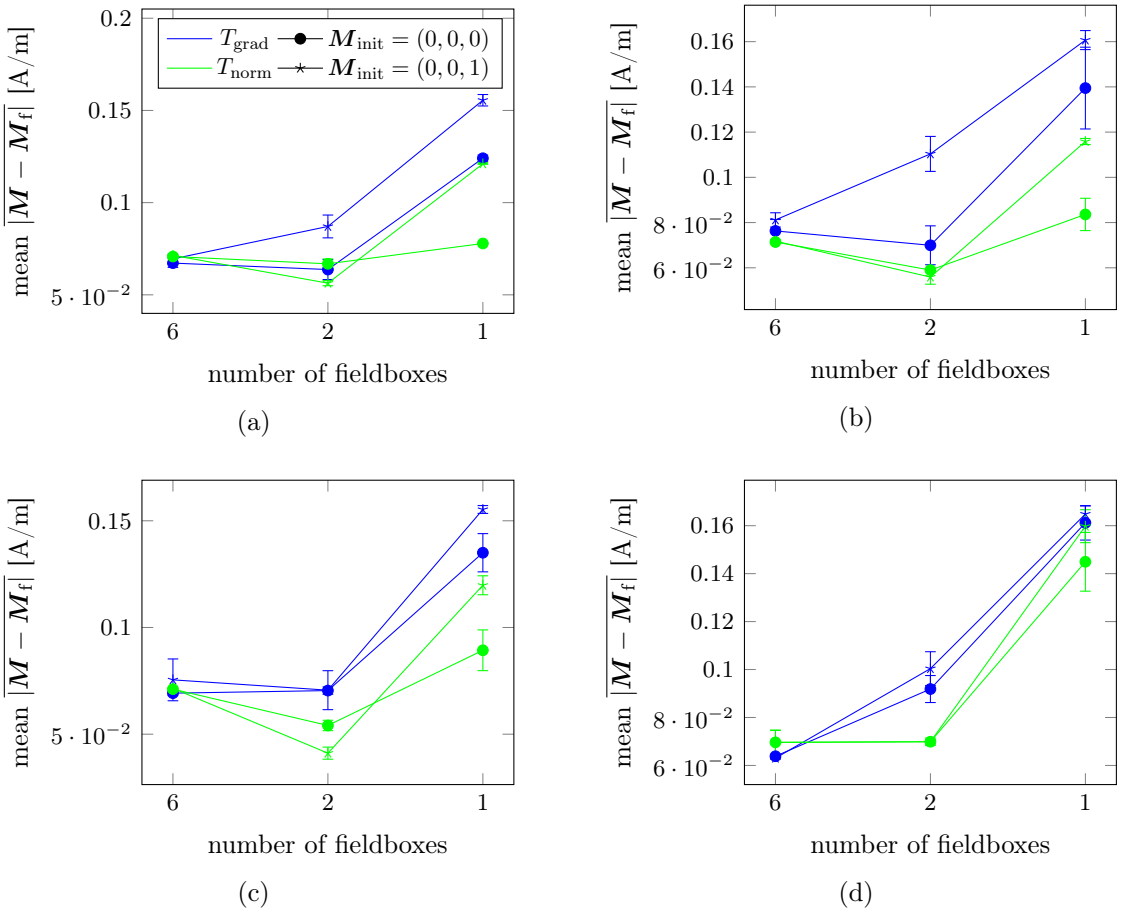

Figure 5.24.: mean$\overline{|\boldsymbol{M} - \boldsymbol{M}_{\text{f}}|}$ of the solutions obtained using the L-curve method in dependence of the number of fieldboxes used as target domain Ω_{t} for a noise level of (a) 10^{-5}, (b) 10^{-4}, (c) 10^{-3} and (d) 10^{-2}.

Regarding the ability to extrapolate the field in areas not part of the target domain Ω_t, using one fieldbox as input, in the same way as for the reconstruction of the magnetization state the regularization term T_{norm} with $\boldsymbol{M}_{\text{init}} = (0,0,0)$ performs best over all noise levels. This can be seen in Figure 5.25 where the solutions obtained using the L-curve method are plotted in dependence of the noise levels. Using fictitious magnetic charges as control variables, for low noise levels the field extrapolation performance is significantly worse compared to using the magnetization. However, for a noise level of 10^{-2} using $\rho_{\text{m,init}} = 0$ and $\sigma_{\text{m,init}} \approx \boldsymbol{M}_{\text{init}} = (0,0,1)$, the mean$|\overline{\boldsymbol{H} - \boldsymbol{H}_{\text{f}}}|$ is only 0.43% larger compared to using the magnetization with T_{grad} and $\boldsymbol{M}_{\text{init}} = (0,0,1)$ that performs better than T_{grad} with $\boldsymbol{M}_{\text{init}} = (0,0,0)$. Note that the solutions obtained using fictitious magnetic charges with $\rho_{\text{m,init}} = 0$ and $\sigma_{\text{m,init}} = 0$ again perform significantly worse and are not visible in Figure 5.25. In comparison to the field extrapolation capabilities in the case of using two fieldboxes as input, the increase in mean$|\overline{\boldsymbol{H} - \boldsymbol{H}_{\text{f}}}|_{\Omega_e}$ between the lowest mean$|\overline{\boldsymbol{H} - \boldsymbol{H}_{\text{f}}}|_{\Omega_e}$ value obtained using two fieldboxes (compare Figure 5.20) and the lowest mean$|\overline{\boldsymbol{H} - \boldsymbol{H}_{\text{f}}}|_{\Omega_e}$ obtained using one fieldbox as input, over all noise levels is $360.66 \pm 125.10\%$.

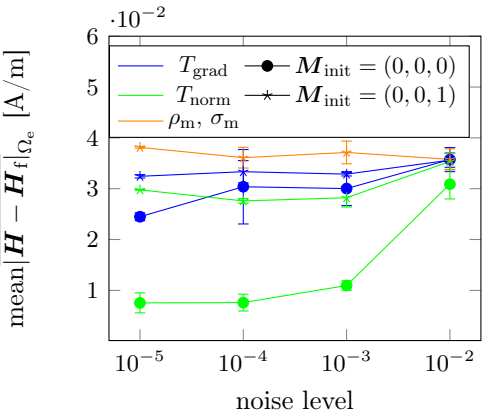

Figure 5.25.: Comparison of the quality of the field extrapolation (mean$|\overline{\boldsymbol{H} - \boldsymbol{H}_{\text{f}}}|_{\Omega_e}$) in dependence of the noise level for different control variables, regularization terms and initial magnetizations for source reconstructions with one fieldbox as input.

Note, that not only regarding the solutions obtained using the L-curve method but also regarding the overall best possible solution in the case of using 1 fieldbox as target domain Ω_t the source reconstructions using the regularization term T_{norm} with an initial magnetization $\boldsymbol{M}_{\text{init}} = (0,0,0)$ deliver the best solutions in terms of reconstruction of the reference flower state as well as in terms of field extrapolation quality. This is also true for the examples presented in the following and therefore, only this source reconstructions are considered from here on.

Changing input fieldbox size

In order to further investigate the dependence of the quality of the reconstructed magnetization state in dependence of the available spatial information of the magnetic stray field, the dependence on the size of the fieldbox used as target domain Ω_t is investigated. In order to do so, two additional fieldboxes are considered and the results are compared to the results obtained using the default fieldbox with a thickness of 0.04 mm and an are of 1×1 mm^2 having 600 elements. The first additional fieldbox has the same thickness of 0.04 mm and an area of 1.5×1.5 mm^2 (1350 elements) and the second additional fieldbox has a thickness of 0.08 mm and also an area of 1.5×1.5 mm^2 (2700 elements). Note, that both additional fieldboxes have the same distance from the magnetic unit cube as the default fieldbox. Furthermore, while using the first additional fieldbox enlarges the area containing information about the stray field parallel to the unit cubes surface and more than doubles the measurment points used as input for the source reconstruction problem, using the second additional fieldbox only enlarges the area further away from the unit cube and doubles the number of measurement points with respect to the first additional fieldbox. For each field box source reconstructions using the magnetization as control variable were performed for three different target fields for each noise level. Note that, since the fieldbox size and the number of elements in each fieldbox are different also the target fields are different.

In Figure 5.26 the dependence of mean$|\boldsymbol{M} - \boldsymbol{M}_f|$ on the fieldbox size (depicted as number of elements inside the fieldbox) for each noise level is plotted for the source reconstructions using the regularization term T_{norm} with $\boldsymbol{M}_{\text{init}} = (0, 0, 0)$. Generally, it can be observed that mean$|\boldsymbol{M} - \boldsymbol{M}_f|$ decreases when using larger fieldboxes as is not surprising since a larger fieldbox provides more information to the inverse problem in terms of spatial distribution of the forward field, but also in terms of number of measurement points. In Table 5.1 the decreases of mean$|\boldsymbol{M} - \boldsymbol{M}_f|$, and therefore the increase in quality of the reconstructed magnetization state, in percent with respect to the results using the default fieldbox are shown for both additional fieldboxes. Regarding the best possible solutions the decrease in mean$|\boldsymbol{M} - \boldsymbol{M}_f|$ is monotonous with increasing fieldbox size except for a noise level of 10^{-3} where after mean$|\boldsymbol{M} - \boldsymbol{M}_f|$ decreased for 12.91% using the larger area fieldbox it increases again by 1.26% using the largest fieldbox with 2700 elements. Furthermore, note that the increase using the largest fieldbox is not significant compared to the increase using the larger fieldbox for lower noise levels, even though the largest fieldbox contains double the amount of measurement points compared to the larger fieldbox. Only for a noise level of 10^{-2} using the largest fieldbox significantly improves the quality of the reconstructed magnetization state. This suggest that for a larger noise level, more information as input to the source reconstruction problem is needed to smooth out the higher noise. Regarding the solutions ob-

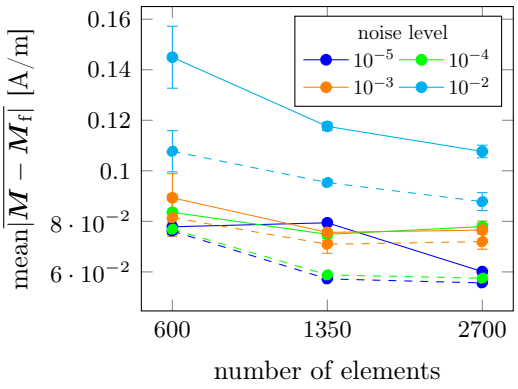

Figure 5.26.: mean$|\boldsymbol{M} - \boldsymbol{M}_f|$ for the best possible solutions (dashed lines) and the solutions obtained using the L-curve method (solid lines) in dependence of the fieldbox size (depicted as number of elements in fieldbox) for different noise levels.

	decrease in % with respect to default fieldbox	
noise level	1350 elements	2700 elements
10^5	24.86	26.94
10^4	23.49	25.21
10^3	12.91	11.65
10^2	11.50	18.51

(a)

	decrease in % with respect to default fieldbox	
noise level	1350 elements	2700 elements
10^5	-2.03	22.78
10^4	10.46	6.76
10^3	15.33	14.29
10^2	18.88	25.73

(b)

Table 5.1.: Decrease of mean$|\boldsymbol{M} - \boldsymbol{M}_\mathrm{f}|$ with respect to the source reconstructions using the default fieldbox for (a) the best possible solutions and (b) the solutions obtained using the L-curve method for the source reconstructions using the two additional fieldboxes (referred to by their respective number of elements).

tained using the L-curve evaluation also a significant decrease in mean$|\boldsymbol{M} - \boldsymbol{M}_\mathrm{f}|$ can be seen using a larger area of the stray field as input to the source reconstruction problem. However, here the decrease is higher for higher noise levels of 10^{-3} and 10^{-2}. This is due to the fact that for lower noise levels of 10^{-5} and 10^{-4} the additional kink in the L-curve for lower values of the regularization parameter, as already discussed above, reappears for both larger fieldboxes and the solutions found using the L-curve method are again further away from the best possible solutions. However, apart from an increase in mean$|\boldsymbol{M} - \boldsymbol{M}_\mathrm{f}|$ of 2.03% using the larger fieldbox containing 1350 data points, increasing the fieldbox size still significantly increases the quality of the reconstructed magnetization state.

In order to investigate the quality of the extrapolated field, in Figure 5.27 mean$|\boldsymbol{H} - \boldsymbol{H}_\mathrm{f}|_{\Omega_\mathrm{e}}$ is plotted in dependence of the fieldbox size and in Table 5.2 the relative decrease of mean$|\boldsymbol{H} - \boldsymbol{H}_\mathrm{f}|_{\Omega_\mathrm{e}}$ in % with respect to using the default fieldbox is presented. Regarding the best possible solutions a significant decrease in mean$|\boldsymbol{H} - \boldsymbol{H}_\mathrm{f}|_{\Omega_\mathrm{e}}$ can be seen for all noise levels and fieldbox sizes. Note, that the decrease using the largest fieldbox with 2700 elements is increased by an average factor of 1.91 with respect to the decrease using the larger fieldbox with 1350 elements for all noise levels except 10^{-3}. This corresponds to the increase in number of measurement points used as input between the two fieldboxes and is in contrast to mean$|\boldsymbol{M} - \boldsymbol{M}_\mathrm{f}|$ where this increase was much lower. Only for a noise level of 10^{-3} the additional information actually lead to an increase in mean$|\boldsymbol{H} - \boldsymbol{H}_\mathrm{f}|_{\Omega_\mathrm{e}}$. Furthermore, regarding the solutions obtained using the L-curve method, for low noise levels of 10^{-5} and 10^{-4} the decrease in mean$|\boldsymbol{H} - \boldsymbol{H}_\mathrm{f}|_{\Omega_\mathrm{e}}$ is almost identical to the decrease found for the best possible solutions. This is since even though the L-curve shows the additional kink at lower values

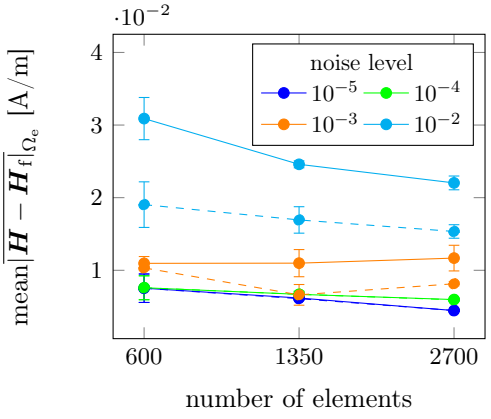

Figure 5.27.: mean$|\boldsymbol{H} - \boldsymbol{H}_\mathrm{f}|_{\Omega_\mathrm{e}}$ for the best possible solutions (dashed lines) and the solutions obtained using the L-curve method (solid lines) in dependence of the fieldbox size (depicted as number of elements in fieldbox) for different noise levels.

	decrease in % with respect to default fieldbox	
noise level	1350 elements	2700 elements
10^5	18.97	40.78
10^4	11.94	21.81
10^3	35.96	21.18
10^2	11.07	19.42

(a)

	decrease in % with respect to default fieldbox	
noise level	1350 elements	2700 elements
10^5	17.91	40.84
10^4	11.94	21.42
10^3	-0.25	-6.59
10^2	20.39	28.67

(b)

Table 5.2.: Decrease of mean$\overline{|\boldsymbol{H} - \boldsymbol{H}_\mathrm{f}|}_{\Omega_\mathrm{e}}$ with respect to the source reconstructions using the default fieldbox for (a) the best possible solutions and (b) the solutions obtained using the L-curve method for the source reconstructions using the two additional fieldboxes (referred to by their respective number of elements).

of α where the optimal solution regarding $\overline{|\boldsymbol{M} - \boldsymbol{M}_\mathrm{f}|}$ is found, regarding $\overline{|\boldsymbol{H} - \boldsymbol{H}_\mathrm{f}|}_{\Omega_\mathrm{e}}$ the regularization parameter value found using the L-curve evaluation is very close or identical to the best possible value regarding $\overline{|\boldsymbol{H} - \boldsymbol{H}_\mathrm{f}|}_{\Omega_\mathrm{e}}$. However, for a noise level of 10^{-3} actually an increase of mean$\overline{|\boldsymbol{H} - \boldsymbol{H}_\mathrm{f}|}_{\Omega_\mathrm{e}}$ is observed when using a larger fieldbox. The increase corresponds to an increase in the difference between the best regularization parameter and the regularization parameter found using the L-curve method between using the default fieldbox and the larger fieldboxes. Furthermore, for a noise level of 10^{-2} the decrease in mean$\overline{|\boldsymbol{H} - \boldsymbol{H}_\mathrm{f}|}_{\Omega_\mathrm{e}}$ for the solutions obtained using the L-curve method is larger compared to the best possible solutions. This coincides with the regularization parameter found using the L-curve method getting close to the best possible regularization parameter for larger fieldboxes compared to the default fieldbox.

Concluding it can be said, that increasing the area from where measurement points are taken as input for the source reconstruction problem is advantageous within the region investigated by this numerical experiment. However, in specific cases the error introduced using the L-curve evaluation leads to a practical decrease of the quality of the reconstructed source variable, be it the reconstructed magnetization state or the extrapolated magnetic field.

	decrease in % with respect to fieldbox with 1350 elements	
noise level	2700 elements	4050 elements
10^5	-0.03	0.09
10^4	1.12	1.65
10^3	-1.10	-0.11
10^2	9.22	11.09

(a)

	decrease in % with respect to fieldbox with 1350 elements	
noise level	2700 elements	4050 elements
10^5	0.93	-0.15
10^4	-2.72	-3.05
10^3	-2.03	-0.07
10^2	3.77	4.93

(b)

Table 5.3.: Decrease of mean$|\boldsymbol{M} - \boldsymbol{M}_\mathrm{f}|$ with respect to the source reconstructions using 1350 measurement points inside the fieldbox for (a) the best possible solutions and (b) the solutions obtained using the L-curve method for the source reconstructions using the an increased number of 2700 and 4050 measurement points inside the fieldbox.

Changing number of field points in fieldbox

In order to separately investigate the dependence of the source reconstruction on the number of input measuement points with unchages spatial domain from where the measurements are taken, the data point density inside a fieldbox with a thickness of 0.04 mm and an area of 1.5×1.5 mm^2 is increased while keeping the fieldbox geometry unchanged. In detail, the number of mesh cells in vertical direction inside the fieldbox is doubled and triplet, therefore increasing the number of measurement points inside the fieldbox from 1350 to 2700 and 4050. Note, that the increase from 1350 to 2700 measurement points inside the fieldbox corresponds to the increase in measurement points provided using the thicker fieldbox in the example presented above. The source reconstructions were again performed for three different target fields for each noise level created with different random seeds.

In Figure 5.29 mean$|\boldsymbol{M} - \boldsymbol{M}_\mathrm{f}|$ is plotted in dependence of the number of measurement points used as input for the source reconstruction problem and in Table 5.3 the relative decrease of mean$|\boldsymbol{M} - \boldsymbol{M}_\mathrm{f}|$ in % with respect to the fieldbox containing 1350 measurement points is shown. It can be seen that for noise levels lower 10^{-2} adding additional measurement points inside the same measurement domain does not improve the quality of the reconstructed magnetization state. This is true for the best possible solutions where the average decrease is 0.27% considering both densities as well as for the solutions obtained using the L-curve method where on average mean$|\boldsymbol{M} - \boldsymbol{M}_\mathrm{f}|$ actually increases by 1.52%. However, for a noise level of 10^{-2} for the best possible as well as for the solutions obtained using the L-curve method a significant decrease in mean$|\boldsymbol{M} - \boldsymbol{M}_\mathrm{f}|$ can be seen by increasing the measurement point density inside the fieldbox.

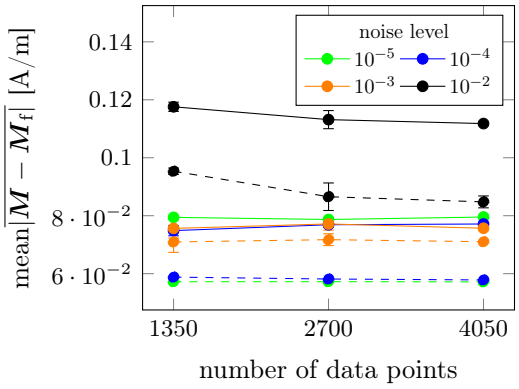

Figure 5.28.: mean$|\boldsymbol{M} - \boldsymbol{M}_\mathrm{f}|$ for the best possible solutions (dashed lines) and the solutions obtained using the L-curve method (solid lines) in dependence of the number of measurement points inside the fieldbox for different noise levels.

	decrease in % with respect to fieldbox with 1350 elements	
noise level	2700 elements	4050 elements
10^5	9.11	7.03
10^4	4.23	6.06
10^3	-23.41	-21.25
10^2	11.55	19.44

(a)

	decrease in % with respect to fieldbox with 1350 elements	
noise level	2700 elements	4050 elements
10^5	2.30	-1.77
10^4	4.23	6.06
10^3	-14.86	-8.23
10^2	5.16	6.20

(b)

Table 5.4.: Decrease of mean$\overline{|\boldsymbol{H}-\boldsymbol{H}_\mathrm{f}|}_{\Omega_\mathrm{e}}$ with respect to the source reconstructions using 1350 measurement points inside the fieldbox for (a) the best possible solutions and (b) the solutions obtained using the L-curve method for the source reconstructions using the an increased number of 2700 and 4050 measurement points inside the fieldbox.

In Figure 5.29 mean$\overline{|\boldsymbol{H}-\boldsymbol{H}_\mathrm{f}|}_{\Omega_\mathrm{e}}$ is plotted in dependence of the data point density inside the fieldbox and in Table 5.4 the relative decrease of mean$\overline{|\boldsymbol{H}-\boldsymbol{H}_\mathrm{f}|}_{\Omega_\mathrm{e}}$ in % with respect to the fieldbox containing 1350 measurement points is given. It can be seen that for a noise level of 10^{-3} the quality of the extrapolated field decreases significantly when increasing the number of measurement points inside the fieldbox for both, the best possible and the solutions obtained using the L-curve method. For all other noise levels increasing the measurement point density inside the fieldbox, for the best possible as well as for the solutions obtained using the L-curve method, monotonically decreases mean$\overline{|\boldsymbol{H}-\boldsymbol{H}_\mathrm{f}|}_{\Omega_\mathrm{e}}$ except for a noise level of 10^{-5} where tripling the number of measurement points inside the fieldbox leads to higher mean$\overline{|\boldsymbol{H}-\boldsymbol{H}_\mathrm{f}|}_{\Omega_\mathrm{e}}$ comparing to doubling them.

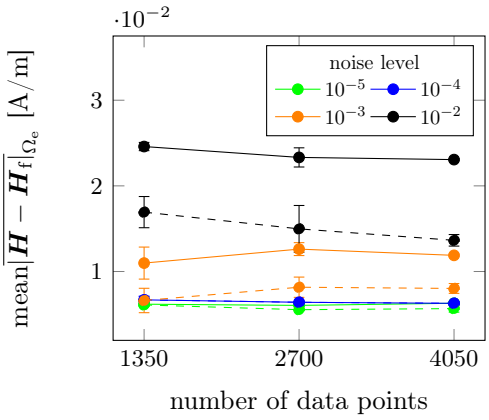

Figure 5.29.: mean$\overline{|\boldsymbol{H}-\boldsymbol{H}_\mathrm{f}|}_{\Omega_\mathrm{e}}$ for the best possible solutions (dashed lines) and the solutions obtained using the L-curve method (solid lines) in dependence of the number of measurement points inside the fieldbox for different noise levels.

Since doubling the number of measurement points inside the fieldbox increases the number of measurement points used as input for the source reconstruction problem in the same way as using the thicker fieldbox in the previous section does, these cases can be compared to investigate whether increasing the spatial density of measurements taken from an identical spatial domain or using a larger spatial domain keeping the measurement density constant is advantageous. To this aim in Table 5.5 the decrease in mean$\overline{|\boldsymbol{M}-\boldsymbol{M}_\mathrm{f}|}$ when increasing the measurement points in the two ways is compared for both the best possible and the solutions obtained using the L-curve method. It can be seen that regarding the best possible solutions none of the two methods are advantageous over all noise levels. Regarding the solutions found using the L-curve method however, using a larger fieldbox is of clear advantage, ecpecially for a noise level of 10^{-5} and 10^{-2} where the decrease in mean$\overline{|\boldsymbol{M}-\boldsymbol{M}_\mathrm{f}|}$ by increasing the spatial density is 0.93 and 3.77 % respectively, while the decrease using an extended fieldbox is 24.81 and 6.85 % respectively. Furthermore in Table 5.6 the decrease in mean$\overline{|\boldsymbol{H}-\boldsymbol{H}_\mathrm{f}|}_{\Omega_\mathrm{e}}$ is

	decrease in % with respect to fieldbox with 1350 elements	
noise level	denser box	larger box
10^5	-0.03	2.08
10^4	1.12	1.71
10^3	-1.10	-1.25
10^2	9.22	7.01

(a)

	decrease in % with respect to fieldbox with 1350 elements	
noise level	denser box	larger box
10^5	0.93	24.81
10^4	-2.72	-3.69
10^3	-2.03	-1.04
10^2	3.77	6.85

(b)

Table 5.5.: Comparison of the decrease in mean$\overline{|\boldsymbol{M} - \boldsymbol{M}_\mathrm{f}|}$ when increasing the number of measurement points used as input for the source reconstruction problem from 1350 to 2700 by increasing the measurement density and by increasing the size of the measurement area for (a) the best possible solutions and (b) the solutions obtained using the L-curve method.

	decrease in % with respect to fieldbox with 1350 elements	
noise level	denser box	larger box
10^5	9.11	21.81
10^4	4.23	9.87
10^3	-23.41	-14.78
10^2	11.55	8.34

(a)

	decrease in % with respect to fieldbox with 1350 elements	
noise level	denser box	larger box
10^5	2.30	22.93
10^4	4.23	9.47
10^3	-14.86	-6.35
10^2	5.16	8.28

(b)

Table 5.6.: Comparison of the decrease in mean$\overline{|\boldsymbol{H} - \boldsymbol{H}_\mathrm{f}|}_{\Omega_\mathrm{e}}$ when increasing the number of measurement points used as input for the source reconstruction problem from 1350 to 2700 by increasing the measurement density and by increasing the size of the measurement area for (a) the best possible solutions and (b) the solutions obtained using the L-curve method.

compared. Here, except for a noise level of 10^{-2} where for the best possible solutions increasing the density of the measurement points decreases mean$\overline{|\boldsymbol{H} - \boldsymbol{H}_\mathrm{f}|}_{\Omega_\mathrm{e}}$ by 11.55% compared to 8.34% by enlarging the fieldbox, increasing the spatial domain from where the measurements are taken is always advantageous.

5.3. Conclusion

In conclusion, the detailed investigation of the source reconstruction of a magnetic flower state inside a permanent magnetic unit cube revealed several insights.

With the magnetization as control variable, it has been shown that decreasing the size of the target domain from which measurement information is available to the source reconstruction problem does not monotonically decrease the quality of the reconstructed magnetization state for all noise levels. Using measurement input from each side of the magnetic unit cube within 6 fieldboxes, using the L-curve method to obtain the optimal value of the regularization parameter α, for a noise level of 10^{-2} the reconstructed magnetization state showed an average difference of 63.04 ± 0.45 mA/m, with respect to the reference flower state, using T_{grad} as regularization term and $\boldsymbol{M}_{\text{init}} = (0, 0, 1)$ as initial magnetization. Reducing the target domain to two fieldboxes on opposite sides of the cube this increased to 69.87 ± 1.57 mA/m for T_{norm} with $\boldsymbol{M}_{\text{init}} = (0, 0, 1)$ and to 144.94 ± 12.26 mA/m using one fieldbox with T_{norm} $\boldsymbol{M}_{\text{init}} = (0, 0, 0)$. Note that this constitutes a relative increase in difference of 129.92% between the case using 6 fieldboxs and using one fieldbox. Especially the decrease in quality between using two fieldboxes on opposite sides of the unit cube and using one fieldbox is significant. It can be explained by the fact, that with increasing distance, the spatial field characteristics produced by a given magnetization decrease and therefore, using only information of the magnetic field from one side of the unit cube, the magnetization state at the opposite side can only be reconstructed with reduced accuracy. For a noise level of 10^{-5} in contrast, while for 6 fieldboxes the best reconstructions are obtained using T_{grad} and $\boldsymbol{M}_{\text{init}} = (0, 0, 0)$ with an average difference of 67.21 ± 2.33 mA/m, for two fieldboxes this decreases to 56.33 ± 1.38 mA/m with T_{norm} and $\boldsymbol{M}_{\text{init}} = (0, 0, 1)$ and then increases for one fieldbox using T_{norm} and $\boldsymbol{M}_{\text{init}} = (0, 0, 0)$ to 77.85 ± 0.22 mA/m. Note, that here the relative increase between using 6 fieldboxes and using one fieldbox is only 15.83%. The presented values additionally show, that no individual regularization term or initial magnetization is advantageous for all cases. However, when reducing the number of fieldboxes from which measurement information is available to the source reconstruction problem it was found that using the regularization term T_{grad} becomes problematic. This is since T_{grad} enforces a regularization on the magnetization independent of the distance to the domain from where measurements are taken, whereas the influence of the magnetization inside a given domain on the residual term depends on its distance from the domain where the magnetic field is considered. Therefore, when the regularization is strong enough to prevent the magnetization from over-fitting in proximity of the target domain, it over-regularizes the magnetization far away from the target domain. That this is not the case for T_{norm} is based in the fact that T_{norm} actually imposes a regularization on the magnetization state that is fulfilled for the reference magnetization state. A possible improvement mitigating this problem could be enforcing the same distance dependence on the regularization term T_{grad} that is present naturally in the residual term.

Furthermore, using one fieldbox, the dependence of the reconstructed magnetization state on the number of measurement points used as input for the source reconstruction problem has been investigated by enlarging the fieldbox and by increasing the density of measurement points inside the fieldbox. It was found that while both methods increase the quality of the reconstructed magnetization state especially for higher levels of noise, enlarging the fieldbox is generally advantageous. However, increasing the number of measurement points while using one fieldbox, for the examples shown, the quality of the reconstructed magnetization state was not increased to reach the quality of the reconstructed magnetizations state using measurements from two fieldboxes at opposite sides of the magnetic unit cube. In detail, the best source reconstructions

using one fieldbox, obtained for a fieldbox with increased area of 1.5×1.5 mm^2 and thicknes of 0.08 mm containing 2700 measurement points, for a noise level of 10^{-5} the difference to using two fieldboxes is 6.73%, while for a noise level of 10^{-2} the difference is higher with 54.08%.

Additionally, the quality of the magnetic field produced by the reconstructed magnetization state in areas that were not part of the input to the source reconstruction problem, referred to as field extrapolation, was investigated. The results show that when using two fieldboxes as input, the field within the four remaining fieldboxes can be reconstructed with a relative error below 5% for all noise levels and the quality of the extrapolated field decreases monotonically with increasing noise. Using 1 fieldbox the ability to extrapolate to the noise free forward field within the remaining five fieldboxes decreases. In detail, using the most advantageous fieldbox of size 1.5×1.5 mm^2 and thickness of 0.08 mm containing 2700 measurement points, the difference between the noise free forward field and the extrapolate field increases by up to 301.63% for the worst case for a noise level of 10^{-2}, compared to using two fieldboxes. Note, that it has been found that the magnetization state showing the smallest difference to the the reference flower state did not necessarily perform best with respect to field extrapolation.

Furthermore, the usage of fictitious magnetic charges as control variables replacing the magnetization was investigated. The idea here was that using fictitious magnetic charges would improve the source reconstruction process since on the one hand it removes the inherent ill-posedness present when using the magnetization as control variable and on the other hand it reduces the number of optimization variables by almost a factor of three. However, for the presented example, regarding reconstruction of the magnetization state, for all noise levels the difference of the reconstructed magnetization state to the reference flower state was higher using fictitious magnetic charges compared to using the magnetization as control variable. Regarding field extrapolation using one fieldbox, while the difference of the reconstructed field is also higher compared to using the magnetization as control variable for all noise levels, the difference decreases with increasing noise. In detail, while for a noise level of 10^{-5} the difference is 55.76% higher using fictitious magnetic charges, this decreases monotonically to only 0.43% for a noise level of 10^{-2} using the regularization term T_{grad} that is comparable to the regularization term T_{charges} used for the fictitious charges. The fact, that this decrease is not observed regarding the reconstructed magnetization state suggests, that the large difference of the reconstructed magnetization state with respect to the reference flower state is at least partly rooted in the numerical error introduced by the additional calculation necessary in order to obtain a magnetization state from a charge distribution. Furthermore, note that by introducing fictitious magnetic charges, the source reconstruction problem becomes a simultaneous distributed-boundary optimal control problem. The two control variables, the fictitious magnetic volume charges constituting the distributed control variable and the surface charges constituting the boundary control variable, are inherently different. However, the current implementation of the presented algorithm does not in any way treat them differently, but passes the combined gradient to the minimization algorithm. As a consequence the same parameters (e.g. the same step length) are used for both variables. This procedure could certainly be improved respecting their inherent differences.

Regarding the technicality of obtaining an optimal solution in dependence of the enforced regularization, while for some cases using the L-curve method the best possible solution was found, generally, a significant difference between the best possible solutions and the solutions obtained using the L-curve method was observed for all presented cases and all regularization terms used. This suggests that additional effort can improve the solution quality significantly. Possible improvements could be gained on the one hand by automation of the procedure of finding the

optimal value of the regularization parameter by means of fitting the L-curve and performing the source reconstruction for the expected optimal value of the regularization parameter. Furthermore, since cases were the optimal solution was not found at the kink of the L-curve, but at additional smaller kinks in the domain where over-fitting is expected, performing additional numerical experiments and training a machine learning algorithm could help find patterns and systematic relationships revealing the true optimal regularization parameter values. Being able to more reliably predict where the optimal regularization parameter can be found furthermore has the potential to reduce the number of necessary optimizations that have to be performed in order to find the best regularization parameter, thereby decreasing the computational effort necessary to perform the source reconstructions.

6. Conclusion and Outlook

6.1. Conclusion

Within this thesis a method to solve the inverse magnetostatic problem within the framework of partial differential equation (PDE)-constrained optimization has been presented. Within this framework the inverse problem is represented as an optimization problem. The gradient which is required to iteratively solve this optimization problem has been derived utilizing the adjoint method. During the derivation, the difference between the gradient and the derivative, that is often overlooked in other works has been established. The developed method was then applied to problems of optimal design, namely to the direct optimization of the topology as well as of the magnetization state of a magnetic structure and to problems of source reconstruction, namely to the reconstruction of a magnetic structures topology or its magnetization state.

On the basis of the derived method a software package on the basis of magnum.fe [19] that itself utilizes the finite element library FEniCS [20] was successfully implemented using python. Several examples have been presented validating the algorithms abilities. Specifically two problem classes were investigated, the topology optimization of hard as well as soft magnetic structures and the reconstruction of the magnetization state of a magnetic structure.

Regarding topology optimization, the topology of hard and soft magnetic thin film flux guide concentrators and the topology of a magnetic recording write head used for heat-assisted magnetic recording was successfully optimized. The presented examples showed, that the optimization of soft magnetic structures is more delicate compared to the optimization of hard magnetic structures. In particular, a greater dependence on optimization parameters leading to an increase in computational effort was observed. This is since for a non-zero susceptibility the minimization problem becomes non-linear even in the case of a linear material law. Furthermore, a dependency of the optimization process on the exact size of the gradient using continuous optimization algorithms was found. This lead to the implementation of a binary topology optimization algorithm independent of the exact gradient size. It was shown that the obtained topologies were improved using the binary topology optimization algorithm while simultaneously decreasing the computational effort needed. Furthermore, optimizing the topology of a magnetic recording write head used for heat-assisted magnetic recording, considering the complete head design during optimization, the capability of the algorithm to solve large scale topology optimization problems has been shown. For this example, also the impact of using simplified, linearized material characteristics in order to speed up the solution process was investigated. The investigation showed the importance of using the full non-linear material characteristics whenever saturation effects play a role. A comparison of the optimization processes of the presented examples showed that the parameter sets delivering the optimal topologies are not identical for each presented example. This makes a parameter study necessary whenever a new topology is to be optimized. Note, that for the presented examples also the difference between the derivative and the gradient was

investigated. It was found that using the derivative leads to poorer performance during optimization especially when refined meshes are used. A more detailed conclusion of the examples with respect to topology optimization can be found at the end of chapter 4 in section 4.4.

With respect to source reconstruction, as an example, the source reconstruction of a magnetic unit cube was investigated in detail. The results showed the capability of the algorithm to reconstruct the magnetization state of a magnetic structure. However, with decreasing measurement points used as input for the inverse problem, the quality of the reproduced magnetization state reduces significantly. The dependency on the position and number of measurement points was investigated in detail. A detailed conclusion is given at the end of chapter 5 in section 5.3. The example of the magnetic unit cube was also used to investigate the quality of the magnetic field generated by the reconstructed magnetization state in regions that were not part of the input for the inverse problem. This is called field extrapolation. Furthermore, a method for the source reconstruction using fictitious magnetic charges as design variables has been implemented. Using fictitious magnetic charges, the minimization process was thought to be simplified since with respect to using the magnetization as design variable, the number of optimization variables reduces, depending on the exact shape of the structure, by almost a factor of three and furthermore a unambiguous correspondence exists between a given distribution of fictitious magnetic charges and the produced magnetic field, where the magnetization distribution producing a magnetic field is only unambiguous up to an arbitrary solenoidal part. However, for the investigated parameter region no improvement introduced by the usage of fictitious magnetic charges has been found.

6.2. Outlook

The presented method to solve the inverse magnetostatic problem can be improved further. This is especially true regarding more complicated optimization problems where the objective functional might be comprised of several, possibly competing terms. Optimization problems of this form can have a multitude of local minima. Therefore, in order to find the global optimum, global optimization schemes can be employed as e.g. done in [45].

An extension of the presented topology optimization approach would furthermore be to enable the possibility to use several materials simultaneously, as e.g. done in [65]. This would allow for the possibility to design the topology of magnetic structures consisting of soft as well as hard magnetic materials.

Also, the algorithm could be extended to enable designing of the direction of the anisotropy axis of an anisotropic hard magnetic structure. To do this, the remanence magnetization vector $\boldsymbol{M}_\mathrm{r} = |M_r|\,\hat{\boldsymbol{M}}_\mathrm{r}$ pointing in the direction of the anisotropy axis has to be used as design variable directly. The gradients necessary for the optimization can be derived using the adjoint approach as presented within this thesis. In order to only optimize the direction of the anisotropy axis, the length of the remanence magnetization vector could either be kept constant by using a regularization term or by using an optimization algorithm that keeps the length constant. The optimized structures can then be fabricated using 3D printing as has recently been shown in [66].

Regarding the source reconstruction of magnetic structures, the evaluation of the L-curve method offers room for improvement. This could include fitting of the L-curve to obtain the optimal regularization parameter, as well as using machine learning techniques.

Furthermore, here the recent increased attention in the possibility to use deep learning to design magnetic structures (see e.g. [67] and [68]) should be mentioned.

Bibliography

[1] Kurt H. J. Buschow, ed. *Handbook of magnetic materials. 19.* 1. ed. Amsterdam Heidelberg: Elsevier, 2011. 436 pp. ISBN: 978-0-444-53780-5.

[2] C.P.O Treutler. "Magnetic sensors for automotive applications". In: *Sensors and Actuators A: Physical* 91.1 (June 2001), pp. 2–6. DOI: 10.1016/S0924-4247(01)00621-5.

[3] Klaus Elian and Horst Theuss. "Integration of polymer bonded magnets into magnetic sensors". In: IEEE, Sept. 2014, pp. 1–5. ISBN: 978-1-4799-4026-4. DOI: 10.1109/ESTC.2014.6962754.

[4] Konrad Kapser and James Sterling. "Integrated GMR based Wheel Speed Sensor for Automotive Applications". In: IEEE, 2007, pp. 848–851. ISBN: 978-1-4244-1261-7. DOI: 10.1109/ICSENS.2007.4388534.

[5] Helmut Koeck et al. "Multi-physics based system simulations for magnetic sensors". In: IEEE, Apr. 2017, pp. 1–5. ISBN: 978-1-5090-4344-6. DOI: 10.1109/EuroSimE.2017.7926274.

[6] R. Bjørk et al. "Review and comparison of magnet designs for magnetic refrigeration". In: *International Journal of Refrigeration* 33.3 (May 2010), pp. 437–448. DOI: 10.1016/j.ijrefrig.2009.12.012.

[7] Oliver Gutfleisch et al. "Magnetic Materials and Devices for the 21st Century: Stronger, Lighter, and More Energy Efficient". In: *Advanced Materials* 23.7 (Feb. 15, 2011), pp. 821–842. DOI: 10.1002/adma.201002180.

[8] P. Neittaanmäki, M. Rudnicki, and A. Savini. *Inverse problems and optimal design in electricity and magnetism.* Monographs in electrical and electronic engineering 35. Oxford [England] ; New York : New York: Clarendon Press ; Oxford University Press, 1996. 367 pp. ISBN: 978-0-19-859383-6.

[9] John J. Croat and J. G. Ormerod, eds. *Modern permanent magnets.* OCLC: 1294316818. Cambridge: Woodhead Publishing, 2022. ISBN: 978-0-323-88640-6.

[10] "Injection molding of polymer-bonded magnets with multipolar structure". In: *Proceedings of the 66th Annual Technical Conference of the Society of Plastics Engineers, Plastics Encounter at (ANTEC'08).* In collab. with S Eimeke et al. 2008, pp. 1504–1508.

[11] Florian Bruckner et al. "Macroscopic simulation of isotropic permanent magnets". In: *Journal of Magnetism and Magnetic Materials* 401 (Mar. 2016), pp. 875–879. DOI: 10.1016/j.jmmm.2015.11.005.

[12] C. Huber et al. “3D print of polymer bonded rare-earth magnets, and 3D magnetic field scanning with an end-user 3D printer”. In: *Applied Physics Letters* 109.16 (Oct. 17, 2016), p. 162401. DOI: 10.1063/1.4964856.

[13] Ling Li et al. “Additive manufacturing of near-net-shape bonded magnets: Prospects and challenges”. In: *Scripta Materialia* 135 (July 2017), pp. 100–104. DOI: 10.1016/j.scriptamat.2016.12.035.

[14] Jaćim Jaćimović et al. “Net Shape 3D Printed NdFeB Permanent Magnet: Net Shape 3D Printed NdFeB Permanent Magnet”. In: *Advanced Engineering Materials* 19.8 (Aug. 2017), p. 1700098. DOI: 10.1002/adem.201700098.

[15] Klaus Sonnleitner et al. “3D printing of polymer-bonded anisotropic magnets in an external magnetic field and by a modified production process”. In: *Applied Physics Letters* 116.9 (Mar. 2, 2020), p. 092403. DOI: 10.1063/1.5142692.

[16] Hendrik Husstedt and Manfred Kaltenbacher. “Detailed analysis of permanent magnets by means of free field measurements”. In: *Journal of Applied Physics* 115.17 (May 7, 2014), 17E302. DOI: 10.1063/1.4852096.

[17] Richard C. Aster and Clifford H. Thurber. *Parameter estimation and inverse problems*. 2nd ed. Waltham, MA: Academic Press, 2013. 360 pp. ISBN: 978-0-12-385048-5.

[18] Michael Hinze, ed. *Optimization with PDE constraints*. Mathematical modelling 23. OCLC: 255277417. Dordrecht: Springer, 2009. 270 pp. ISBN: 978-1-4020-8839-1 978-1-4020-8838-4.

[19] Claas Abert et al. “magnum.fe: A micromagnetic finite-element simulation code based on FEniCS”. In: *Journal of Magnetism and Magnetic Materials* 345 (Nov. 2013), pp. 29–35. DOI: 10.1016/j.jmmm.2013.05.051.

[20] Anders Logg, Kent-Andre Mardal, and Garth N. Wells, eds. *Automated solution of differential equations by the finite element method: the FEniCS book*. Lecture notes in computational science and engineering 84. OCLC: 794507863. Berlin Heidelberg Dordrecht London New York: Springer, 2012. 723 pp. ISBN: 978-3-642-23099-8 978-3-642-23098-1.

[21] Tobias Schwedes et al. *Mesh Dependence in PDE-Constrained Optimisation*. Cham: Springer International Publishing, 2017. ISBN: 978-3-319-59482-8 978-3-319-59483-5. DOI: 10.1007/978-3-319-59483-5.

[22] Gregor Wautischer et al. “A topology optimization algorithm for magnetic structures based on a hybrid FEM–BEM method utilizing the adjoint approach”. In: *Scientific Reports* 12.1 (Jan. 2022), p. 1119. DOI: 10.1038/s41598-021-04246-z.

[23] Florian Bruckner. “Multiscale simulation of magnetic nanostructures”. Dissertation. Technische Universität Wien, 2013.

[24] Miklós Kuczmann. *Potential Formulations in Magnetics Applying the Finite Element Method*. Laboratory of Electromagnetic Fields "Széchenyi István” University Gyor, Hungary, 2009.

[25] Riccardo Hertel and Attila Kákay. "Hybrid finite-element/boundary-element method to calculate Oersted fields". In: *Journal of Magnetism and Magnetic Materials* 369 (Nov. 2014), pp. 189–196. DOI: 10.1016/j.jmmm.2014.06.047.

[26] Florian Bruckner et al. "3D FEM–BEM-coupling method to solve magnetostatic Maxwell equations". In: *Journal of Magnetism and Magnetic Materials* 324.10 (May 2012), pp. 1862–1866. DOI: 10.1016/j.jmmm.2012.01.016.

[27] Markus Rech. "Effiziente Nahfeldkubatur in der Galerkin-Randelementmethode". Diploma Thesis. Bonn: Rheinischen Friedrich-Wilhelms-Universität Bonn, Mar. 2002.

[28] D.R. Fredkin and T.R. Koehler. "Hybrid method for computing demagnetizing fields". In: *IEEE Transactions on Magnetics* 26.2 (Mar. 1990), pp. 415–417. DOI: 10.1109/20.106342.

[29] Claas Abert et al. "A fast finite-difference algorithm for topology optimization of permanent magnets". In: *Journal of Applied Physics* 122.11 (Sept. 21, 2017), p. 113904. DOI: 10.1063/1.4998532.

[30] Gregor Wautischer et al. "Topology optimization of a heat-assisted magnetic recording write head to reduce transition curvature using a binary optimization algorithm utilizing the adjoint method". In: *Scientific Reports* 12.1 (Aug. 2022), p. 13986. DOI: 10.1038/s41598-022-18112-z.

[31] F. Campelo, J. A. Rmiírez, and H. Igarashi. *A survey of topology optimization in electromagnetics: considerations and current trends*. 2010.

[32] Jeonghoon Yoo and Noboru Kikuchi. "Topology optimization in magnetic fields using the homogenization design method". In: *International Journal for Numerical Methods in Engineering* 48.10 (Aug. 10, 2000), pp. 1463–1479. DOI: 10.1002/1097-0207(20000810)48:10<1463::AID-NME952>3.0.CO;2-5.

[33] J. Kang and S. Wang. "Shape optimization of BLDC motor using 3-D finite element method". In: *IEEE Transactions on Magnetics* 36.4 (July 2000), pp. 1119–1123. DOI: 10.1109/20.877637.

[34] Y. Okamoto, K. Akiyama, and N. Takahashi. "3-D topology optimization of single-pole-type head by using design sensitivity analysis". In: *IEEE Transactions on Magnetics* 42.4 (Apr. 2006), pp. 1087–1090. DOI: 10.1109/TMAG.2006.871422.

[35] Semyung Wang et al. "Topology optimization of electromagnetic systems considering magnetization direction". In: *IEEE Transactions on Magnetics* 41.5 (May 2005), pp. 1808–1811. DOI: 10.1109/TMAG.2005.846480.

[36] S. Wang and J. Kang. "Topology optimization of nonlinear magnetostatics". In: *IEEE Transactions on Magnetics* 38.2 (Mar. 2002), pp. 1029–1032. DOI: 10.1109/20.996264.

[37] P. Seebacher et al. "Optimization of an Electromagnetic Actuator using Topology-Optimization". In: *2019 22nd International Conference on the Computation of Electromagnetic Fields (COM-*

PUMAG). 2019 22nd International Conference on the Computation of Electromagnetic Fields (COMPUMAG). Paris, France: IEEE, July 2019, pp. 1–4. ISBN: 978-1-72815-592-0. DOI: 10.1109/COMPUMAG45669.2019.9032821.

[38] Martin P. Bendsøe and Ole Sigmund. *Topology Optimization*. Berlin, Heidelberg: Springer Berlin Heidelberg, 2004. ISBN: 978-3-642-07698-5 978-3-662-05086-6. DOI: 10.1007/978-3-662-05086-6.

[39] Alain Bossavit. *Computational electromagnetism: variational formulations, complementarity, edge elements*. OCLC: 162128760. San Diego: Academic Press, 1998. ISBN: 978-0-08-052966-0.

[40] C. Huber et al. "Topology optimized and 3D printed polymer-bonded permanent magnets for a predefined external field". In: *Journal of Applied Physics* 122.5 (Aug. 7, 2017), p. 053904. DOI: 10.1063/1.4997441.

[41] Ciyou Zhu et al. "Algorithm 778: L-BFGS-B: Fortran subroutines for large-scale bound-constrained optimization". In: *ACM Transactions on Mathematical Software* 23.4 (Dec. 1, 1997), pp. 550–560. DOI: 10.1145/279232.279236.

[42] M Nordaas and Simon W. Funke. *The Moola optimisation package*. 2016. URL: https://github.com/funsim/moola (visited on 2016).

[43] Chang-Hwan Im, Hyun-Kyo Jung, and Yong-Joo Kim. "Hybrid genetic algorithm for electromagnetic topology optimization". In: *IEEE Transactions on Magnetics* 39.5 (Sept. 2003), pp. 2163–2169. DOI: 10.1109/TMAG.2003.817094.

[44] Yoshifumi Okamoto and Norio Takahashi. "A Novel Topology Optimization of Nonlinear Magnetic Circuit Using ON/OFF Method". In: *IEEJ Transactions on Fundamentals and Materials* 125.6 (2005), pp. 549–553. DOI: 10.1541/ieejfms.125.549.

[45] Florian Slanovc et al. "Global Magnetic Topology Optimization". In: *SSRN Electronic Journal* (2022). DOI: 10.2139/ssrn.4189409.

[46] A. Guedes et al. "Improving Magnetic Field Detection Limits of Spin Valve Sensors Using Magnetic Flux Guide Concentrators". In: *IEEE Transactions on Magnetics* 43.6 (June 2007), pp. 2376–2378. DOI: 10.1109/TMAG.2007.893119.

[47] R.E. Rottmayer et al. "Heat-Assisted Magnetic Recording". In: *IEEE Transactions on Magnetics* 42.10 (Oct. 2006), pp. 2417–2421. DOI: 10.1109/TMAG.2006.879572.

[48] M.H. Kryder et al. "Heat Assisted Magnetic Recording". In: *Proceedings of the IEEE* 96.11 (Nov. 2008), pp. 1810–1835. DOI: 10.1109/JPROC.2008.2004315.

[49] R. F. L. Evans et al. "Thermally induced error: Density limit for magnetic data storage". In: *Applied Physics Letters* 100.10 (Mar. 5, 2012), p. 102402. DOI: 10.1063/1.3691196.

[50] Jian-Gang Jimmy Zhu and Hai Li. "Correcting Transition Curvature in Heat-Assisted Magnetic Recording". In: *IEEE Transactions on Magnetics* 53.2 (Feb. 2017), pp. 1–7. DOI: 10.1109/TMAG.2016.2614836.

[51] Zengyuan Liu et al. "Curvature and Skew in Heat-Assisted Magnetic Recording". In: *IEEE Transactions on Magnetics* 55.3 (Mar. 2019), pp. 1–8. DOI: 10.1109/TMAG.2018.2868128.

[52] Jian-Gang (Jimmy) Zhu and Hai Li. "Write head field design for correcting transition curvature in heat assisted magnetic recording". In: *AIP Advances* 7.5 (May 2017), p. 056505. DOI: 10.1063/1.4976733.

[53] Simon Greaves et al. "Split-Pole Write Head for Thermally Assisted Magnetic Recording". In: *IEEE Transactions on Magnetics* 47.10 (Oct. 2011), pp. 2375–2378. DOI: 10.1109/TMAG.2011.2146234.

[54] Simon John Greaves, R. Itagaki, and Yasushi Kanai. "A Model for Predicting Transition Curvature in Heat-Assisted Magnetic Recording". In: *IEEE Transactions on Magnetics* (2019), pp. 1–6. DOI: 10.1109/TMAG.2018.2885990.

[55] Cheng-Ming Chow and James A. Bain. "A Split-Pole-Gapped NFT Write Head Design for Transition Curvature Reduction in Heat-Assisted Magnetic Recording". In: *IEEE Transactions on Magnetics* 54.11 (Nov. 2018), pp. 1–4. DOI: 10.1109/TMAG.2018.2835311.

[56] N. X. Sun, A. M. Crawford, and S. X. Wang. "Advanced Soft Magnetic Materials for Magnetic Recording Heads and Integrated Inductors". In: *MRS Proceedings* 721 (2002), E6.3. DOI: 10.1557/PROC-721-E6.3.

[57] Florian Bruckner et al. "Solving Large-Scale Inverse Magnetostatic Problems using the Adjoint Method". In: *Scientific Reports* 7 (Jan. 18, 2017), p. 40816.

[58] Gregor Wautischer et al. "Solving the inverse magnetostatic problem using fictitious magnetic charges". In: *AIP Advances* 8.5 (May 2018), p. 056005. DOI: 10.1063/1.5007348.

[59] A. Kost, T. Honma, and H. Igarashi. "Inverse inference of magnetization distribution in cylindrical permanent magnets". In: *IEEE Transactions on Magnetics* 36.4 (July 2000), pp. 1168–1171. DOI: 10.1109/20.877648.

[60] O. Chadebec et al. "Recent improvements for solving inverse magnetostatic problem applied to thin shells". In: *IEEE Transactions on Magnetics* 38.2 (Mar. 2002), pp. 1005–1008. DOI: 10.1109/20.996258.

[61] Laure Arbenz et al. "Characterization of Permanent Magnet Magnetization". In: *IEEE Transactions on Magnetics* 53.11 (Nov. 2017), pp. 1–4. DOI: 10.1109/TMAG.2017.2692391.

[62] Armand Wirgin. "The inverse crime". In: (2004). Publisher: arXiv Version Number: 1. DOI: 10.48550/ARXIV.MATH-PH/0401050.

[63] Per Christian Hansen and Dianne Prost O'Leary. "The Use of the L-Curve in the Regularization of Discrete Ill-Posed Problems". In: *SIAM Journal on Scientific Computing* 14.6 (Nov. 1993), pp. 1487–1503. DOI: 10.1137/0914086.

[64] Julieta Bollati, Claudia M. Gariboldi, and Domingo A. Tarzia. "Explicit solutions for distributed, boundary and distributed-boundary elliptic optimal control problems". In: *Journal of Applied Mathematics and Computing* 64.1 (Oct. 2020), pp. 283–311. DOI: 10.1007/s12190-020-01355-2.

[65] Taehoon Jung, Jaejoon Lee, and Jaewook Lee. "Design and Fabrication of Magnetic System Using Multi-Material Topology Optimization". In: *IEEE Access* 9 (2021), pp. 8649–8658. DOI: 10.1109/ACCESS.2021.3049271.

[66] M. Suppan et al. "In-situ alignment of 3D printed anisotropic hard magnets". In: *Scientific Reports* 12.1 (Oct. 20, 2022), p. 17590. DOI: 10.1038/s41598-022-20669-8.

[67] Stefan Pollok, Rasmus Bjork, and Peter Stanley Jorgensen. "Inverse Design of Magnetic Fields Using Deep Learning". In: *IEEE Transactions on Magnetics* 57.7 (July 2021), pp. 1–4. DOI: 10.1109/TMAG.2021.3082431.

[68] Hayaho Sato and Hajime Igarashi. "Deep learning-based surrogate model for fast multi-material topology optimization of IPM motor". In: *COMPEL - The international journal for computation and mathematics in electrical and electronic engineering* 41.3 (May 10, 2022), pp. 900–914. DOI: 10.1108/COMPEL-03-2021-0086.

A. Appendix

A.1. Dual Space

As also explained in [21] in more detail, every Hilbert space H possesses an orthonormal basis ψ and an element $u \in H$ is represented as

$$u(\boldsymbol{r}) = \sum_i u_i(\boldsymbol{r})\,\psi_i(\boldsymbol{r}), \tag{A.1}$$

where ψ_i are the single basis functions and u_i are the coefficients of the coefficient vector $\boldsymbol{u}$.

The dual basis ψ^* of the dual space H^* is defined by

$$\psi_i^*(\psi_j) = \delta_{ij} \quad \forall i, j, \tag{A.2}$$

where the single ψ_i^* are functionals since they are elements of H^*. We can therefore, depict an arbitrary element $I \in H^*$ as

$$I = \sum_i I_i \psi_i^*, \tag{A.3}$$

where the I_i are the coefficients of the coefficient vector $\boldsymbol{I}$. Applying I onto a vector $u \in H$ then means

$$\begin{gathered} U(u) = \sum_i I_i \psi_i^* \left(\sum_j u_j \psi_j \right) = \sum_{i,j} I_i u_j \psi_i^*(\psi_j) = \sum_{i,j} I_i u_j \delta_{ij} = \sum_i I_i u_i = \\ \boldsymbol{I} \cdot \boldsymbol{u} = \boldsymbol{I}^T \boldsymbol{u} = (\boldsymbol{I}, \boldsymbol{u})_{\ell^2}, \end{gathered} \tag{A.4}$$

where we have introduced the ℓ^2 or euclidean inner product of two column vectors $\boldsymbol{a}$ and $\boldsymbol{b}$ as $(\boldsymbol{a}, \boldsymbol{b})_{\ell^2} = \boldsymbol{a}^T \boldsymbol{b}$.

A.2. Obtaining the Riesz representers

The Riesz map is inner product dependent. In the case of the L^2 inner product, that is defined as

$$(u, v)_{L^2} = \int_\Omega u(\boldsymbol{r})\, v(\boldsymbol{r})\, \mathrm{d}\boldsymbol{r}, \tag{A.5}$$

since $u = \sum_i u_i \psi_i$, $v = \sum_i v_i \psi_i$, this can be transformed into a matrix representation

$$\begin{gathered} (u, v)_{L^2} = \int_\Omega \sum_i u_i \psi_i \sum_j v_j \psi_j \, \mathrm{d}\boldsymbol{r} = \\ \sum_i u_i \sum_j v_j \int_\Omega \psi_i \psi_j \, \mathrm{d}\boldsymbol{r} = \boldsymbol{v}^T M \boldsymbol{u} \end{gathered} \tag{A.6}$$

with M being the so called mass matrix

$$M_{ij} = \int_{\Omega} \psi_i \psi_j \, \mathrm{d}\boldsymbol{r}. \tag{A.7}$$

Now, according to the Riesz representation theorem a functional I can be uniquely represented by its Riesz representer $\mathcal{R}_{L^2}(I)$. If we identify v with $\mathcal{R}_{L^2}(I)$ we get

$$I(u) = (\mathcal{R}_{L^2}(I), u)_{L^2} = (v, u)_{L^2}. \tag{A.8}$$

Furthermore, as shown above (section A.1) a functional I can be represented in the dual basis ϕ^* and the application of I onto u that is $I(u)$ can be written as

$$I(u) = \boldsymbol{I}^T \boldsymbol{u} = (\boldsymbol{I}, \boldsymbol{u})_{\ell^2}. \tag{A.9}$$

The two different representations must of course give the same result

$$(v, u)_{L^2} = \boldsymbol{v}^T M \boldsymbol{u} = \boldsymbol{I}^T \boldsymbol{u} = (\boldsymbol{I}, \boldsymbol{u})_{\ell^2} \tag{A.10}$$

and it can therefore be seen that the mass matrix can be used to perform transformations between the two representations

$$\boldsymbol{I} = M\boldsymbol{v}. \tag{A.11}$$

Consider now the Riesz representer of I with respect to the ℓ^2 inner product

$$I(u) = (\mathcal{R}_{\ell^2}(I), u)_{\ell^2} = \boldsymbol{w}^T \boldsymbol{u}. \tag{A.12}$$

If the representation of the dual basis ψ^*

$$\boldsymbol{I}^T \boldsymbol{u} = \boldsymbol{w}^T \boldsymbol{u} \tag{A.13}$$

that with respect to the ℓ^2 inner product the coefficient vectors of the dual and the primal representation of I are identical.